Design of a Linear Cavity and a Characterization Setup for Multi-pass Transmission Electron Microscopy

by

Marco Turchetti

Submitted to the Department of Electrical Engineering and Computer Science
in partial fulfillment of the requirements for the degree of

Master of Science in Electrical Engineering and Computer Science

at the

MASSACHUSETTS INSTITUTE OF TECHNOLOGY

February 2019

Author ... Signature redacted ....
Department of Electrical Engineering and Computer Science
January 31, 2019

Certified by. Signature redacted..................
Karl K. Berggren
Professor of Electrical Engineering and Computer Science
Thesis Supervisor

Accepted by..... Signature redacted ....
Leslie A. Kolodziejski
Professor of Electrical Engineering and Computer Science
Chair, Department Committee on Graduate Students

Design of a Linear Cavity and a Characterization Setup for Multi-pass Transmission Electron Microscopy

by

Marco Turchetti

Submitted to the Department of Electrical Engineering and Computer Science
on January 31, 2019, in partial fulfillment of the
requirements for the degree of
Master of Science in Electrical Engineering and Computer Science

Abstract

In this thesis, the different electron optical components necessary to build a linear cavity for multi-pass transmission electron microscopy are analyzed and simulated. Moreover, a prototype of the core component, the gated mirror, was designed and some preliminary experimental testings were carried out to asses its optical properties. Then, an architecture of the complete linear cavity, including the correction of spherical aberration and image rotation was designed, optimized and validated through simulation. Finally, an experimental setup for the characterization of electron optical elements was also designed, implemented and experimentally tested. Such a diagnostics setup is going to be adopted for the verification of the multi-pass components optical properties, performance, and their agreement to the design specifications.

Thesis Supervisor: Karl K. Berggren
Title: Professor of Electrical Engineering and Computer Science

Acknowledgments

The work presented in this thesis would not have been possible without constant support and advice from my colleague, friends and family. In particular, I would like to thank:

My advisor Prof. Karl K. Berggren for his guidance and for creating a friendly and stimulating research environment in which I find myself able to develop my scientific skills and creativity.

Dr. Chung-Soo Kim for believing in my abilities and for guiding and mentoring me throughout the whole project. I couldn't have done it without him and his expertise.

My office mate Navid Abedzadeh for thoughtful discussions, experimental assistance, and, last but not least, for his friendship.

Akshay Agarwal and Brenden Butters for their valuable advice and many helpful discussions.

Prof. Richard G. Hobbs for his precious insight and for passing down to me his excitement about the project.

Our collaborators at TU Delft, Erlangen and Stanford for helpful conversations during our project meetings, in particular Prof. Pieter Kruit for his immense knowledge in electron optics.

All my friends and my coworkers, in particular Murat Onen for his constant moral support and for being my graduate school wingman.

The Gordon and Betty Moore Foundation for supporting financially this work.

My parents and sisters for always believing in me and supporting me in all my choices. They are the people I will always be able to count on.

Contents

List of Figures

List of Tables

Chapter 1

Introduction

The introduction of electron microscopy as an alternative to light microscopy opened the door for the exploration of the atomic world. This new world was previously inaccessible because the wave nature of light ties the smallest detail that we can resolve to its wavelength. The Abbe's criterion, or diffraction limit, states that it is impossible to resolve two elements of a structure that are closer than half the probe wavelength. However, while typical lattice constants are in the order of fractions of nanometers, visible light has a wavelength between 400 nm and 700 nm. Hence, we cannot hope to explore the atomic structure of a sample using light. On the other hand, an electron, if properly accelerated, can easily reach a sub-nm wavelength ($\lambda = h/\sqrt{2mE}$). Therefore, using electrons instead of photons as probe particles, the resolution is no more limited by the diffraction, and atomic scale imaging can be achieved. The PICO TEM at the Forschungszentrum Julich in Germany, which is one of the few instruments in the world equipped with both spherical and chromatic aberration correction, achieved 50 pm resolution.[1]

However, other phenomena become important to constrain the smallest detail that we can resolve. These pertain to the quality of the source and the electron optical setup, like aberrations, or to the sample itself, such as the volume of interaction and the damage induced to the sample by the probe. The latter represents the main resolution limit when imaging radiation sensitive samples such as biological specimens, preventing to resolve their atomic constituents.[2, 3, 4] The effort toward the solution of the radiation damage problem is the very motive of this work.

Resolving the atomic structure of macromolecules is a fundamental component for our understanding of their nature and behavior and it would be a great instrument in the hands of biologists and doctors. However, the dose of electrons necessary to overcome the shot noise and resolve such fine details, while it is not a problem for more robust samples like solid state devices, in these sensitive samples causes different side effects[5]:

1. damage to polymers and tissue due to excitation of phonons that heat the specimen;
2. atom dislocation resulting in point defects;
3. breaking of chemical bonds due to inelastic scattering (radiolysis).

Williams and Carter refer to it as the "microscopists' analog of the Heisenberg uncertainty principle in that the very act of observing your specimen can change it".[5] Fig. 1-1 illustrates an example of the evolution of such radiolysis damage on a protein-based sample while the dose progressively increases.[6]

In the last decades, to address this problem cryo-electron microscopy was developed. This powerful technique, that was awarded the Chemistry Nobel prize in 2017, allows the mapping of a macromolecule with a resolution of few angstroms thanks to advanced image processing techniques that reconstruct the topography of one macromolecule starting from thousands of lower resolution images of identical macromolecules. [7, 8, 9, 10, 11] Therefore, this technique is able to get around the problem of radiation damage without really solving it, because it does not allow direct imaging of a single molecule at atomic resolution that would be the ideal solution. It shows astonishing results but exhibits some critical issues in terms of effort in preparing several identical samples and complexity of data treatment. Also, imaging a live biological process in cryo-EM is out of the question. The sample must be in a crystallized state.

Alternative techniques are under investigation, such as electron wavefront engineering to verify structural hypotheses [12], entanglement-assisted electron mi-

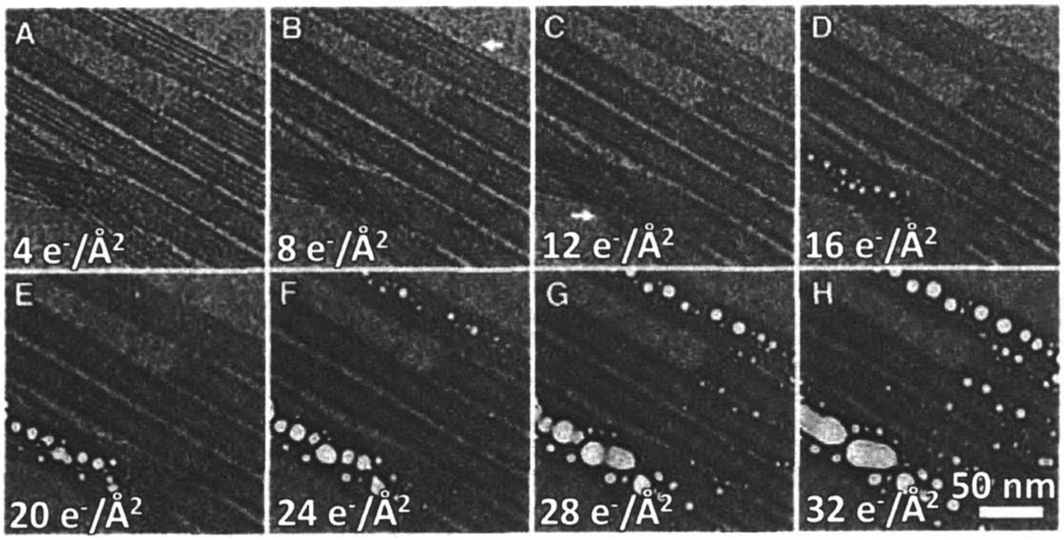

Figure 1-1: Radiation damage - Evolution of the radiolysis damage while progressively increasing the cumulative dose received by a sample comprised of microtubules, which are a protein-based specimens. Each frame corresponds to an additional cumulative dose of $4\,\mathrm{e}^-/\mathrm{\AA}^2$. From frame B the sample start to exhibit the damage due to radiolysis, which is visible in term of blurring of the microtubules edges. From image C it is also possible to see the development of hydrogen gas bubbles due to the breaking of hydrogen bondings. This Figure was taken from Ref. [6].

croscopy based on a flux qubit [13], electron holography/ptychography [14, 15],quantum electron microscopy (QEM) [16] and multi-pass transmission electron microscopy [17, 18]. In this thesis, we are going to concentrate on the multi-pass approach.

1.1 Motivation for Multi-pass

In order to solve the issue of damage to the sample, we need to change our measurement scheme. Giovannetti et al. in [19, 20] address this issue analyzing the recent developments in quantum metrology and characterizing different measurement strategies in term of the improvement in the signal to noise ratio that they guarantee respect to classical approaches.

We can consider the interaction of a probe p_0 with our sample as a unitary operation $\Phi_x = e^{-iHx}$ where H is a Hermitian operator with eigenvalues λ_i and x is the quantity that we are going to measure, which in our case is going to be the phase. Once we define this framework Giovannetti et al. analyze two different approaches, one where N probes are employed in parallel, which is depicted in Fig. 1-2, and one where a single probe is sequentially employed N times, which is shown in Fig. 1-3. In the parallel case, we can also decide to entangle the N probes, entangling the outputs or both. It is possible to show that the minimum error δx, hence the resolution, that we can obtain using these measurement schemes is:

1. Parallel measurement fully classical (CC) and parallel measurement entangling the output (CQ): $\delta x \geq \frac{1}{\sqrt{N\nu}(\lambda_M - \lambda_m)}$, where ν is the number of times the estimation is repeated and λ_M and λ_m are the maximum and minimum eigenvalues of H, respectively.

2. Parallel measurement with probe entanglement (QC), parallel measurement with both probe and output entanglement (QQ) and sequential measurement: $\delta x \geq \frac{1}{N\sqrt{\nu}(\lambda_M - \lambda_m)}$

Therefore, as the damage is going to be proportional to the dose that we use on the sample, hence proportional to $N\nu$, we can conclude that at a constant damage

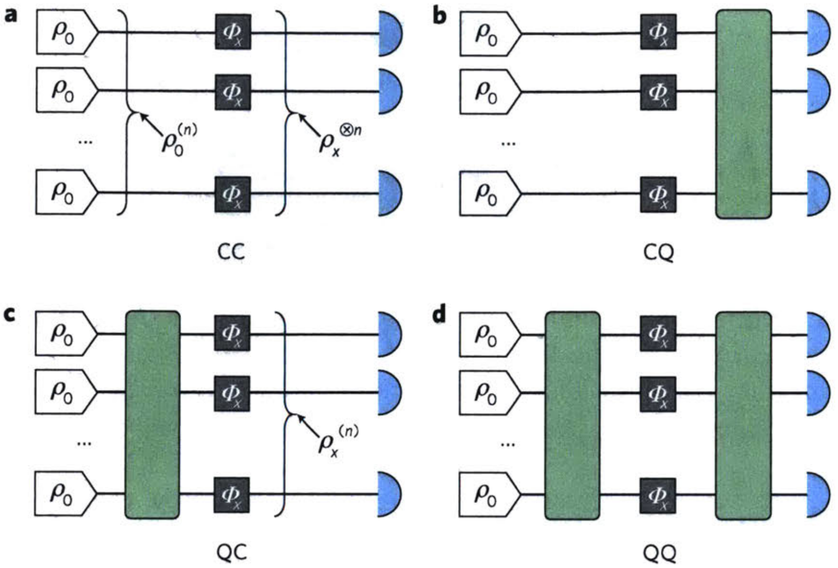

Figure 1-2: Parallel estimation strategies - Schematic of the possible strategies with N parallel estimations. In particular (a) the condition of classical imaging CC; (b) the condition with entangled outputs after the interaction of the probe with the sample CQ; (c) the condition with entangled probes QC; (d) the condition of both entangled probes and outputs QQ. CC and CQ entails a $\delta x \propto \frac{1}{\sqrt{N\nu}}$. Instead, QC and QQ entails a $\delta x \propto \frac{1}{N\sqrt{\nu}}$. This Figure was taken from Ref. [20]

we can achieve an improvement in resolution of a factor of $\sqrt{N}$ if we either do a parallel measurement with entangled probe or a sequential measurement. As we are interested in electron microscopy and the entanglement of electrons is something that is not going to be possible in the foreseeable future, the only concrete option to use this result is to employ a sequential measurement scheme, or multi-pass.

In this measurement strategy, the phase information of the sample can be sequentially accumulated by re-imaging the sample on itself inside an electron resonant cavity N times, which leads to a decrease in damage proportional to $\sqrt{N}$ compared to traditional phase contrast imaging while keeping the signal to noise constant. As biological samples imaged at high electron energy are typically weak phase objects, this method can be successfully implemented for bio-imaging.

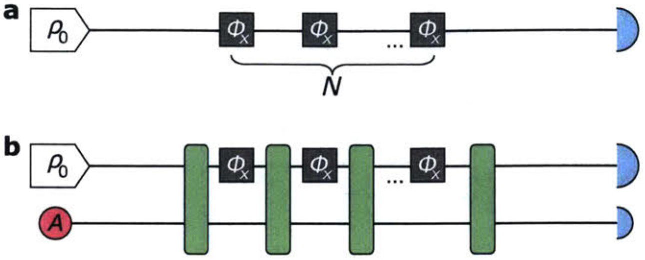

Figure 1-3: Sequential estimation strategies - Schematic of the strategy with N sequential estimations: (a) the basic scheme; (b) the same scheme with an entangled external ancillary system. This scheme entails a $\delta x \propto \frac{1}{N\sqrt{\nu}}$. The ancillary system does not have any effect on the resolution δx. This Figure was taken from Ref. [20]

1.2 Resonant Cavity for Electrons

The concept of a resonant cavity for electron has been proposed before in the context of quantum electron microscopy,[16, 21] but has never been experimentally realized yet. As with most electron microscopy concepts, this idea is borrowed from optics where cavities are well established. In optics, to build a cavity you can simply use two semitransparent mirrors.[17] In electron optics, this component does not exist. Kruit et al. proposed to use gated mirrors, which has not been experimentally demonstrated yet. A gated mirror is an electron optical component usually kept to a negative potential high enough as to act as a two-sided mirror for the incoming electrons. When a sufficiently large positive pulse is applied to the gated mirror, the potential barrier is lowered and the electrons can pass through.

Fig. 1-4 portrays the optical diagram of a possible implementation of a multi-pass microscope, built using two gated mirrors as core components to define the boundaries of the cavity. In this schematic, the electron illumination beam (red in the figure) is emitted by the electron gun. The beam has to be generated by a pulsed source such as a laser triggered source, because in this way it can be in-coupled and out-coupled into and from the cavity without being disturbed by the varying potential distribution in the gated mirrors. After being generated by the source the beam passes through the illumination optics that focus it onto the first gated mirror (highlighted in yellow). The gated mirror is drawn here as a wedge because, as will be discussed in the following chapters, for the system to be stable this component needs to correct spherical aberrations, hence it needs to create a hyperbolic mirror surface that can be achieved when its core electrode has a wedge shape. The gated mirror is closed until a pulse is applied which let the electron access the cavity. Once inside the electron path is guided by two lenses which collimate the beam onto the sample. Part of the beam will pass through the sample (red) and part will be scattered (blue). A system of lenses and a second gated mirror placed symmetrically respect to the sample will reflect back the electrons and re-image the sample on itself. Then, we let the system resonate in the cavity and the phase information is gradually accumulated. Of course, the resonant cavity has to be designed so that the resonance of both the illumination and scattered beam are sustained. After a sufficient number of round-trips, when the necessary phase information has been accumulated, an appropriately timed voltage pulse on the second gated mirror is used to out-couple the electrons towards the projection optics outside the cavity. The projection optics magnify the image and, ultimately, a phosphorus screen or a CCD sensitive to electrons is placed on the image plane and the resulting image is recorded.

1.3 Thesis Goal and Outline

The goal of my Master's Thesis is to design and demonstrate through simulation a linear resonant cavity for multi-pass TEM, and to develop a reliable experimental procedure for the characterization of the electron optical components necessary to build such a cavity. The design has to include the validation of the cavity optical properties through ray-tracing simulation that can be done using electron optical software such as Lorentz. Also, as the system requires novel high-speed electron optical components, RF simulations of such elements are also necessary. These can be carried out using COMSOL and MATLAB. Moreover, the design has to consider the effect of intrinsic aberrations of the column as well as machining defects and misalignments. On the other hand, the experimental procedure for the characterization of the electron optical components can be done modifying an SEM column so to allow the

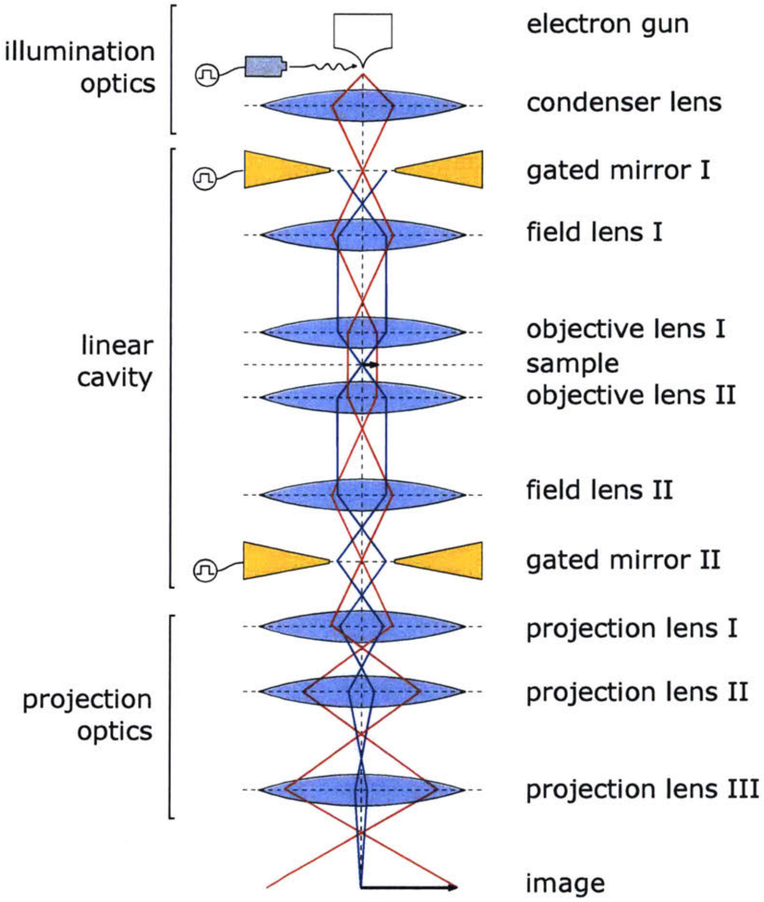

Figure 1-4: Multi-pass schematics - Optical diagram of the multi-pass microscope, showing the illumination beam in red and the scattered beam in blue. The hyperbolic gated mirrors, which bound the cavity, are highlighted in yellow. The beam is generated by a pulsed source, then it is in-coupled into the cavity where it resonate accumulating the sample phase information. After a sufficient number of roundtrips is then out-coupled, magnified by the projection optics and imaged.

analysis of the beam in transmission implementing energy spectroscopy and shadow imaging measurement schemes and applying the Ronchingrams theory and possibly ptychography for aberration characterization.[22, 23, 24] Such an effort would be a significant step towards the realization of a multi-pass system.

Chapter 2

Components for Multi-pass

In order to build a multi-pass microscope we need to study, design and develop electron optical components to guide, focus and control in time the electron beam path. These components include electrostatic and magnetic lenses, gated mirrors and a pulsed source. In particular, we are interested in their optical characteristics, design parameters, and aberration.

In this chapter I am going to do a review of aberration theory and report on the design of electron lenses,[21] gated mirrors and their use to correct aberrations. Finally, I am going to discuss two different ways we can generate a pulsed electron beam.

2.1 Aberration Theory

An ideal electron lens is an object that when placed in the path of an electron it exerts an angular deflection to the electron trajectory proportional to the distance r from the lens optical axis. This proportionate deflection means that parallel rays are going to be focused at the same spot. In other words, an incoming plane wave is converted to a spherical wave. If we consider the rays coming from an object, this property results into the creation of an image of the object at a position that can be calculated using the lens equation:

$$\frac{1}{f} = \frac{1}{o} + \frac{1}{i} \tag{2.1}$$

where f is the focal distance, o is the object position and i is the image position.

However, a real lens exhibits parasitic effects. Some of these effects are intrinsic and are simply due to the fact that the r deflection is just an approximation (paraxial approximation), but higher orders of deflection do exist. Other parasitic effects are due to imperfections, misalignment and machining defects. These are the so-called geometrical aberrations. Moreover, the deflection strength for real lenses is dependent on the electron energy. This characteristic generates the so-called chromatic aberrations.[25]

2.1.1 Geometrical Aberrations

A geometrical aberration is usually classified using two numbers, its radial order N and its azimuthal symmetry S. The aberration strength is given by a coefficient C_{NS}, which is dimensionless. These three parameters unequivocally define the phase difference between the spherical wave produced by an ideal lens and the actual wavefront due to the real lens. In the paraxial approximation this wave aberration function can be expressed as: [26]

$$\chi(\theta, \phi) = K + \sum_{N=0}^{\infty} \sum_{S} \frac{\theta^{N+1}}{N+1} \left[C_{NSa} cos(S\phi) + C_{NSb} cos(S\phi) \right], \tag{2.2}$$

where K is a constant, $S \in [0, N+1]$ and takes only the values of opposite parity with respect to N, that is to say that if N is even/odd S takes all the odd/even values from 0 to N+1, θ is the angle with respect to the optical axis and ϕ is the angle on the azimuthal plane.

Following this definition for the aberration function χ, the aberration coefficient can be written as:

$$C_{NS} = \sqrt{C_{NSa}^2 + C_{NSb}^2}. \tag{2.3}$$

Table 2.1: Aberration coefficients up to the fifth radial order [26, 21]

Radial order N	Azimuthal symmetry S	Aberration Coefficient	Name
0	1	C_{01}	Image Shift
1	0	C_{10}	Defocus
1	2	C_{12}	Twofold Astigmatism
2	1	C_{21}	Coma
2	3	C_{23}	Threefold Astigmatism
3	0	C_{30}	Spherical aberration
3	2	C_{32}	Twofold Astigmatism of C_3
3	4	C_{34}	Fourfold Astigmatism of C_3
4	1	C_{41}	Four order Coma
4	3	C_{43}	Fourth order threefold astigmatism
4	5	C_{45}	Fivefold astigmatism
5	0	C_{50}	Fifth order spherical aberration
5	2	C_{52}	Twofold astigmatism of C_5
5	4	C_{54}	Fourfold astigmatism of C_5
5	6	C_{56}	Sixfold astigmatism of C_5

Table 2.1 summarizes the aberrations up to the fifth order.

The shapes of the correspondent aberrations are portrayed in Fig. 2-1 from [26].

The most important of the geometrical aberrations is the third-order spherical aberration. The reason for it, is that spherical aberration is usually the dominant one and also because it is intrinsic to the lens, it is not due to machining or alignment errors, as demonstrated by the Scherzer's theorem.[27] Spherical aberration is caused by the fact that the angular deflection is not exactly linear with r but higher orders of deflection are present. The result is that rays which are closer to the optical axis are going to be focused farther away. This effect generates a non-zero classical spot size. The spot size can be calculated as:

$$d_S = \frac{C_S \alpha^3}{2}, \tag{2.4}$$

where α is the semiangle and $C_S = \frac{\lambda}{2\pi} C_{30}$ is typically the number referred as the spherical aberration coefficient, which is expressed in m.

It is worth noting that the spot size would not be zero even with null aberration, since it would be diffraction-limited. The diffraction-limited spot can be calculated

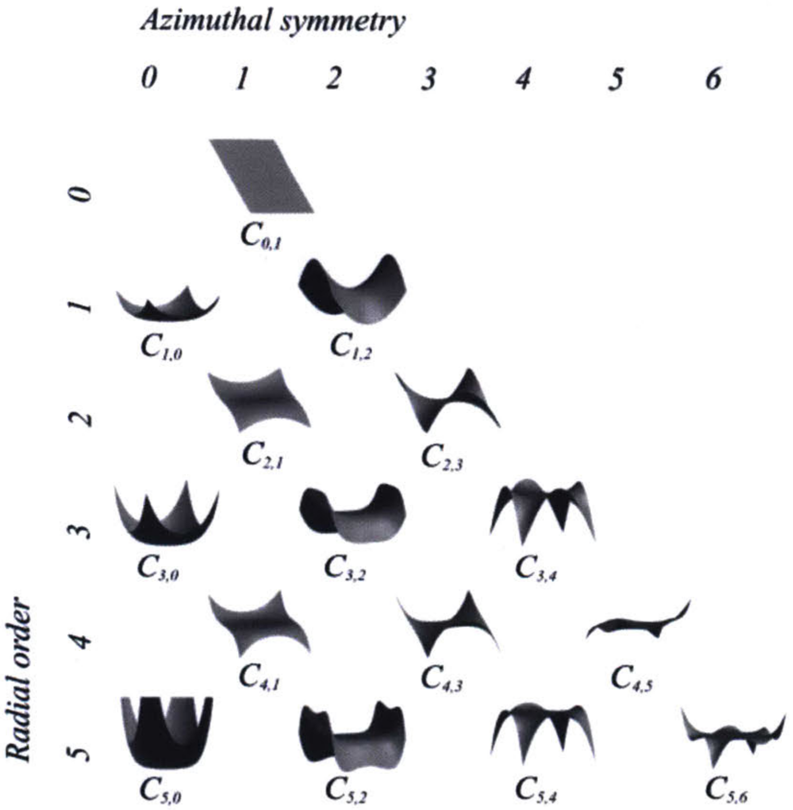

Figure 2-1: Three-dimensional representation of the first fifth orders aberration wavefronts - The wavefront representation are classified accordingly to their radial order N and azimuthal symmetry S. This Figure was taken from [26]

as:

$$d_D = \frac{\lambda}{2\text{sin}\alpha}, \tag{2.5}$$

where $\lambda = \frac{h}{\sqrt{2mE}}$ is the electron De Broglie wavelengths, which for the energies used in microscopy is usually of the order of picometers.

In order to better visualize and understand the effect of aberrations on the electron beam spot and, consequently, on the image generated by the lens, it is useful to define the beam point spread function $PSF(\mathbf{r})$. This quantity is the impulse response of the imaging system. In an SEM, where we image the source onto a sample, if we consider the electron source as a point source, the $PSF(\mathbf{r})$ corresponds to the beam spatial distribution at the object, where it is focused. Therefore, it determines the surface where the electrons interact with the sample. Of course, the image in this case will not only be determined by the $PSF(\mathbf{r})$ but also by the volume of interaction that generates the detected signal (e.g. the number of secondary electrons generated). Instead, in a TEM, which is more similar to a standard optical system the $PSF(\mathbf{r})$ is going to correspond to the response of the system at the image plane for each point of the object. Therefore the image can be determine convolving the object with the $PSF(\mathbf{r})$: $I(\mathbf{r}) = O(\mathbf{r}) \circledast PSF(\mathbf{r})$. To evaluate the $PSF(\mathbf{r})$ due to a certain geometric aberration it is convenient to define its Fourier transform, the contrast transfer function $T(\mathbf{q}) = \mathscr{F}(PSF(\mathbf{r}))$. Then the $T(\mathbf{q})$ due to aberrations can be simply defined as: [28, 29]

$$T(\mathbf{q}) = A(\mathbf{q})e^{iW(\mathbf{q})}, \tag{2.6}$$

where $A(\mathbf{q})$ is a function which in general corresponds to the shape of the objective aperture but it can incorporate also other non-idealities of the source etc., and $W(\mathbf{q})$ is the phase factor which contains the aberrations. An easy way to build this phase factor is to use the Zernike polynomials: $Z_n^m(\mathbf{q})$. Then the phase factor can be easily written as:

$$W(\mathbf{q}) = \sum_{n,m} C_n^m Z_n^m(\mathbf{q}). \tag{2.7}$$

For instance, the polynomial $Z_4^0(\mathbf{q})$ introduces spherical aberration in the wavefront. Fig. 2-2 shows the $W(\mathbf{q})$ function and the correspondent $PSF(\mathbf{r})$ evaluated using MATLAB for $C_4^0 = 2$.

2.1.2 Chromatic Aberrations

As previously anticipated the second category of aberration is chromatic aberrations. They are due to the fact that is impossible to generate a monochromatic beam. A beam generated by an electron gun is going to have a Gaussian energy distribution with energy spread ΔE. Electron lenses are going to exert the same force to each

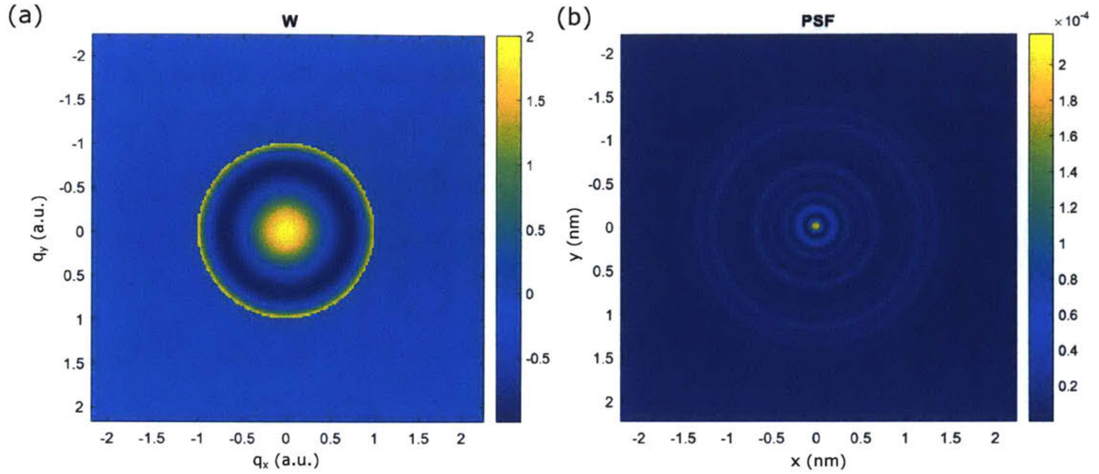

Figure 2-2: Calculation of the phase factor and point spread function of a spherically aberrated beam - The evaluation of the phase factor $W(\mathbf{q})$ (a) and point spread function $PSF(\mathbf{r})$ (b) for a beam affected by spherical aberration was performed using MATLAB. $W(\mathbf{q})$ was calculated imposing $C_4^0 = 2$, coefficient of the Zernike polynomial with $n = 4$ and $m = 0$. This is the polynomial responsible for spherical aberrations.

electron but electrons with different energies have different velocities, hence they are going to experience the deflection for a different time interval δt. This characteristic entails that parallel rays of different energies are going to be focused at different positions. In particular electrons with lower energy are going to have a shorter focal length. The spot size due to these aberration can be evaluated with the following equation:

$$d_C = \frac{\Delta E}{E} C_C \, \alpha, \tag{2.8}$$

where C_C is the coefficient of chromatic aberrations in m.

2.2 Electron Lenses

The main component necessary to build any electron optical system are electron lenses. These, as anticipated before, are elements which, on their azimuthal plane, impose a deflection to the electrons proportional to the distance from their optical axis. This deflection is a result of Lorentz force:

$$\mathbf{F} = q\mathbf{E} + q\mathbf{v} \times \mathbf{B}. \tag{2.9}$$

As can be seen from 2.9 this deflection can be generated by both an electric or a magnetic field. This property defines the two main categories of electron lenses: electrostatic and magnetic lenses. In the following, I am going to describe and simulate these components, characterizing their optical properties in terms of focusing power, image rotation and aberrations. Knowing these characteristics is crucial to design the different components comprising the multi-pass resonant cavity.

2.2.1 Electrostatic Lenses

Electrostatic lenses exploit the first term of the Lorentz force $\mathbf{F} = q\mathbf{E}$. They are comprised of stacking of rotationally symmetric electrodes with a round aperture, or bore, in the center. They exploit the electric field generated by these electrodes to deflect the electrons. In order to understand how they work it is necessary to solve the Laplace equation for a rotationally symmetric structure. In these conditions, if we know the potential on the optical axis, the resulting potential can be written as:[35, 21]

$$\begin{aligned} V(r,z) &= \sum_{n=0}^{\infty} \frac{(-1)^n}{(n!)^2} \left(\frac{r}{2}\right)^{2n} \frac{\partial^{2n} V(0,z)}{\partial z^{2n}} \qquad (2.10) \\ &= V(0,z) - \left(\frac{r^2}{4}\right) \frac{\partial^2 V(0,z)}{\partial z^2} + \left(\frac{r^4}{64}\right) \frac{\partial^4 V(0,z)}{\partial z^4} + \dots \qquad (2.11) \end{aligned}$$

Which corresponds to the longitudinal and transverse electric fields:

$$E_z(r,z) = -\frac{\partial V(0,z)}{\partial z} + \left(\frac{r^2}{4}\right) \frac{\partial^3 V(0,z)}{\partial z^3} + \dots \tag{2.12}$$

$$E_r(r,z) = \left(\frac{r}{2}\right) \frac{\partial^2 V(0,z)}{\partial z^2} - \left(\frac{r^3}{16}\right) \frac{\partial^4 V(0,z)}{\partial z^4} + \dots \tag{2.13}$$

The first electric field is responsible for the acceleration in the optical axis direction, instead the second one is responsible for the radial acceleration, hence the deflection. The first terms of the forces resulting from these field are:

$$F_z(r,z) = q\ E_z = e\frac{\partial V(0,z)}{\partial z} + \ldots \tag{2.14}$$

$$F_r(r,z) = q\ E_r = -\frac{e}{2}\frac{\partial^2 V(0,z)}{\partial z^2} r + \ldots \tag{2.15}$$

Since the longitudinal part is independent of r while the transverse one is linearly dependent on it, the deflection is going to be linearly dependent with r as well. Hence, this system behaves as a lens. In particular, the deflection is going to be dependent on the impulse $F_r \Delta t$. Therefore, it is going to be proportional to the curvature of the axial potential $V(0,z)$ and to the time spent by the electron in that field, which in turn depends on the initial velocity and the axial acceleration $a_z = F_z/m_e$ (that is proportional to the slope of the axial potential).

The curvature of the axial potential which determines the deflection can be controlled by modifying the potential of the different electrodes composing the lens stack. The curvature can be both positive or negative, which corresponds to a convergent (positive) or divergent (negative) lens effect, respectively. However, the only way to have a net divergent negative effect is to have a single electrode with a bore, and a flat counter-electrode, which corresponds to the case of an emitter or a mirror. Any higher number of electrodes is going to generate an overall positive lens effect. This characteristic comes from the fact that for any given couple of electrodes the electrons are going to experience two possible effects:

1. lower potential to higher potential: first a positive and then a negative curvature/lens effect (PN), together with an acceleration, so it is going to spend less time in the negative part, hence overall positive lens effect;

2. higher potential to lower potential: first a negative and then a positive curvature/lens effect (NP), together with a deceleration, so it is going to spend more time in the positive part, hence overall positive lens effect;

Typically when you want to design an electrostatic lens you want the electron before and after interacting with the lens to have the same energy. To achieve such a condition, you need the outermost electrodes to be at the same potential (usually the reference ground potential). To build such a system, the minimum number of electrodes is three. This kind of component is called a unipotential lens, or einzel lens. In the following, I am going to simulate an einzel lens using LorentzEM software modifying the different electrical and geometrical parameters, in order to study the dependence of the lens optical characteristics with them.

Fig. 2-3 (a,b) shows the simulation of the potential distribution of the einzel lens and the correspondent electron trajectories for an incoming beam with an energy of 5 keV, which is the energy that we intend to use in our first design of the multi-pass cavity. In this simulation the parameters used for the lens were:

1. electrode bore diameter $D = 2$ mm;

2. electrode thickness $T = 2$ mm;

3. electrode gap $G = 2$ mm.

The spherical aberration can be evaluated emitting a series of rays at different distances from the optical axis and measuring the resulting spot size after the interaction with the lens. The aberration coefficient can then be extracted using the relationship $C_s = \frac{2d_s}{\alpha^3}$, where α is the semi-angle of the marginal emitted ray.

The chromatic aberration instead can be evaluated emitting only marginal rays but with an energy spread ΔE. In this case, a spread of 2 eV was selected. Then, if the resulting spot size is measured after the interaction with the lens, the aberration coefficient can be evaluated from the relation $C_c = \frac{d_c}{\alpha \cdot \Delta E/E}$.

Fig. 2-3 (c) and (d) shows the spot size due to spherical and chromatic aberration, respectively.

Fig. 2-4 shows the result of an analysis of the behavior of the spherical and chromatic aberration coefficients and the focal length of an einzel lens while varying the potential of the central electrode. The analysis was performed both using positive

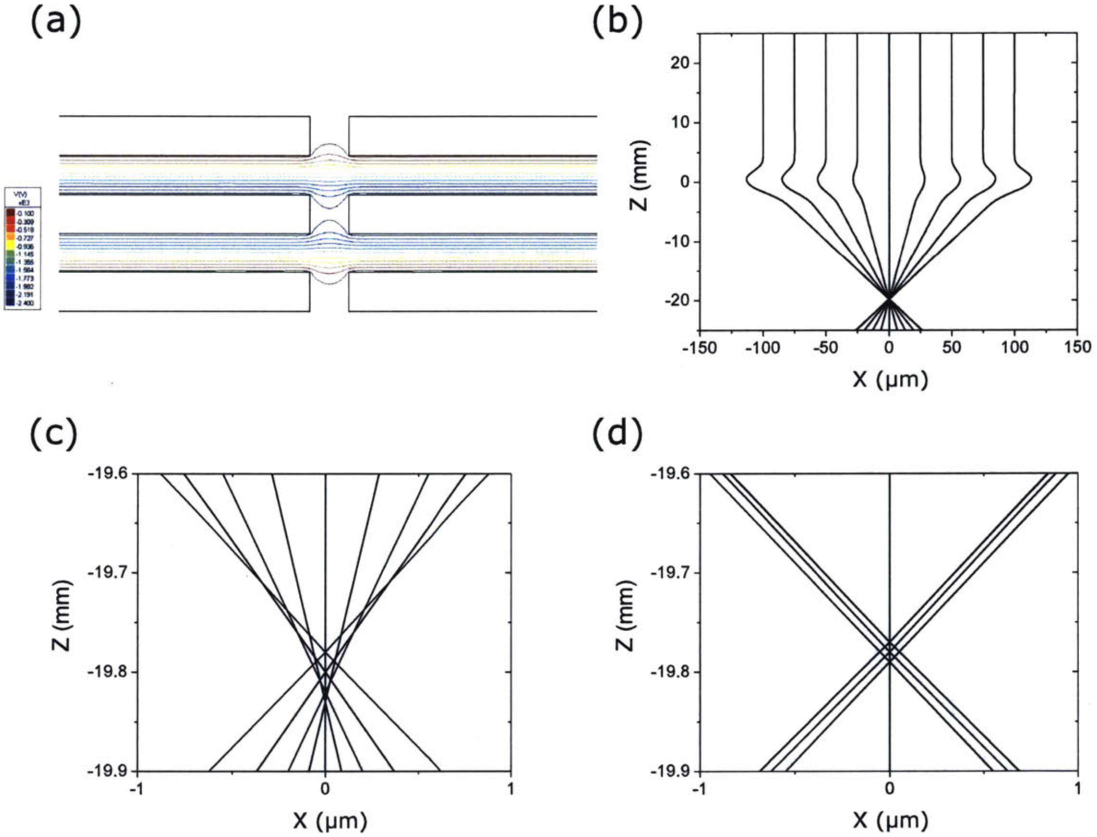

Figure 2-3: Simulation of the potential distribution and ray-tracing of an einzel lens - (a) equipotential lines and (b) trajectories simulations, performed for a structure with parameters $D = T = G = 2$ mm and $E = 5$ keV. The figure also shows the spot size due to spherical (c) and chromatic (d) aberrations.

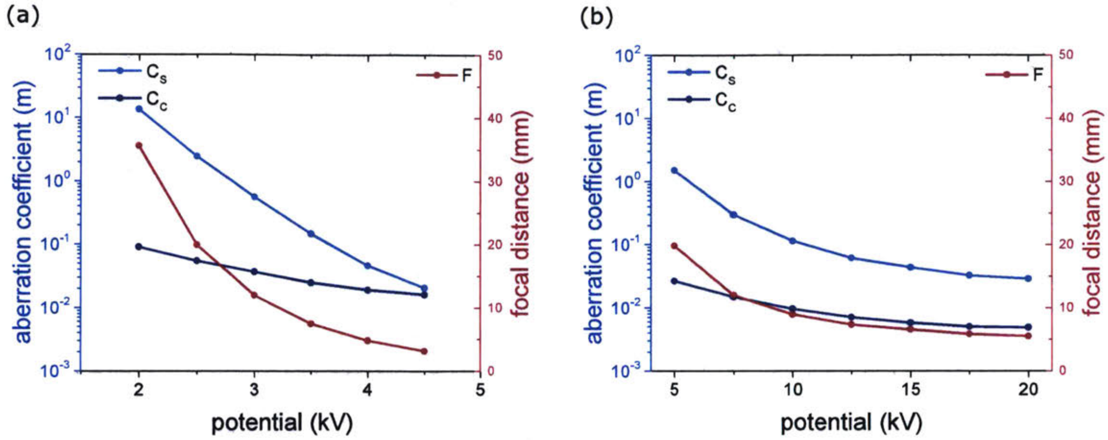

Figure 2-4: Simulation of the dependence of the optical characteristics of an einzel lens with its central electrode potential - The two graphs portray the result of the simulation showing the dependence of spherical and chromatic aberration coefficients C_S and C_C and focal distance F, while varying the central electrode potential for a negative potential (a) and positive potential (b) lenses.

and negative potentials on this electrode. In the first case, the resulting field generates a PNP lens effect while in the second case an NPN one. As we can see from the result, in the two cases, for the same focal length the aberration are comparable, but the lens with positive potential requires a much higher potential in absolute value respect to the negative potential one. This requirement is due to the fact that the positive lens accelerates the electrons so they are going to spend less time in the lens field. In both cases, as expected, the simulation shows a stronger focusing power for higher potential. Therefore, when possible, a negative potential lens is preferable since it requires using a less expensive voltage source.

The next important step for designing a lens is to know the effect of the geometrical parameter of the lens itself on its optical properties. Fig. 2-5 shows the result of this characterization performed varying the electrodes diameter, gap, and thickness of a negative potential lens. As we can see from the result, a decrease of all these parameters brings a shorter focal distance. But while decreasing the diameter and the gap also decrease the aberrations, the thickness has a very small effect on the aberrations. Therefore, using an overall smaller lens is going to be beneficial. However, we have also to consider the fact that a smaller lens is also going to be more

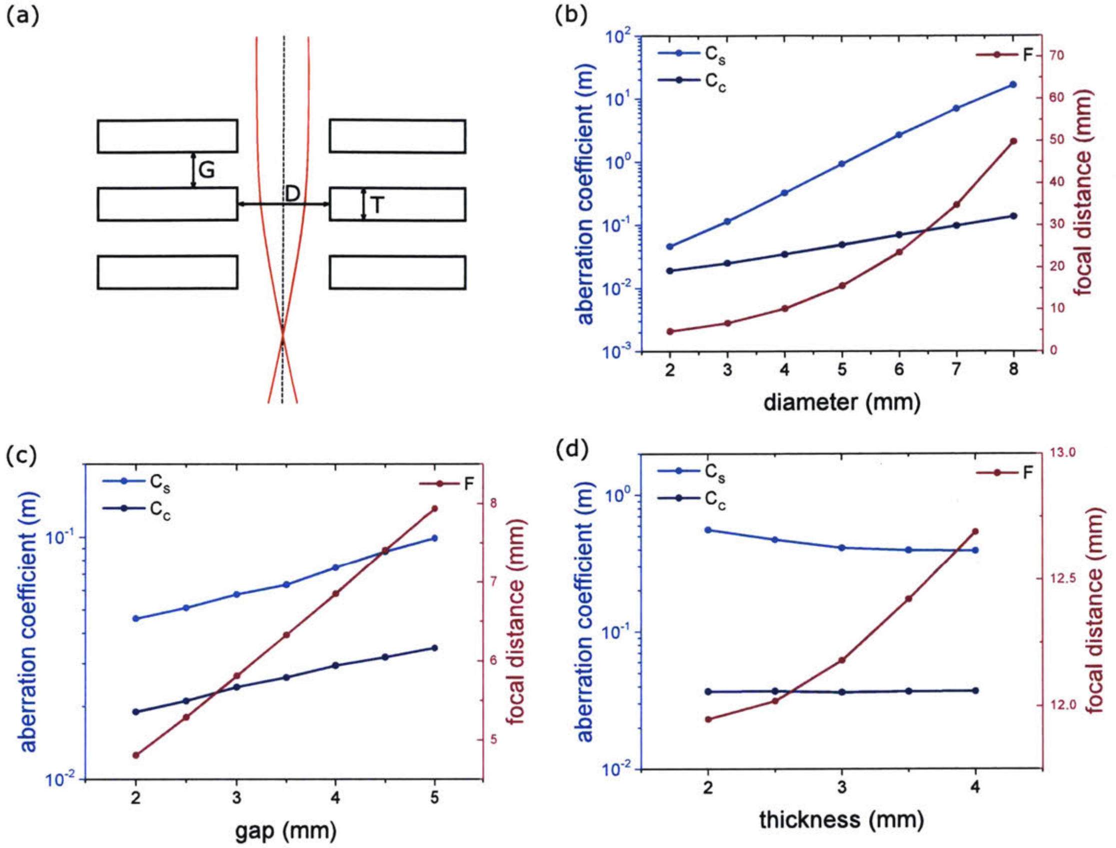

Figure 2-5: Simulation of the dependence of the optical characteristics of an einzel lens with its geometrical parameters - (a) Schematics of an einzel lens showing the parameters: diameter D, gap G and thickness T. (b-d) portrays the result of the simulation showing the dependence of spherical and chromatic aberration coefficients C_S and C_C and focal distance F, while varying these parameters.

sensible to machining errors and alignment issues. Therefore, the optimal size has to be selected keeping in mind the machining and assembling tolerances that you expect to be able to achieve.

2.2.2 Magnetic Lenses

The second main category of electron lenses is magnetic lenses. These exploit the second term of the Lorentz force $\mathbf{F} = q\mathbf{v} \times \mathbf{B}$. They are composed by a rotationally symmetric structure comprised of a copper coil winded into a yoke of magnetic material, such as iron. This yoke has a gap on the optical axis side. The two gap extremities, or pole pieces, concentrates the field in the optical axis region.

In order to understand how they work, it is necessary to solve the Laplace equation for a rotationally symmetric structure. In these conditions, if we know the field on the optical axis, the resulting off-axis longitudinal and transverse magnetic fields can be written as:[35]

$$B_z(r,z) = B_z(0,z) - \frac{r^2}{4}\frac{\partial^2 B_z(0,z)}{\partial z^2} + \dots \tag{2.16}$$

$$B_r(r,z) = -\frac{r}{2}\frac{\partial B_z(0,z)}{\partial z} + \frac{r^3}{16}\frac{\partial^3 B_z(0,z)}{\partial z^3} - \dots \tag{2.17}$$

That in paraxial approximation gives the following equation for the transverse force:

$$F_r(r,z) = m\frac{\partial^2 r(z)}{\partial z^2} = -\frac{e^2 B_z^2(0,z)}{8E}r. \tag{2.18}$$

Also in this case we can see that the transverse force is linearly dependent with r. Hence, this system behaves as a lens. It is worth noting that in this case the electron is not only focused, but it also follows a helical path, which introduces a rotation of the image plane. In particular, if we approximate the axial field with the following hat function with half-maximum width $2a$:

$$B_z(0,z) = \frac{B_0}{1+\frac{z^2}{a^2}}. \tag{2.19}$$

Then, the resulting focal length and total image rotation can be approximated respectively as:

$$f = \frac{16mE}{\pi e^2}\frac{1}{aB_0} \propto \frac{aE}{I^2}, \tag{2.20}$$

$$\phi = \frac{e\pi}{\sqrt{8mE}}aB_0 \propto \frac{I}{\sqrt{E}}, \tag{2.21}$$

where I is the total current passing through a section ($I = Ni$ with N number of windings and i current injected in the copper wire).

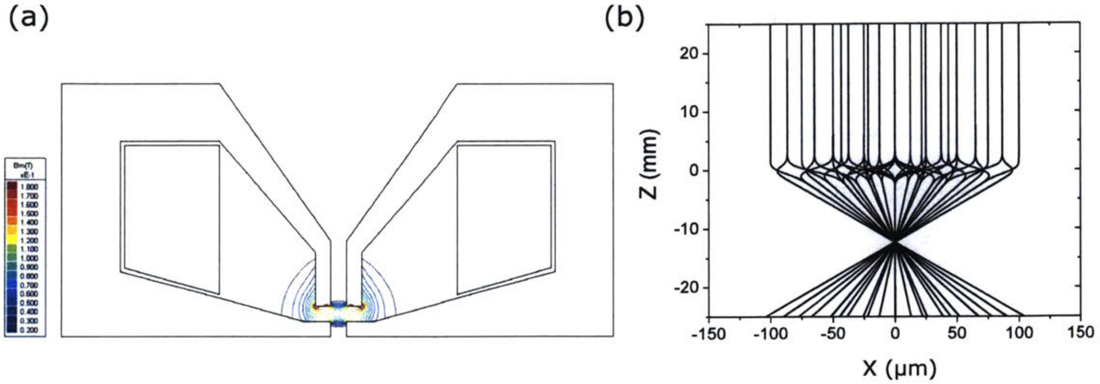

Figure 2-6: Simulation of the magnetic field lines and ray-tracing of a magnetic lens - (a) magnetic field lines and (b) trajectories simulations, performed for a structure with parameters $I = 200$ A, $D = G = 2$ mm and $E = 5$ keV.

In the following, I am going to simulate a magnetic lens using LorentzEM software modifying the different electrical and geometrical parameters, in order to study the dependence of the lens optical characteristics with them.

Fig. 2-6 shows the geometry of the simulation of the magnetic field lines distribution of the lens and the correspondent electron trajectories for an incoming beam with an energy of 5 keV. In this simulation the parameters used for the lens were:

1. total section current $I = 200$ A;
2. bore diameter $D = 2$ mm;
3. pole piece gap $G = 2$ mm.

The spherical aberration and chromatic aberrations are evaluated using the same technique implemented in the simulation of the electrostatic lenses described earlier.

Fig. 2-7 shows the result of an analysis of the behavior of the spherical and chromatic aberration coefficients and the focal length of a magnetic lens while varying the total section current I, the bore diameter D and the pole piece gap G. As we can see from the result, a higher focal distance can be achieved decreasing the current or increasing the diameter or the gap but it also result in higher coefficients of spherical and chromatic aberrations. In these simulations, I also evaluated the additional image rotation with respect to that of a standard optical lens, which is π. The results are summarized in Table 2.2. The simulation showed that these values are practically independent on the geometry. They only have a linear dependence with the current, which is consistent with what found in Eq. 2.21.

Table 2.2: Image rotation dependence with the total section current

I (A)	ϕ (deg)
100	15.06
200	30.12
300	45.18
400	60.27
500	75.36
600	90.40

2.3 Gated Mirror

In order to be able to build a linear cavity for electron, we need to develop components that can define a cavity, acting as mirrors when the electrons are inside the cavity. For a linear cavity, such components should also to be able to be gated so as to let the electron enters into the cavity and exit from it after having completed the required number of roundtrips. We are going to refer to this component as a gated mirror. The main working principle of a gated mirror is that when it has to act as a mirror it generates a potential in the beam path higher than that used to accelerate the electrons. Instead, when it is necessary to couple electrons in and out of the cavity this potential is lowered so to let the electrons pass through. This concept was first proposed for quantum electron microscopy by Kruit et al. in [16] where such an element is referred to as "barn door".

A design of a gated mirror for multi-pass microscopy has to take into account some important factors:

1. it has to be operated faster than the roundtrip time of the electron in the cavity, otherwise resonance cannot take place. To meet this specification, the system

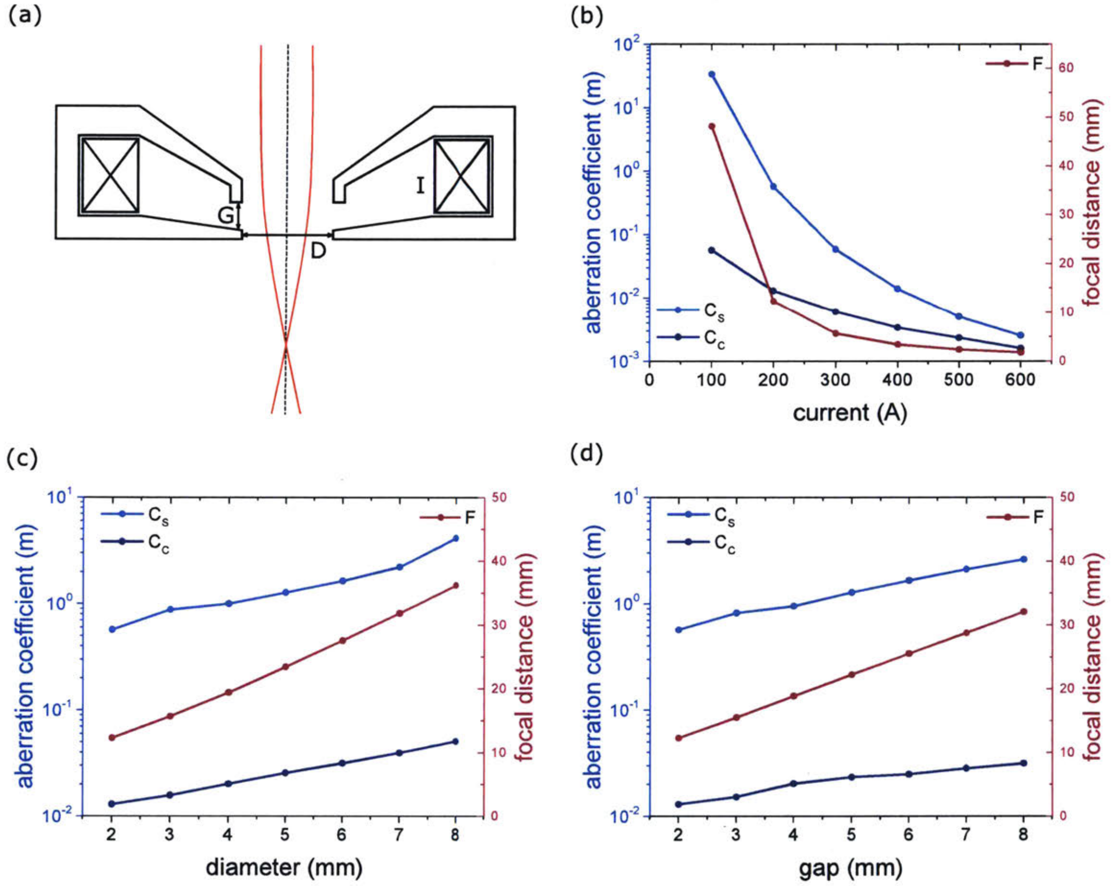

Figure 2-7: Simulation of the dependence of the optical characteristics of a magnetic lens with its total section current and geometrical parameters - (a) Schematics of a magnetic lens showing the parameters: current I, diameter D and gap G. (b-d) portrays the result of the simulation showing the dependence of spherical and chromatic aberration coefficients C_S and C_C and focal distance F, while varying these parameters.

has to be matched with an external pulse generator that has to be designed so to generate pulses of hundreds of volts at the ns timescale.

2. it has to minimize the effect of aberrations because they will build up with the number of roundtrips, disrupting the achievable resolution. To meet this specification, the geometry of the gated mirror has to be accurately designed. As we will see in the following sections, a successful approach is to build aberration corrected mirrors. This technique is well established for standard electron mirrors [30, 31, 32, 33] and its implementation for gated mirrors has been proposed,[34] but not experimentally demonstrated yet.

In the following sections, some gated mirror designs are proposed and the gating mechanism is verified through simulation. Then the possibility of upgrading the system to include an aberration-correction feature is discussed analyzing the characteristics of hyperbolic mirrors.

2.3.1 Design and Simulation of a Gated Mirror

The simplest gated mirror that we can design is comprised of a stacking of three electrodes insulated from each other, where a concentric aperture is drilled at the center of each of them. The central electrode has to be connected to a potential high enough so that at the center of the structure the potential is higher with respect to the electron energy. The external electrodes are instead grounded. The central electrode is also connected to a pulse generator which when activated lower the potential of the central electrode letting the electron pass through. The first simulation that was performed is a COMSOL RF time-dependent analysis of the gating mechanism in this base level structure.

The COMSOL model for this simulation was built integrating electromagnetic waves, electrical circuit and charged particle tracing modules. Fig. 2-8 illustrates the COMSOL model that was implemented. The electrodes used in this model have gap $G = 2$ mm, bore diameter $D = 1$ mm and thickness $T = 1$ mm. The electron energy used is $E = 3$ keV and the central electrode potential is kept to -3700 V.

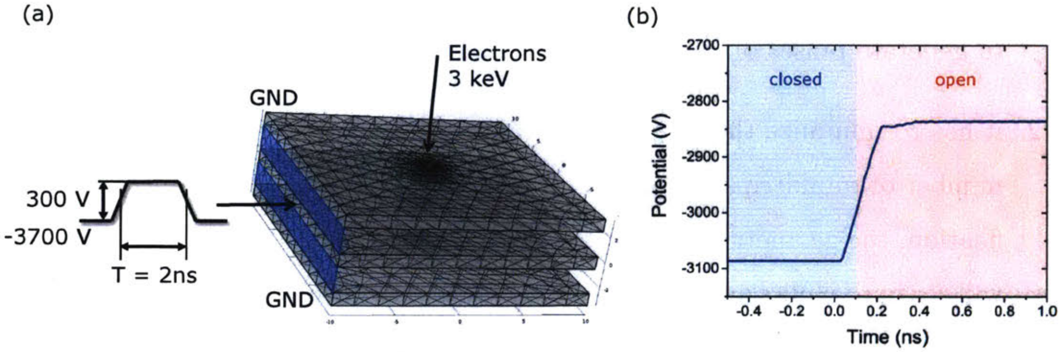

Figure 2-8: COMSOL model of a three-electrode gated mirror and potential at the center of the structure - (a) TDTS model: mesh distribution and lumped ports of the external pulse generator. The structure is matched with the external circuitry. (b) The potential at the center of the structure.

A 300 V pulse 2 ns long with 100 ps rise time is then applied between the central and the external electrodes which opens the gate. A scattering boundary condition is applied to the external boundary of the model to avoid reflections. The device is matched with the external circuitry using a parallel plate model for the characteristic impedance (i.e. $Z_{in} = Z_0\frac{d}{w}$). Fig. 2-8 (b) shows the simulation of the potential at the center of the structure. When this potential goes below -3000 V the gate is open.

Fig. 2-9 illustrates the result of the time-dependent trajectory simulation of the electron beam marginal rays. It is worth noting that the electron in-coupling while lowering the potential has an effect on electron trajectories, therefore a very sharp pulse and a pulsed electron source is required. In this way, the electrons will interact only in the time period when the gate is fully closed or fully open. To avoid ringing or minimizing its effect it is also important to operate the system when it is stabilized, to match as well as possible the gate with the external circuitry and/or to adopt some strategy of active compensation or feedback.

In order to have better control of the trajectories during resonance, in-coupling, and out-coupling, it is beneficial to add two electrodes between the grounded external electrodes and the central one, biased at an intermediate potential between the two. Fig. 2-10 shows a possibility for this 5-electrode configuration. In this setup the electrode parameters are: gap $G = 1.5$ mm, thickness $T = 1$ mm and bore diameter

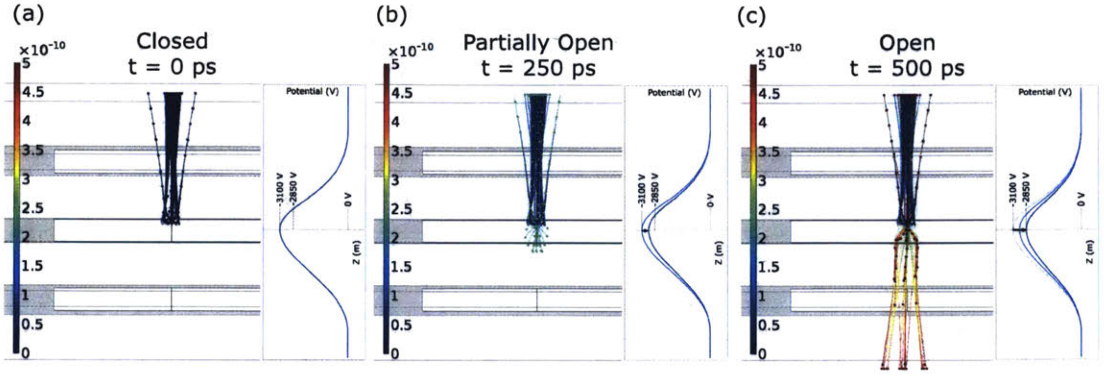

Figure 2-9: COMSOL particle trajectories simulation during gating operation - (a-c) show the electron trajectories simulated using COMSOL particle tracing module at different simulated times.

D = 3 mm. In this figure, the results of the simulation are shown in terms of the equipotential lines in this structure, and the axial potential and the electron trajectories in closed and open configuration. The open configuration is achieved by applying a 150 V pulse to the central electrode.

It is not sufficient to simulate the DC operation of the gated mirror. An RF analysis it is also necessary in order to establish if this structure can be operated at the required speed or if the capacitance of the electrodes is going to prevent the high-speed operation. To do so a 3D COMSOL model was built, imagining a possible implementation of the structure. Fig. 2-11 (a) shows a cross-section of the simulated geometry, where the potential pulse is applied with a matched coaxial cable connected with a pin going to the central electrode and the grounded external conductor is connected to the external shielding of the structure, that is also connected to the two external electrodes. The pulse is applied from the left side of this structure as can be seen from the picture. In this structure, the electrode can be isolated from one another and the whole system can be held together using insulating spacers of cylindrical or spherical shape. Fig. 2-11 (b) is a simulation of the axial potential at the center of the core electrode. As can be seen from this simulation, with this design, a pulse of 100 V have a time constant of few ns. Since the electron pulse has to interact with a potential as stable as possible, a good choice would be to time

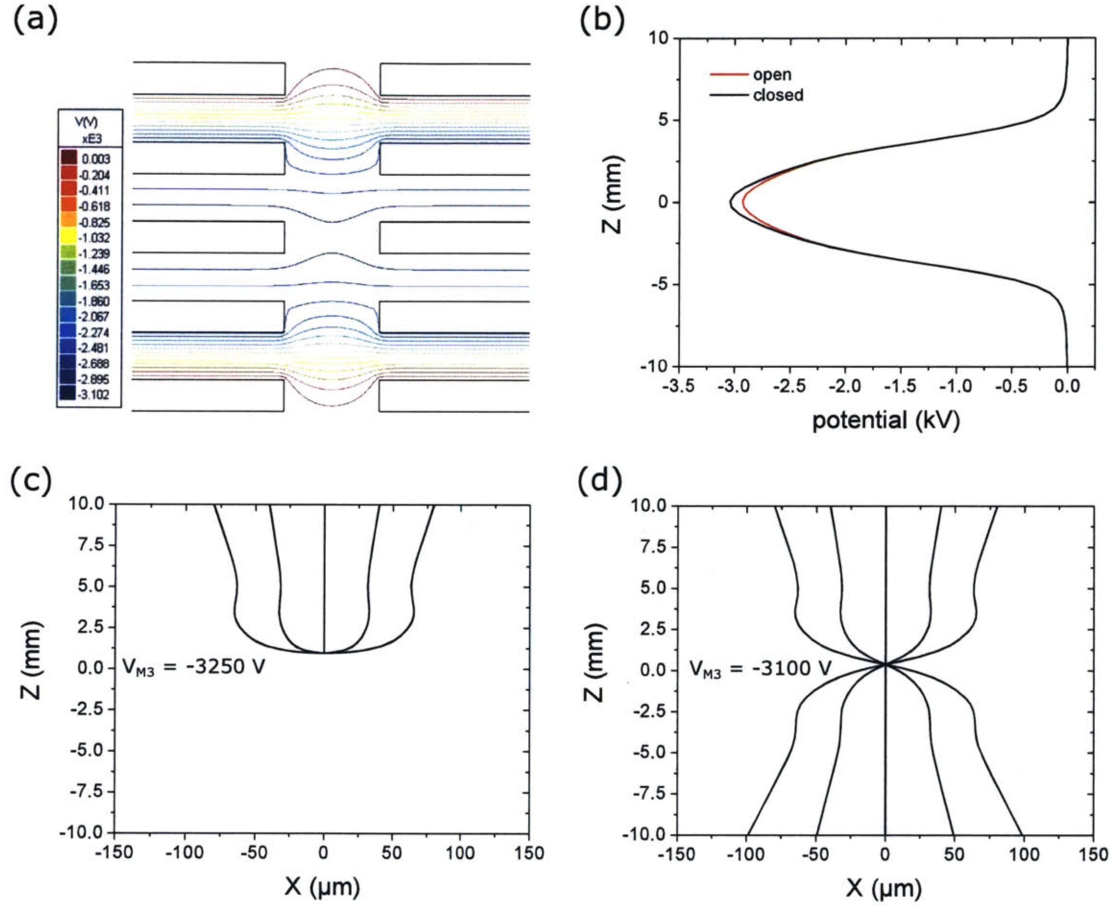

Figure 2-10: DC ray-tracing simulation of a five-electrode gated mirror in open and closed condition - (a) Geometry and potential distribution of the electron gated mirror. The multi-colored lines indicate equipotential surfaces. The potential used for the simulation are the following: $V_{\mathrm{M1}} = V_{\mathrm{M5}} = 0$ V, $V_{\mathrm{M2}} = V_{\mathrm{M4}} =$ -2490 V, V_{M3} = -3250 V. The applied pulse is of 150 V. The geometrical parameters used are: gap $G = 1.5$ mm, thickness $T = 1$ mm and bore diameter $D =$ 3mm. (b) Axial potential at the electron gate in open and closed configuration. (c) Raytracing simulation in closed condition.(c) Raytracing simulation in open condition.

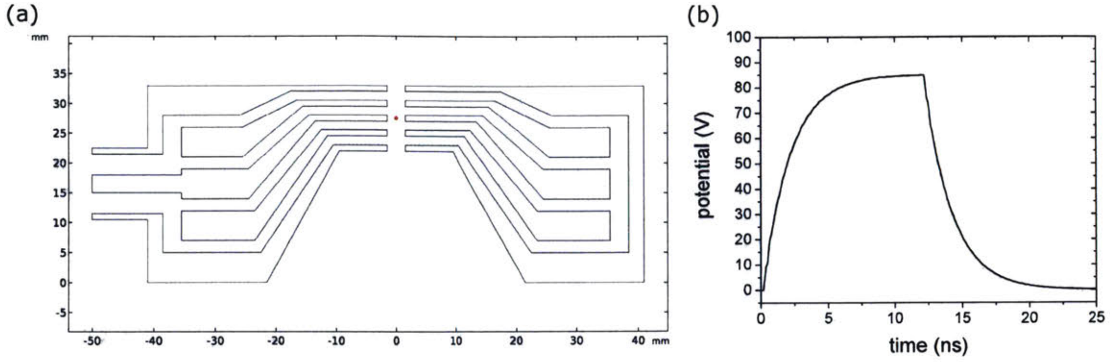

Figure 2-11: Geometry of the COMSOL model of the gated mirror prototype and simulation of the central potential - (a) illustrates the simulated geometry with the input for the electrical connection done with a coaxial cable on the right. (b) shows the simulated axial potential at the center of the middle electrode. This is evaluated doing a line integral of the field from the field free region. The point at which the potential is evaluated is highlighted in red in (a).

the electron pulse to reach the gate in the time frame 9-12 ns from when the pulse is generated. After this moment the system needs other 10 ns to restore the closed configuration. Therefore, the cavity has to be long enough so that the time required for an electron to do a roundtrip is more than 10 ns. If this constraint were to be too limiting, alternatively, the design can be modified so as to have a smaller device, hence a smaller capacitance and a smaller time constant. This modification can be done maintaining the same geometry close to the optical axis so that the optical properties would not be affected. Here, this particular design was used because these are the dimensions that were used to build the first prototype, which will be described in the next section.

Fig. 2-12 instead illustrates the field distribution inside the structure at different times when the pulse is applied. The field is shown at 2 ns, 4 ns, 8 ns, and 16 ns. The potential is applied from external circuitry which is matched to the coaxial cable connected to the central electrode and the external shielding. The coaxial cable has an internal conductor of diameter $d = 3$ mm and an external conductor of diameter $d = 10$ mm, hence its characteristic impedance is $Z_0 = \frac{138}{\sqrt{\epsilon}} \log(D/d) = 72.2\,\Omega$. Therefore the external circuit is simulated using its Thevenin's equivalent: a pulse generator and a $72.2\,\Omega$ resistor.

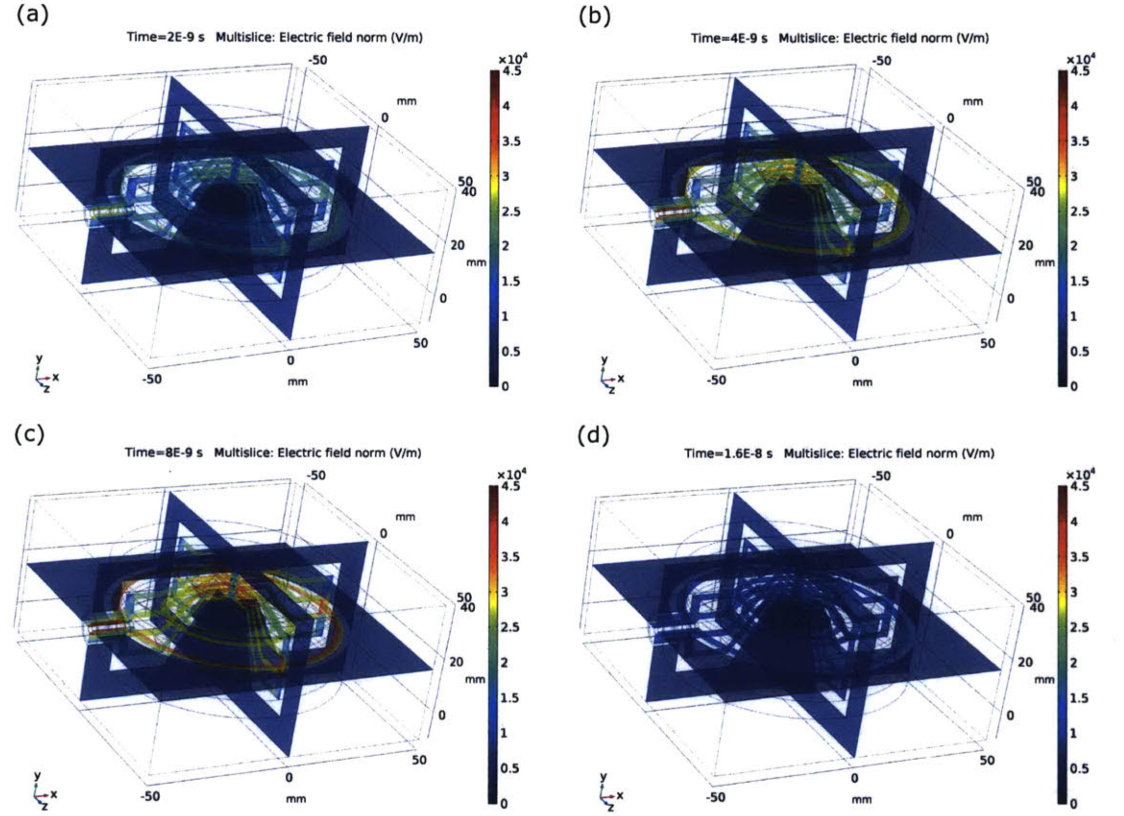

Figure 2-12: Field distribution simulation at different instants - (a-d) show the field distribution in different cross sections of the device at 2 ns, 4 ns, 8 ns and 16 ns, respectively.

2.3.2 Assembly and Preliminary Testing of a Gated Mirror

In order to develop and experimentally demonstrate a working gated mirror, it is necessary to take into account some more practical aspects of the design, such as the machining tolerances, the assembly, the alignment between electrodes, the shielding, the connections, and the testing. All these elements have to be taken into account to build an effective component. Before machining, a CAD model of the piece was developed using Autodesk Inventor.

Fig. 2-13 (a) shows the CAD drawing of the designed piece. The electrodes are shaped so as to permit an easy connection with the wires coming from the power supply. The insulation and alignment between the electrodes are done using three Al_2O_3 balls that sit in concentric grooves, present both on the bottom and on the top plate of each electrode. These grooves ensure the radial position of the balls. The angular position instead is secured by three notches at 120 deg from each other, present on the top surface of each electrode. Therefore, each ball has a total of 4 points of contact: 3 on the bottom plate and 1 on the top one. The alignment done with insulating balls is the most precise. For this reason, this alignment scheme was preferred with respect to the use of insulating rods and spacers, the other common alternative. The structure is shielded and kept in place by a grounded aluminum shield, which has a specific hole for the electrical connection, performed with pins screwed into the electrode and connectors fastened to the wires. The machining of the individual electrodes was outsourced to an external supplier. All the electrodes were machined in 316 stainless steel which is non-magnetic. Fig. 2-13 (b) and (c) shows the resulting pieces after assembling them, before and after securing the shield.

Once the system was assembled a frequency test was performed using a network analyzer,[1] connecting the probe to the central electrode and the ground to the external shell. Fig. 2-14 shows the result of this measurement. This graph portrays the frequency behavior of the S_{11} parameter of the structure, that is to say, the ratio between the reflected and incident power. We can see that this specific prototype cannot be used above 1 GHz because higher frequencies would cause resonance, hence

---

[1] I would like to thank John Simonaitis for his help in performing this measurement.

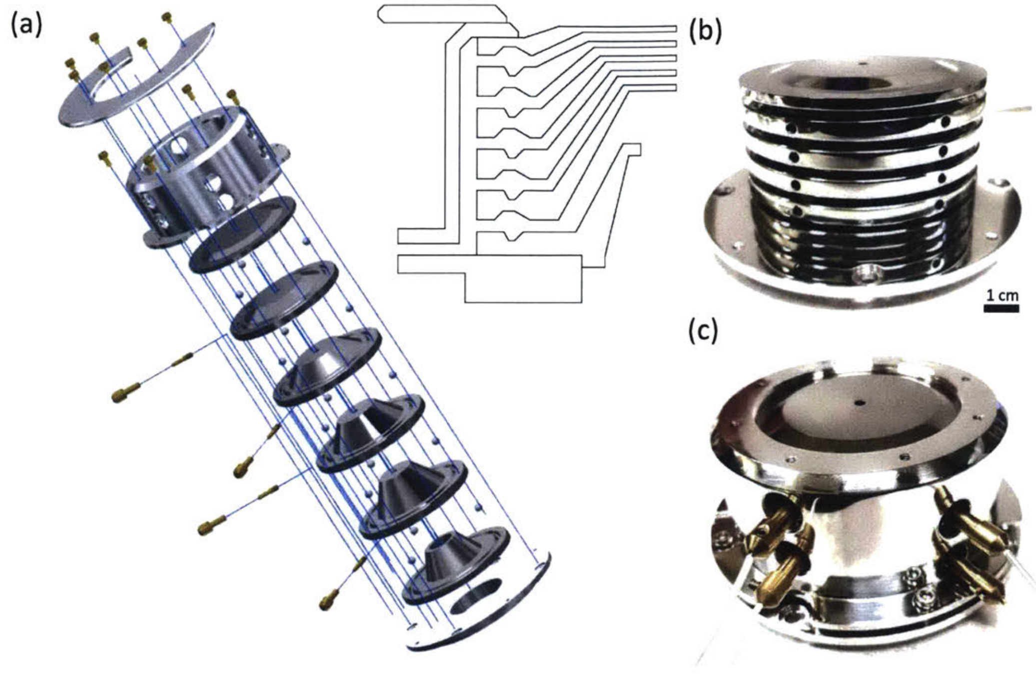

Figure 2-13: Gated mirror prototype - CAD exploded view with inset of the section (a) and assembled the prototype, before (b) and after (c) the mounting of the shield and the electrical connections.

ringing. This limitation is probably not an issue since we expect to use pulses of the order of few nanoseconds. However, there is also a peak at 100 MHz that could disturb our operation. Further analysis will be necessary in the future to understand if this is an artifact of the connection or it is real, and if it is, whether it can cause sufficient ringing in the potential of the gated mirror to disturb the electron trajectories.

The next step was to place the device in the SEM chamber to check the alignment between the plates. Fig. 2-15 shows a machining precision in each piece which respects the manufacturer tolerances of 10 µm. However, the alignment within plates is of the order of 200 µm, which is not acceptable to get low enough aberrations not to distort the beam path and shape significantly.

For this reason, once the device was assembled the central aperture was enlarged to a bore of 3.5 mm, but done simultaneously for all the electrodes so that the alignment would be the best we can get. The hole was done mounting the device on a lathe

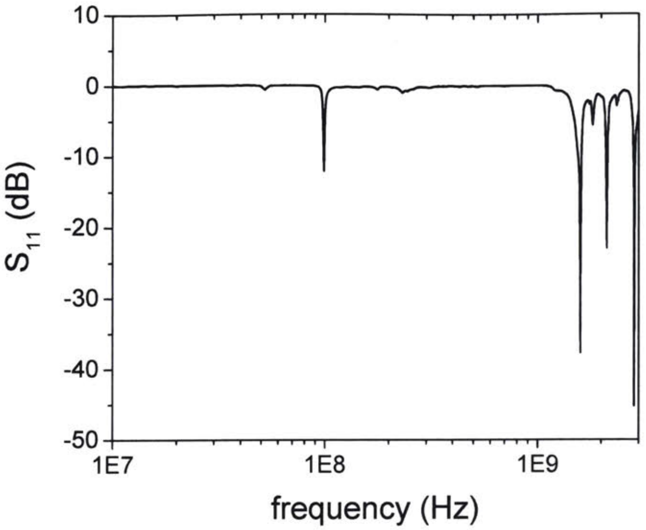

Figure 2-14: S_{11} parameter measurement of the gated mirror prototype using a network analyzer - The frequency dependence of the S_{11} parameter shows a flat range of frequencies at which the device can be operated up to 1 GHz, except for a resonance peak at 100 MHz.

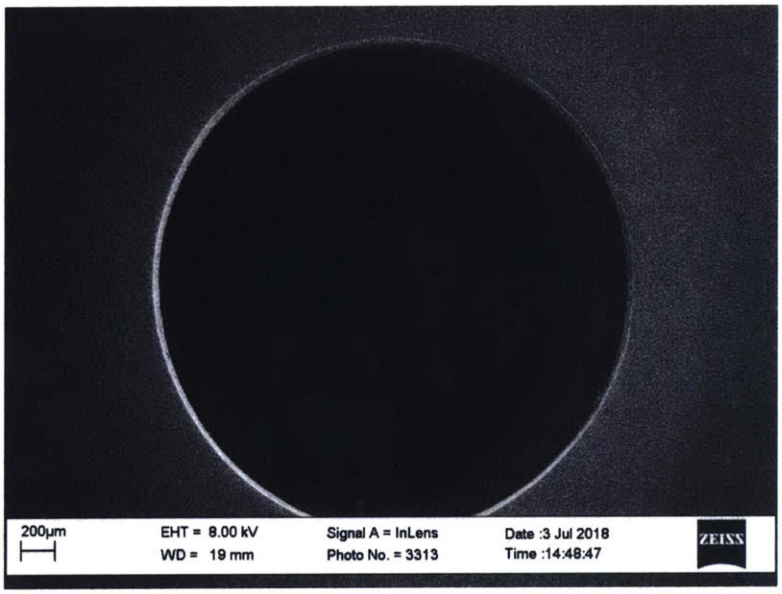

Figure 2-15: SEM of the prototype to asses the alignment precision between the different electrodes - The SEM image show a misalignment between the different plates of the order of 200 µm.

adopting a two-step process, first using a drill bit and then a reamer.[2] Fig. 2-16 shows the device mounted on the lathe used for this procedure, and an SEM image of the final result. As can be seen, the alignment between the holes is extremely improved with respect to that shown in Fig. 2-15. The only problem with this procedure is that it leaves behind burrs, even after sonication in IPA. For this reason, in the future, it will be necessary to come up with some procedure for the deburring such us electropolishing or using some specifically designed tool. Alternatively, the device could be disassembled, polished and reassembled. However, this procedure is expected to introduce some misalignment.

The next step consists in the DC testing of the device. A very efficient way to test if the alignment is good enough, so that the device behaves as expected and can be used as a gated mirror, is to perform a mirror image measurement as described in [36]. The quality of the mirror image is going to be a benchmark for the overall alignment and machining precision of the gated mirror. This experiment can be carried out as follows[3]:

1. negatively bias the fourth electrode to bring the gate to a closed configuration;

2. place a sample in the beam path, in between the SEM objective lens and the gated mirror. This procedure was done mounting a TEM sample grid on a 3 axis nano stage placed into the SEM. The sample used was comprised of a copper grid covered with graphene on lacey carbon with sprinkled TiN nanoparticles on top;

3. put the beam in scanning mode and focus onto the sample;

4. tweak the potential of the other electrodes up to the point when the reflected beam is focused on the bottom of the sample. This condition can be recognized because it is going to show an image of the bottom surface of the sample together with the top one.

---

[2] I would like to thank Brenden Butters for his help in performing this procedure.

[3] I would like to thank Navid Abedzadeh for his help in setting up this experiment.

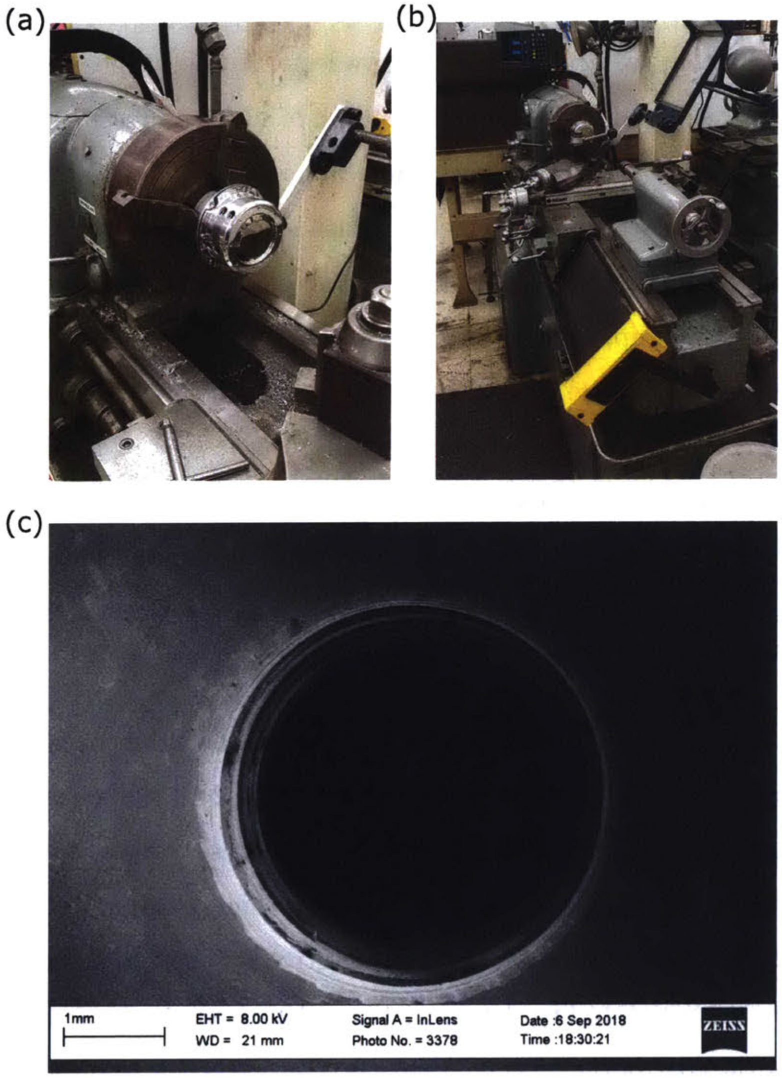

Figure 2-16: Lathe re-drilling of the central bore and new alignment assessment - (a) and (b) shows the mounting of the prototype on the lathe, used to drill and then ream the new central bore to achieve better inter-electrode alignment. (c) is an SEM of the modified prototype exhibiting an improved alignment, that is now lower than 10 µm. However, burrs are now visible at the edges of the apertures.

Fig. 2-17 shows the experimental setup and Fig. 2-18 illustrates the result of a scanning measurement with the gate in the closed configuration before placing the sample in the beam path. In this picture, the reflected beam is re-focused at the position of the objective lens. In fact, we can see at the center of the structure an image of the bottom surface of the objective lens. It is even possible to appreciate the scratch on this metal surface. The recording of such an image is possible because the electrons which are reflected back are scanned onto the objective lens surface, they hit it producing secondaries which are then sucked up by the bias of the in-lens detector in the column and detected. The central region is instead black because those electrons in their way up, they go into the objective lens aperture without producing secondaries. Since they have the same energy of the incoming beam (i.e. 3 keV), they are too energetic to be attracted by the small positive bias of the in-lens detector. Hence, they are not detected and we see a dark region. The fact that this area is not perfectly circular is already an indication that there is some misalignment or tilting of the device with respect to the column, or between the electrodes composing the device itself.

The next step consists in bringing the sample in the beam path using the nano stage and follow the procedure previously listed. Fig. 2-19 shows some SEM images acquired using this technique. As can be seen from these images, both the front and the back side of the sample are captured in the same frame. While far from the gated mirror optical axis the reflected image is strongly aberrated, close to the center it is possible to appreciate fine details of the order of hundreds of nanometers. The aberration at the edge of the reflected image is most likely due to misalignment/tilting and to the fact that since we are not imaging the pivot point of the beam scanning on the mirror, the beam is most likely scanning on the mirror potential surface, which is not flat. Hence, it will generate aberrations. Another important fact to notice is that we are not in a regime of point symmetry, which, as pointed out by N. Abedzadeh in [36], means that in a perfect alignment condition would imply that the direct and reflected images should overlap. Therefore, the lack of overlap between these two in the recorded image is an indication that the device may be slightly tilted. Therefore,

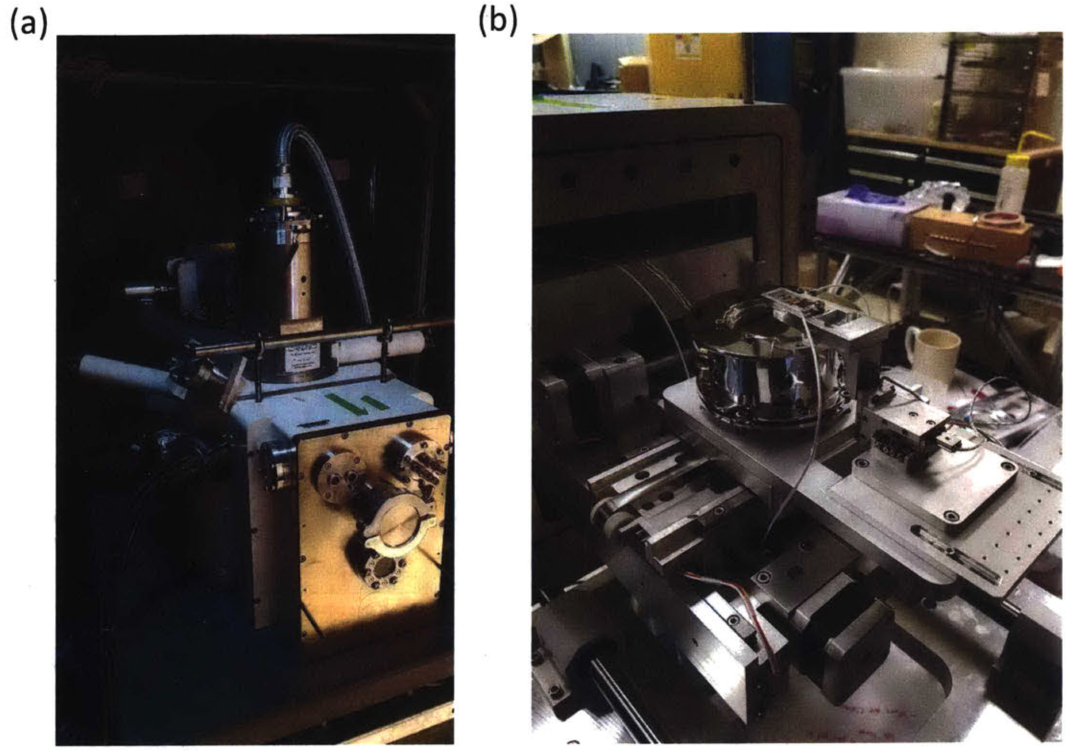

Figure 2-17: Experimental setup used for the characterization of the prototype in mirror condition - (a) Modified SEM tool used for the experiment (a) and assembly of the experiment (b) .In the latter image, it is possible to see the device mounted on the heavy-duty stage of the SEM custom door. A nano stage is used to place a sample above the gated mirror. The SEM is a modified LEO 1525 with a Gemini column.

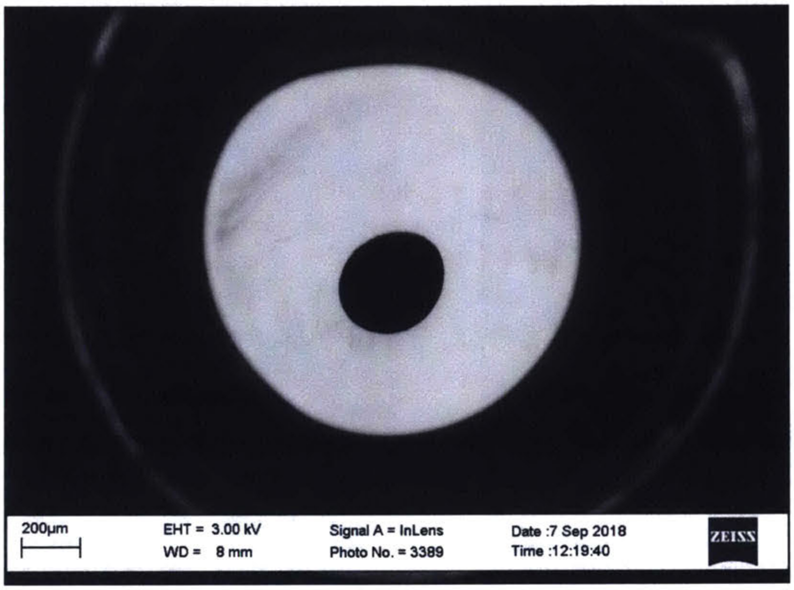

Figure 2-18: Image acquired scanning on the gated mirror in closed configuration - The picture is acquired tweaking the closed gated mirror potentials so to refocus the reflected beams on the objective lens. For this reason at the center of the structure is possible to see the objective lens bottom metallic surface and its aperture. This image is produced by the secondary electron generated by the reflected beam hitting the objective lens. The fact that distortions can be seen in the image is an indication that some misalignment or tilting of the device are present.

in the future, it would be beneficial to build or acquire a tilting stage where to install the gated mirror in order to compensate for this issue.

2.3.3 Hyperbolic Mirrors

As we saw in the previous sections all the elements that we incorporate in our design are going to introduce aberrations. In a normal microscope, the presence of these aberrations is going to generate issues only when you try to reach extremely high resolutions, especially because typical TEM works at very high energies. Electrons are usually accelerated to 200-300 keV. Unfortunately, in our system, we are using lower energies and we want the beam to make multiple round trips inside the cavity. Therefore, the beam is going to interact many times with each element composing the linear cavity, accumulating aberrations at each round trip. The consequence is a progressive degradation of the resolution during resonance. For this reason, it would be beneficial for our design to compensate for aberrations at each round trip. In this section, the modification of the gated mirror geometry to incorporate an aberration correction feature is discussed, and the characteristics of such a system are evaluated through simulation.

In 1936 Otto Scherzer demonstrated that spherical and chromatic aberration, regardless of the fabrication precision, cannot be eliminated by improving the quality of the lenses and that for an electrostatic round lens the aberrations do not change sign (Scherzer's Theorem).[27] Inducing an opposite sign of aberration is possible through one of the following means:

1. breaking the rotational symmetry exploiting multipoles fields [37, 38]
2. introducing orthogonal symmetries using elements such as mirrors [30, 39]
3. using time-varying potential with pulsed beam [40]
4. introducing space charges on the electron optical axis placing a conducting foil or a mesh in the beam path [41]

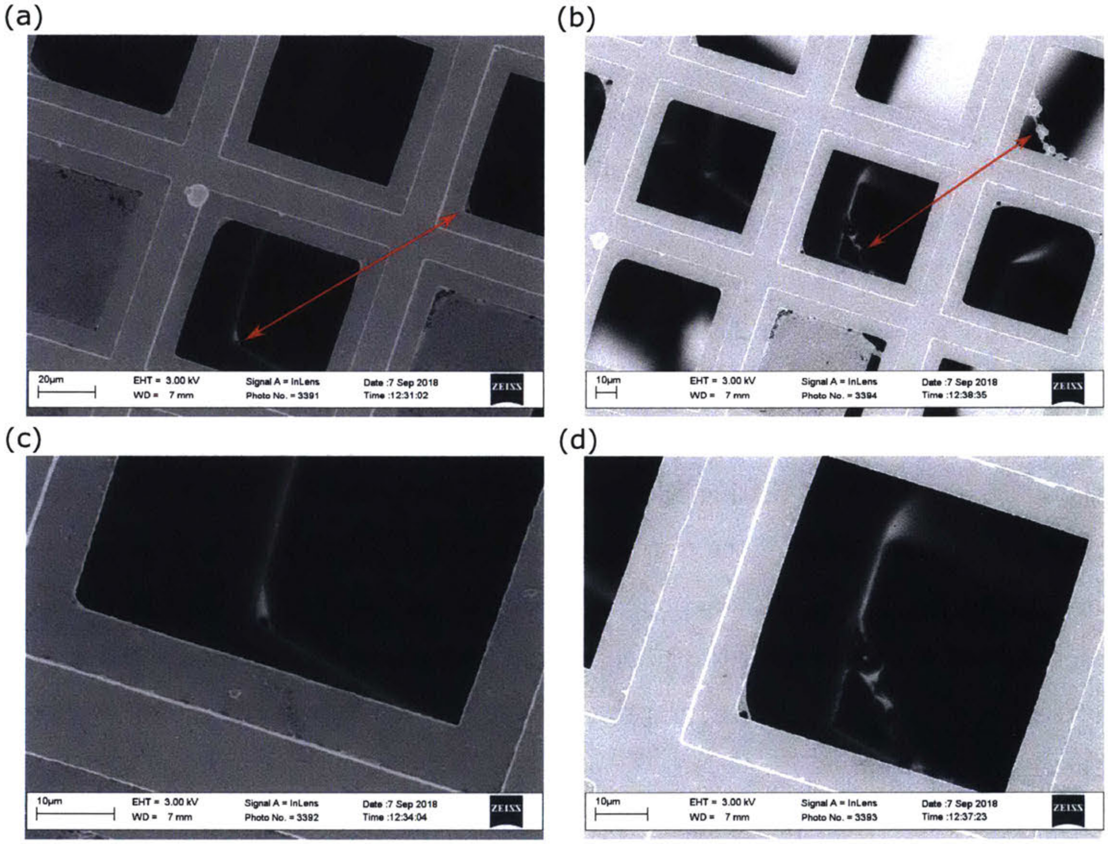

Figure 2-19: Image of the front and back side of a sample placed above the gated mirror in closed configuration - This measurement is obtained scanning the beam on the closed gated mirror in a condition where both the incoming beam and the reflected one are focused at the mirror plane. The quality of the back image, which comes from the reflected beam is an indication of the alignment quality. Since it is possible to resolve details of hundreds of nm the alignment is good. However, the aberration far from the optical axis and the fact that the reflected image is not at the same position as the direct one is probably an indication of tilting of the device. (a) and (b) shows highlight the correspondence of some detail between the direct and reflected image, which allows quantifying the non-overlap between the two images, that is about 100 µm. (c) and (d) instead shows the same details in the reflected image, magnified.

The third method had not been demonstrated, and the fourth method induces inelastic scattering, resulting in the loss of intensity. Correction using multipoles is currently well established in aberration-corrected TEM. However, this technique is not very stable and requires continuous tuning of the correction fields. For these reasons, in the following, the implementation of the second method to our system is discussed. Aberration correction using a mirror in a linear electron reflector was first proposed by [42]. I would like to thank our collaborators in the Stanford team to point out the possibility of implementing this method in the gated mirror design.

A hyperbolic mirror works by generating a hyperbolic potential in the region where the electrons are reflected. Such a potential is able to focus the reflected paraxial rays stronger than the marginals, and the high energy electrons stronger than the low energy ones, which is equivalent to saying that this kind of potential shape can generate spherical and chromatic aberrations with a negative coefficient. An important characteristic of hyperbolic mirror that we have to take into account in our design is that for the hyperbolic mirror to be effective in correcting the aberration, the diffraction plane has to be at the mirror surface. The intensity of the correction depends on z_0, the position of the image plane. z_0 is determined by the potential distribution inside the structure. For this reason, this device can be used as a tunable corrector for spherical and chromatic aberrations. Moreover, the value of the C_s scales as M^4.[33] Therefore, with a larger numerical aperture, it is possible to increase the strength of the correction considerably. In standard triode hyperbolic mirrors, the wedge electrode potential represents an additional degree of freedom for tuning the correction, as it can move the position of the mirror surface. However, in our system, we have some additional constraints because the gated mirror must assure the in-coupling of the beam. Consequently, the wedge electrode potential is limited to few hundreds of volts above the 5,000 V corresponding to the potential to which the electrons are accelerated, otherwise we would require too big a pulse for the in-coupling.

Fig. 2-20 (a) shows the potential distribution of a possible design of hyperbolic gated mirror. In this design the wedge electrode is chosen with a slope of $\sqrt{2}$, a distance between the center of the structure and the second electrodes of $G_1 = 15$ mm and a gap between these electrodes and the outermost ones $G_2 = 4.5$ mm. The potentials applied to the structure are, from the central electrode outward, $V_0 = -5200$ V, $V_1 = -3000$ V and $V_2 = 0$ V. Fig. 2-20 (b) is a ray-tracing simulation of an electron beam coming from the bottom of the structure, focused at 20.75 mm from the center of the gated mirror and reflected back at the same position. After the reflection, the beam exhibits negative spherical and chromatic aberration. In particular, in this configuration, the aberration coefficients of the reflected beams are $C_S = -672$ mm and $C_C = -555$ mm.

Fig. 2-20 (c) and (d) illustrate the result of the focal distance and aberration coefficients simulation while varying the potentials of the central electrode V_0 and that of the second electrode V_1. We can see from these result that an increase of these potentials in both cases entails a larger focal distance, but while a higher V_0 implies a higher correction, the opposite is valid for V_1. These simulations show that this device can be effectively used to tune the correction of the aberration, which gives us higher freedom in the design.

As previously anticipated, also the geometry of the electrodes is going to influence the amount of correction that the device can provide, which has to be matched to the aberrations introduced by the other elements of the cavity. In particular, Fig. 2-21 analyze the influence of the relative distances between the electrodes, G_1 and G_2. From these simulations, we can conclude that in both cases a larger gap corresponds to a larger correction, but while G_1 has also a significant impact of the focal length, the effect of G_2 on this property is negligible.

2.4 Electron Pulse Generation

For the system to work it is necessary to in-couple into the linear cavity a very short electron pulse. Otherwise, the electrons would interact with the gating potential when this is still not stable, i.e. during the rising and falling time of the pulse and during the possible ringing of the axial potential due to the resonance of the gated mirror at

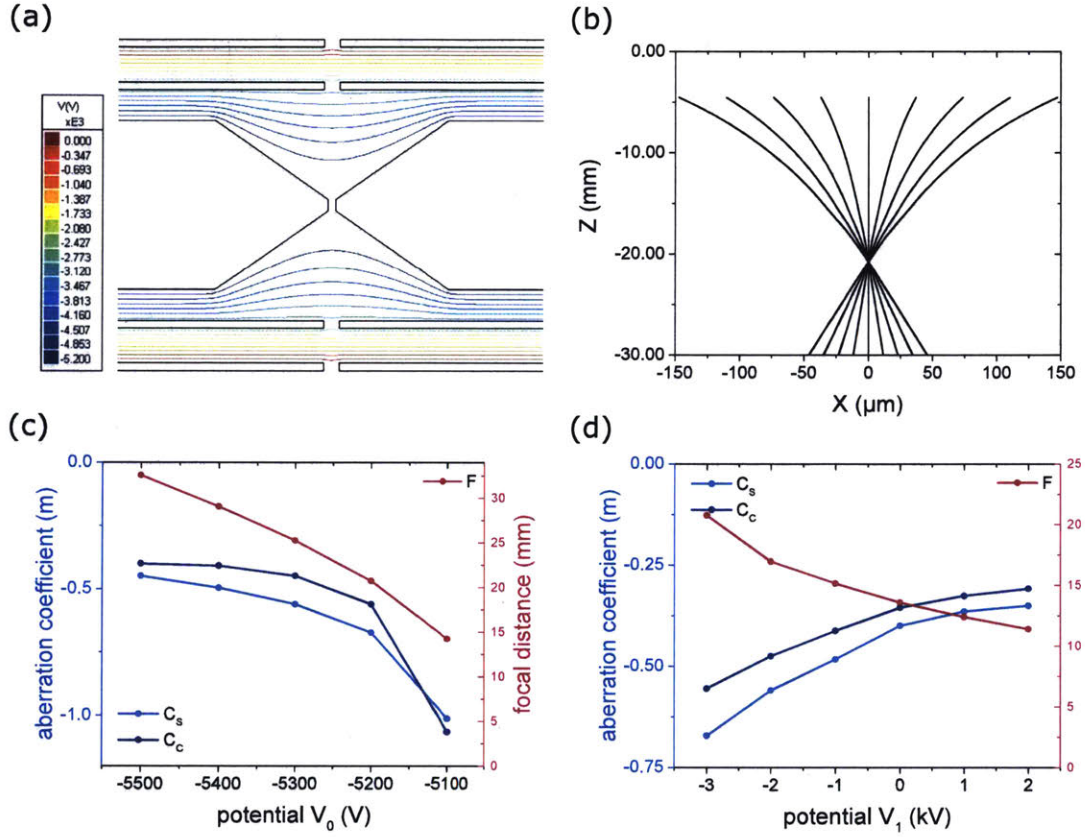

Figure 2-20: Simulation of an hyperbolic gated mirror and influence of the potential configuration - The potential distribution (a) and the electron trajectories (b) of an hyperbolic gated mirror with $G_1 = 15$ mm, $G_2 = 4.5$ mm, $V_0 = -5200$ V, $V_1 = -3000$ V and $V_2 = 0$ V are simulated. The influence of V_0 and V_1 on the system optical properties is also analyzed in (c) and (d) respectively.

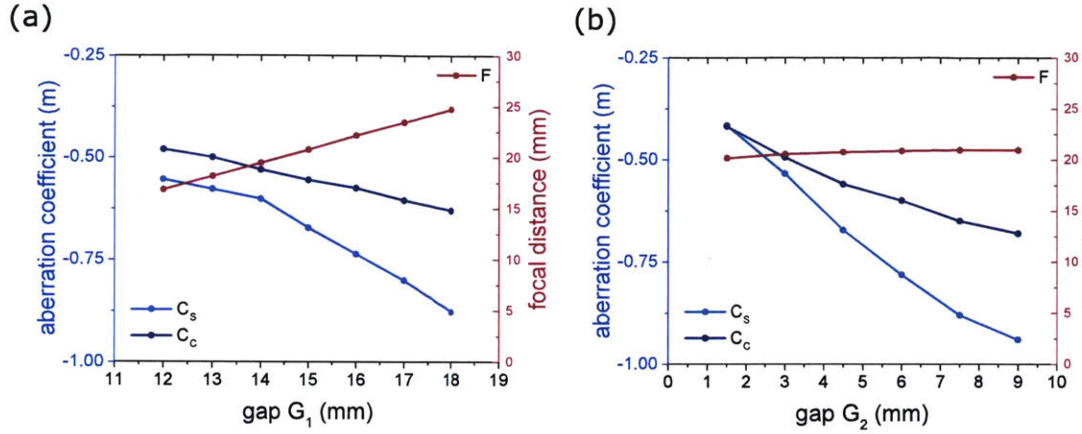

Figure 2-21: Influence of the electrode geometry on the hyperbolic gated mirror optical properties - Simulation of the varyation of the spherical and chromatic aberration coefficients and the focal length while varying G_1 (a) and G_2 (b). These simulations are performed using $V_0 = -5200$ V, $V_1 = -3000$ V and $V_2 = 0$.

some of the frequencies comprising the input pulse spectrum. For this reason, in this section, I am going to do a short overview of the two main different methods that can be used to implement the generation of electron pulses pulse. This generation has to be then synchronized with the electric pulse controlling the opening and closing mechanism of the gated mirror.

The first method that we can use to generate an electron pulse is through laser triggering. This methods works shining a fast-pulsed laser at the apex of a Schottky field emission gun. The electron pulses are then generated by photoemission. The laser is going to provide enough energy to the electron present at the tip of the gun so that they can overcome the potential set by the metal work function, and they are emitted from the tip. [44, 45, 46, 47, 48] Typically, Schottky tips are made of zirconium oxide coated tungsten whose photoemission threshold energy is ~ 2.9 eV.[48] For this reason, it is necessary to use lasers with wavelength $\lambda < 400$ nm, which permits to overcome such a barrier. We also need a pulse width < 100 ps, so as to interact as much as possible with a stable potential at the gates. Typically, laser pulses energies > 2 nJ are used to extract electrons with reasonable probability. This method schematic is summarized in Fig. 2-22 (a). Laser triggering can easily achieve fs pulses is necessary, which would not be possible with the blanking.

The second method that can be used to generate consists in having a DC electron gun instead of a pulsed one and place a fast beam blanker in the beam path. [45, 49, 50] If we place under the blanker an aperture, scanning the beam onto the aperture can generate an electron pulse as sketched in Fig. 2-22 (b). Particularly important for this method to work is the fact that the blanking has to be done at a crossover point of the beam, otherwise, during the blanking, the pivot point of the beam would move and different parts of the pulse would exhibit different optical characteristics. Nowadays, very fast blankers are commercially available. In [49] a < 100 ps electron pulse was demonstrated using a fast blanker. Other constraints to keep in mind while designing the blanking system are the fact that the blanking angle has to be larger than the convergence angle of the beam, and the fact that the aperture size has to be small enough so that the full beam can be blanked. If these constraints are not met the electron pulse cannot be generated. The deflection angle β generated by the blanker can be evaluated as follows:

$$\beta = \operatorname{atan}\left(\frac{V_p l}{2V_e d}\right), \tag{2.22}$$

where V_p is the pulse amplitude, V_e is the electrons' acceleration potential, l is the length of the parallel plates of the blanker, and d is the distance between the plates. Therefore if D is the distance from the aperture and A is the aperture size, the previously listed constraints can be written as:

$$\beta > \alpha; \tag{2.23}$$

$$A < 2D\left(\frac{V_p l}{2V_e d} - \alpha\right). \tag{2.24}$$

Future work should include the experimental comparison between these two methods in order to asses which one would guarantee the best performances.

(a) Laser Triggering

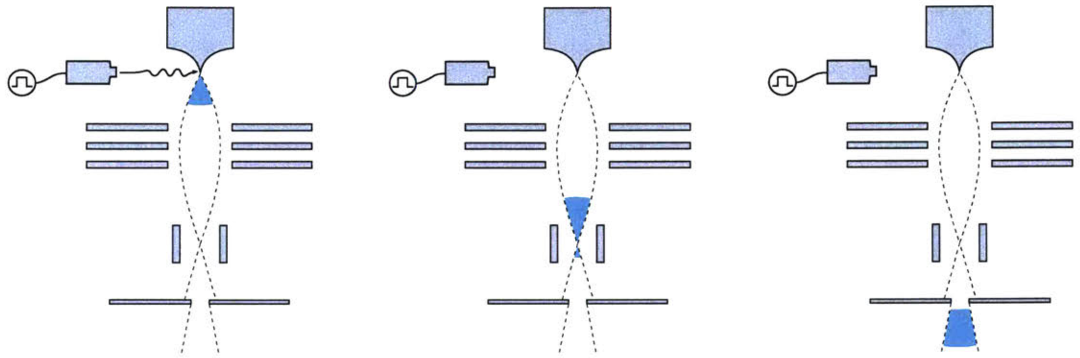

(b) Fast Blanking

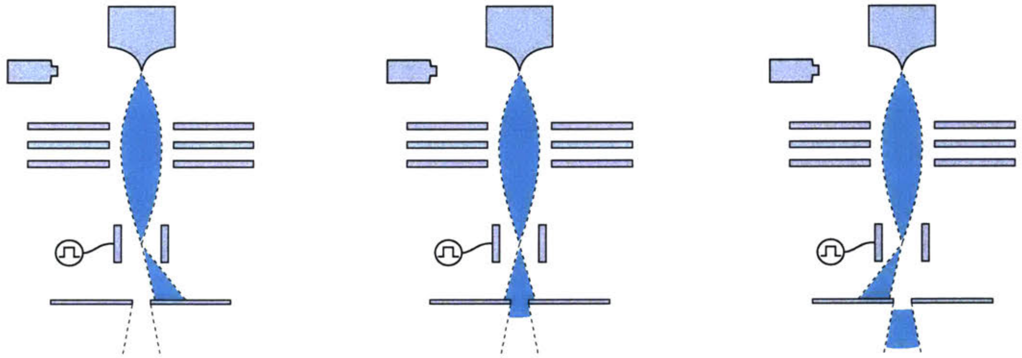

Figure 2-22: Electron pulse generation - Schematics of two possible methods to generate an electron pulse: (a) laser triggering and (b) fast blanking. Laser triggering can be achieved shining a pulsed laser on the tip of a Schottky field emission gun. The photon is going to deliver to the electrons of the tip enough energy so to overcome the work function, causing a pulsed photoemission. The fast blanking method instead can be implemented placing a blanker at a crossover point of an electron beam generated by a DC electron gun. The blanker is then used to scan the beam onto an aperture, that periodically blocks or let the beam through, therefore generating a pulsed electron beam.

Chapter 3

Design of a Linear Cavity

In this chapter, I am going to discuss the design and simulation of a linear cavity for multi-pass microscopy. The linear cavity is the main component of the microscope and it is defined by two gated mirrors, that control the resonance of the electrons in the cavity. As explained in the previous chapters, when the electron coming from the gun reach the first gated mirror they are reflected back since the potential of this component is kept high enough so as not to let the electron go through. Then, a pulse is applied to the central electrode of the top gate, which lowers its potential, letting a pulse of electrons in the cavity. At this point, both gated mirrors are kept closed and the electron bunch resonates inside the cavity gradually accumulating the phase information of the sample, which is placed at the center of the cavity. To allow this process to occur, the resonant cavity needs to satisfy several conditions:

1. the system needs to sustain the resonance of both the scattered beam and the illumination beam;
2. the image plane has to be superimposed on the sample plane after each roundtrip;
3. the resonance has to be stable, i.e. each electron trajectory needs to end up on the same spot on the sample plane with reasonable accuracy taking into account aberrations.

The last condition is particularly hard to satisfy using flat electron gates since the aberration of the system is going to disrupt the resonance stability. Essentially, the spot size on the sample is going to grow after each roundtrip. For this reason, I decided to use the hyperbolic gated mirror discussed in the previous chapter. This component would allow compensating for spherical aberration correcting for the spot size degradation at each roundtrip. However, as explained in the previous chapter, the correction requires the reflection plane to be in the Fourier plane and the image plane to be in front of the mirror. However, this condition causes a π rotation of the image therefore not allowing a sequential accumulation of the phase (the electrons would not hit the same spot after each roundtrip). To avoid this issue several strategies can be employed:

1. Using a sample that occupies only a semi-plane. This solution would entail losing half the roundtrips;
2. Using image processing to extract the image from the 2 overlapped images. This solution may not be possible since a loss of coherence in the beam can be expected if there is no coherent build up of the phase information.
3. Introducing magnetic lenses to compensate the rotation.

The most promising one seems to be the introduction of magnetic lenses in the design, which would not be a workaround but it would solve the problem altogether. For this reason, in the next section, I am going to propose and simulate a design using this solution.

3.1 Design Using Magnetic Lenses

As discussed more thoroughly in the previous chapter, while electrostatic electron lenses behave as light lenses from an optical perspective, magnetic lenses not only generate a focusing of the beam but they also introduce an image rotation. The amount of rotation can be controlled varying the current in the lens. Therefore, we can exploit this effect to our advantage to correct for the parasitic π rotation that is introduced by the employment of the gated mirror in spherical aberration correction mode.

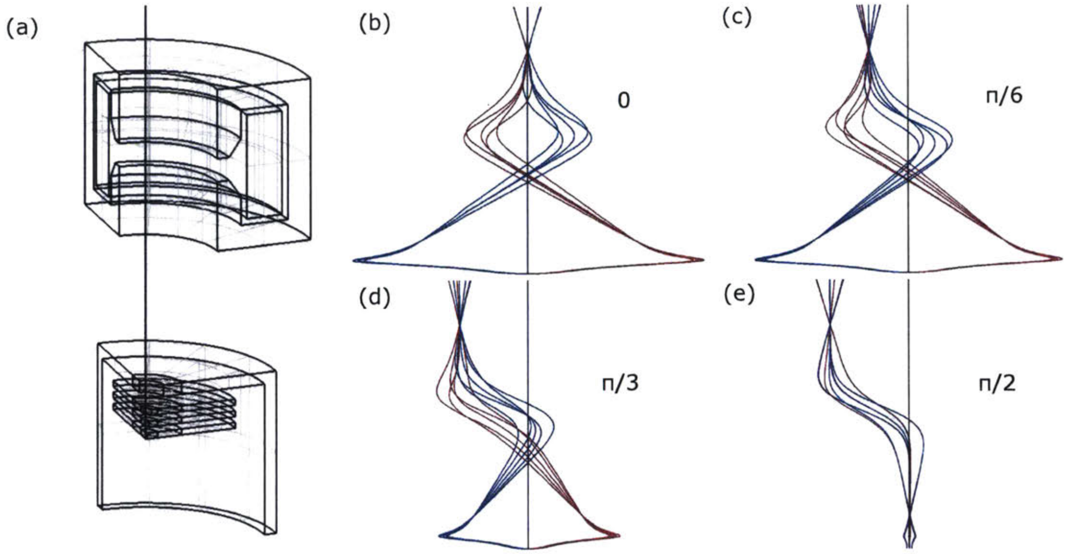

Figure 3-1: Simulation of a magnetically corrected mirror - Simulated structure, comprised of a magnetic lens and a tetrode mirror (a), and trajectory simulation shown at different rotation angles around the optical axis: 0 (b), $\pi/6$ (c), $\pi/3$ (d), $\pi/2$ (e). In the simulation the direct and reflected rays are shown in blue and red, respectively.

Fig. 3-1 shows a simulation of a structure composed by a mirror with Fourier plane on the reflection surface and a magnetic lens, whose current is selected so as to imprint a $\pi/2$ rotation. In this picture, I show the electron trajectory simulation of the rays coming from a point on the image plane. The picture shows the simulated structure and the ray tracing for different angles around the optical axis, where the direct beam is highlighted in blue and the reflected one in red. From this simulation, it can be clearly seen that each point of the image plane is re-mapped on itself after the roundtrip. This condition verifies because, going down, the beam gets a first $\pi/2$ rotation from the lens, then a π rotation from the mirror, and finally another $\pi/2$ rotation from the lens, for a total of 2π.

As shown in Fig. 1-4 the linear cavity is composed of two mirrors and 4 lenses. Therefore, instead of introducing additional elements to correct for the rotation we can substitute some of these lenses with magnetic ones. It is noteworthy that a $\pi/2$ rotation implies a focal length smaller than the lens structure itself, therefore it is not possible to use a $\pi/2$ objective lens unless we place the sample in magnetic immersion.

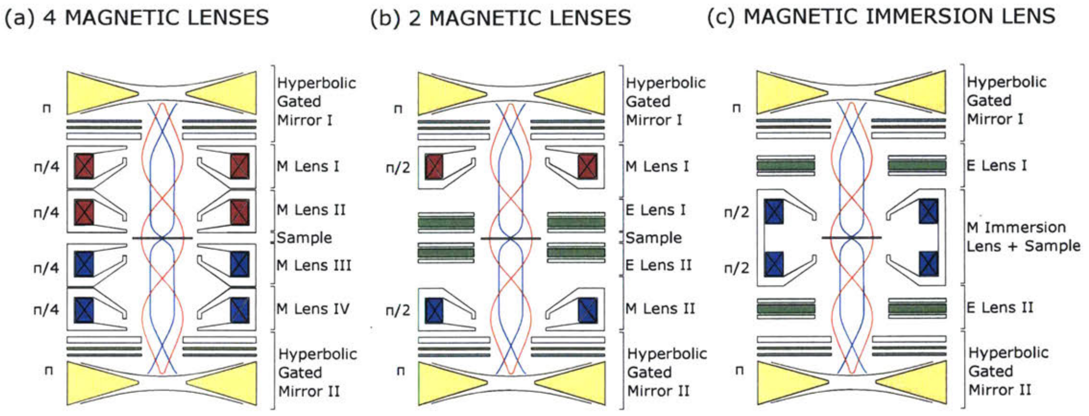

Figure 3-2: Magnetic linear cavity schematics - (a) The first design employs four magnetic lenses, each with $\pi/4$ rotation. (b) The second one employs two magnetic lenses, each with $\pi/2$ rotation. (c) The third design employs an immersion magnetic lens with total π rotation.

In Fig. 3-2, I propose three possible designs for the multi-pass exploiting this solution:

1. Employing 4 magnetic lenses with $\pi/4$ rotation. The advantage of this design is that it assures a good control of rotation and C_S correction contemporary. The disadvantage is that the objective lens focal length is not independent of the rotation. It is worth noticing the fact that if the objective lens is magnetic using opposite current for the top and the bottom lens allows to establish a zero field region at the sample position.

2. Employing 2 magnetic lenses with $\pi/2$ rotation. The advantage of this design is that it assures a good control of rotation and independent objective lens focal length (since the objective lens is electrostatic). The drawback is a more difficult implementation of C_S correction

3. Employing an immersion magnetic lens with total rotation π. The advantage of this design is that it assures a good control of C_S correction and it is a more compact design. However, the alignment can be critical.

The first option seems the most convenient. Other than the advantages previously listed, this configuration is also the more robust from a practical perspective since

Table 3.1: Resonant cavity design parameters

Element	Parameter	Value
sample	POS	0 mm
objective lens	POS	8.5 mm
	G	3 mm
	D	4 mm
	I	298 A
field lens	POS	30 mm
	G	3 mm
	D	4 mm
	I	298 A
gated mirror	POS	60 mm
	G1	15.5 mm
	G2	4 mm
	D	2 mm
	V0	-5200 V
	V1	-2628 V
	V2	0 V

you can use the field lens to compensate for a possible manufacturing-related error in the rotation imparted by the objective lens, while maintaining the correct focal distance. For this reason, I decided to base my design on this schematic.

Table 3.1 reports the position respect to the sample plane and the element parameters of the element comprising half of the linear cavity. Of course the other half is symmetric, with the exception of the magnetic lenses current that are flowing in opposite direction, so t generate a field free region at the sample position. All the positions are taken with respect to the center of the devices.

Fig. 3-3 shows the result of the simulation of a 5 keV linear resonant cavity. This simulation confirmed the stability of the electron trajectories through resonance with ray tracing of illumination and scattered beams. Fig. 3-3b,c, and d show the simulations of the marginal and paraxial ray of both the beams in the different planes. The spherical aberration spot size of the re-projected image for this design after 1 roundtrip, simulated for a scattering angle of $\alpha = 10$ mrad is $d_S = \frac{C_S \alpha^3}{2} \sim 4$ nm. Which means a spherical aberration coefficient of $C_S = 64$ mm. The diffraction spot size for these specification is $d_D = \frac{0.753}{\alpha\sqrt{V}} \sim 2$ nm. Therefore, if, as first approximation, we only consider these two contributions, we can evaluate the total spot size to be $d = \sqrt{d_S^2 + d_D^2} = 4.5$ nm. This simulation also demonstrates that with this aberration corrected design it is possible to achieve sub-angstrom trace stability. Here, trace stability is defined as the difference between the position of an illumination beam trace between two consecutive roundtrips.

Finally, the cavity has to be able to handle the in-coupling and the out-coupling of the beam. The two processes are analogous except for the fact that the first involves only the illumination beam, while the second involves both the illumination and the scattered beam. Fig. 3-3 shows the operation of the cavity during resonance and out-coupling. This simulation is done performing a ray-tracing in the two configurations, therefore demonstrating the effectiveness of this design in performing also the task at hand.

All these results and validations suggest that our design is suitable for a proof of concept demonstration of a multi-pass electron microscope.

3.2 Possible Developments

The proof-of-concept demonstration of the multi-pass principle is just the first step in building a multi-pass microscope able to compete with traditional TEMs. In order to be able to achieve a sufficient resolution, necessary to resolve sub-nanometer details of a protein this design requires improvements. In this section, I am going to discuss some possible developments of this design that in the future could be implemented to make it more effective.

3.2.1 Acceleration Stage

One necessary step to improve this design is the increasing of the operating voltage. In this design, we are passing through the sample with 5 keV energy electrons. However, it would be more convenient to use high energy electrons which interact very little with the sample. For this reason, together with the fact that high energy lenses have

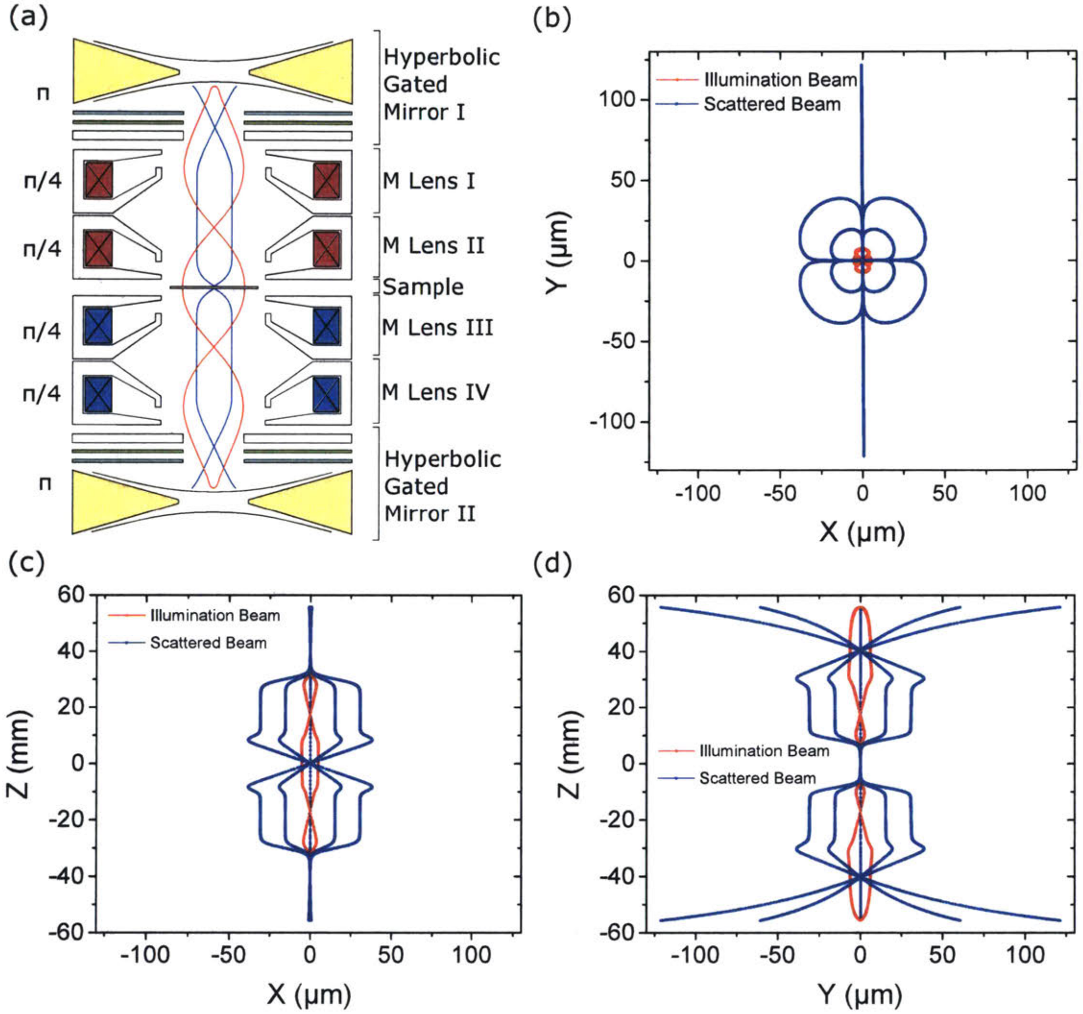

Figure 3-3: Magnetic linear cavity simulation - (a) Schematics of the resonant cavity, composed of 4 magnetic lenses and two hyperbolic gated mirrors. The hyperbolic gated mirrors are composed of 4 electrodes and can compensate for spherical and chromatic aberrations. Each magnetic lens provides the correct focusing power as well as a $\pi/4$ rotation that compensates for the π rotation of the mirror, so that the sample can be re-imaged on itself correctly and the phase information can be accumulated during the resonance. The lenses on the lower half of the linear cavity have the opposite direction of the current so that the sample is kept in a field-free region. (b-d) Ray tracing simulation of the illumination beam and scattered beam in XY (b), XZ (c) and YZ (d) planes. This simulation is performed using a 5 mrad scattering angle and 5 keV electron energy. The result shows sub-angstrom trace stability and a spot size of the re-projected image of 4 nm, which is close to the diffraction limit for this electron energy (1 nm).

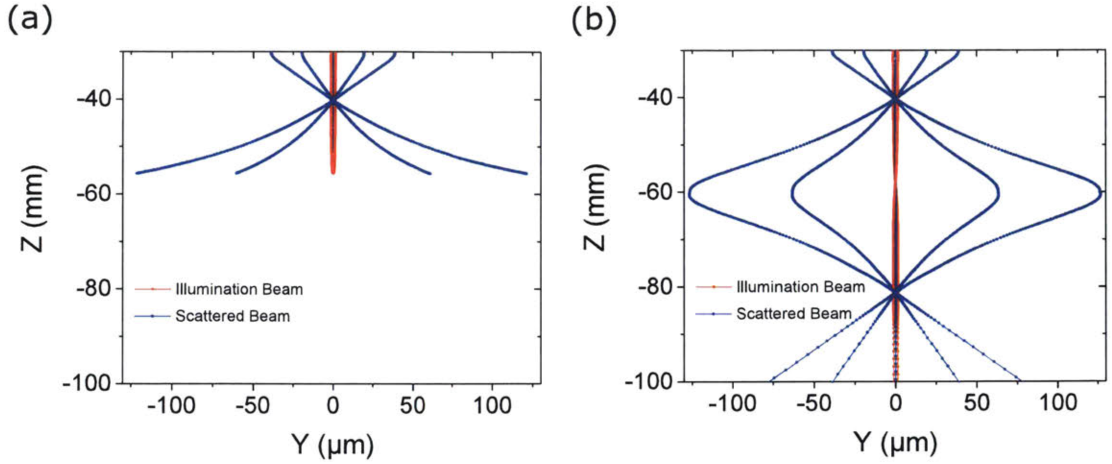

Figure 3-4: Out-coupling simulation - Ray-tracing simulation of the illumination and scattered beams at the second gated mirror during resonance (a) and out-coupling (b). This simulation shows that the beam optical characteristics are not significantly affected during the out-coupling process, therefore validating the design during this mode of operation.

a lower aberration, typical TEMs are operated at 200-300 keV. Another issue with low energy electrons is that they experience a larger phase shift when interacting with a sample. This phase shift limits the maximum number of roundtrips that can be implemented because after the phase shift reaches 2π there will be phase wrapping, and no additional information can be collected. On the other hand, high energy electrons experience less phase shift when passing through the sample, therefore we could potentially increase the number of roundtrips and decrease the dose without risking phase wrapping.

However, building gated mirrors at such a high voltage would be very challenging from an engineering perspective. For this reason, a possible solution would be the introduction of an acceleration/deceleration stage at the center of the cavity, where the sample is placed. In this configuration, the electrons can be reflected by 5 keV mirrors but then they are accelerated to a much higher energy before interacting with the sample and then decelerated before entering in the other arm of the cavity. Of course, in this case, the sample would have to be floating at a high potential, which is challenging from an engineering point of view, but feasible.

In this section, I am going to discuss some preliminary results regarding the study

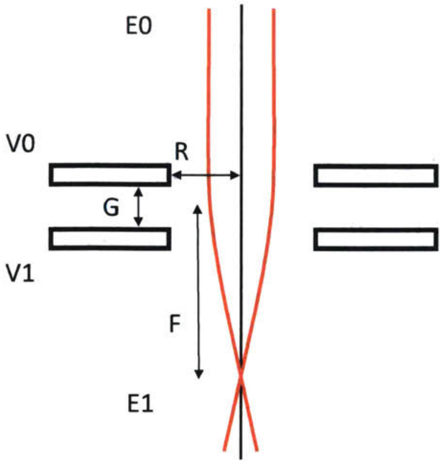

Figure 3-5: Acceleration/deceleration lens simulation scheme - Sketch of the model used in the simulation. The electrodes used are 1 mm thick. In the Acceleration (Deceleration) case E0 (E1) is 5 keV.

of the aberrations introduced by this acceleration/deceleration stage. Other then the practical challenges in assembling such a device, a possible additional obstacle to the implementation of such a system can come from the aberration that it would introduce. These are going to degrade the resolution and if too large they could potentially overcome the advantages introduced by the acceleration/deceleration stage. Therefore, an aberration analysis of such a system is necessary. To do so I proceeded first by simulating the acceleration and deceleration stages separately. I performed a ray tracing simulation of these systems in order to characterize their aberration and lensing effect, for different geometries.

Fig. 3-5 shows a sketch of the model used in this simulation. This model is comprised of two rotationally symmetric electrodes, kept at different potentials. The acceleration/deceleration is determined by the difference between these electrode potentials. I adopted a uniform 1 mm thickness for the electrodes and varied the other geometrical parameters, i.e. gap and electrode radius, that have the most significant impact on aberrations.

Fig. 3-6 and Fig. 3-7 portray the result of the simulation of the acceleration and deceleration stages, respectively, while varying the acceleration and deceleration voltage. The electrons' energy outside the stage used in this simulation is 5 keV, which is consistent with the cavity designed in the previous section. The electrons are accelerated of 30 keV, 60 keV and 90 keV in the sample region. For each of these energies, I performed a ray tracing simulation varying the gap and the electrode radii and evaluated the values of the spherical aberration coefficient and focusing power. These parameters are fundamental for the design of the cavity because they are going to determine the aberration correction that we need to apply and the minimum spot size that we can re-image onto the sample. As can be seen from these simulations an increase of the gap always corresponds to an increase of C_S and a decrease of the focusing power. Increasing the electrode bore instead decreases C_S in the acceleration case and increases it in the deceleration case while the focusing power is reduced in both. it is noteworthy that these properties have an opposite effect on the minimum achievable spot size since $d_S = \frac{C_S\alpha^3}{2}$ and for the same incoming beam, higher focal distance F (i.e. smaller α) implies smaller spot size while higher C_S increase it.

Once established these factors, I integrated both the components into a single acceleration/deceleration stage. Fig. 3-8 shows the electric potential simulation of a 50 kV acceleration/deceleration stage. The sample holder is placed in the middle, and it has to be conductive. The whole system is electrically floating and the mechanical connection to the external chassis has to be done with an insulating material.

3-9 portrays the potential close the sample plane. As can be seen, the sample sits in a region of very uniform potential. Therefore, the electric field is going to be negligible and we do not expect any parasitic disturbance.

3-10 portrays the ray tracing simulation of a beam entering the acceleration/deceleration stage with an energy of 5 keV and an angle of 5 mrad. This condition corresponds to a sample illumination area of 6 µm. The resulting spot size after passing through the whole system is $d_s = 3$ nm which is reasonable and corresponds to an overall C_s of the stage of 48 mm.

3.2.2 Design with Blanking In- and Out-coupling Mechanism

The integration of the controlled reflection, the aberration correction and the fast switching are not an easy requirement to be met in a single component. There-

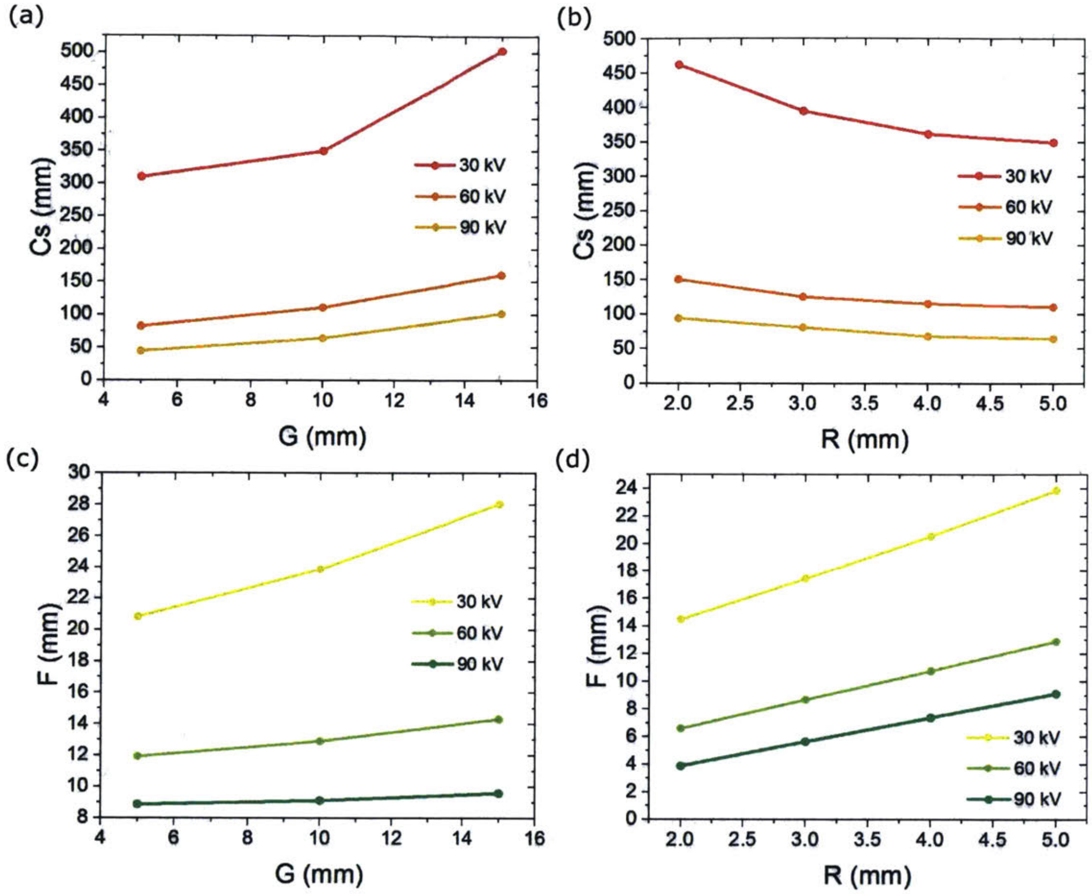

Figure 3-6: Acceleration stage simulation - Simulation of the spherical aberration coefficient (a) and focal distance (c) while varying the lens gap for a radius $R = 5$ mm. Simulation of the spherical aberration coefficient (a) and focal distance (c) while varying the lens radius for a gap $G = 10$ mm

fore, it would be beneficial to have an alternative design that would not require to have a gated mirror to in-couple and out-couple the electron beam. A possible alternative would be to entrust the switching mechanism to a fast blanker. This idea was initially proposed by Prof. Pieter Kruit, who adopted this concept to design a mirror-based aberration corrector that does not require a magnetic separator, called K-corrector.[51] With the relaxation of this constraints, the design of an aberration-corrected mirror become easier, and the aberration correction can be tuned more straightforwardly. Fig. 3-11 (a) shows the schematics of this possible design. At the start, the first blanker is on while the second is off. The electron beam is coming from

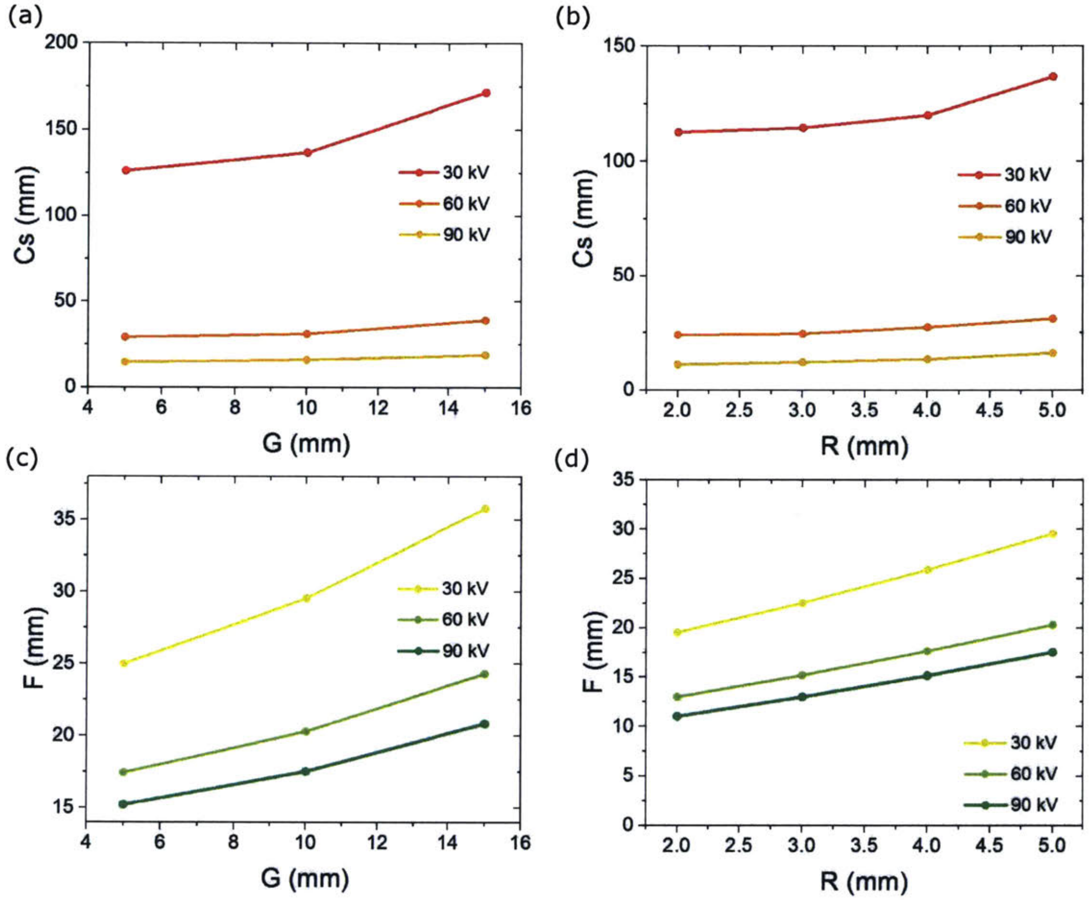

Figure 3-7: Deceleration stage simulation - Simulation of the spherical aberration coefficient (a) and focal distance (c) while varying the lens gap for a radius $R = 5$ mm. Simulation of the spherical aberration coefficient (a) and focal distance (c) while varying the lens radius for a gap $G = 10$ mm

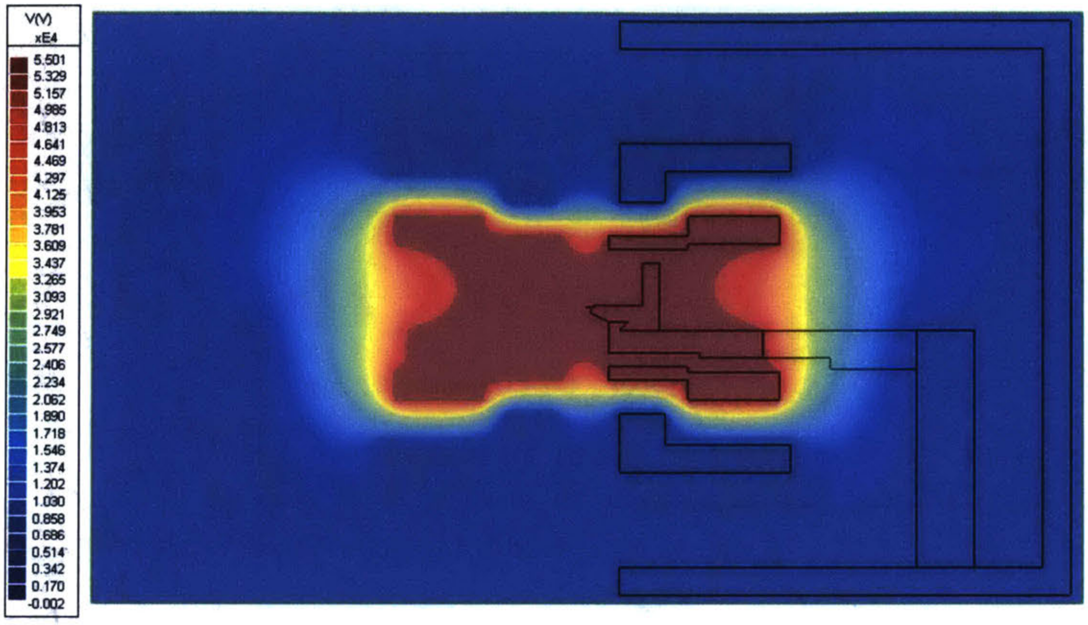

Figure 3-8: Acceleration/deceleration stage potential distribution - Electrical potential simulation of the acceleration/deceleration stage, insulated from the external grounded chassis.

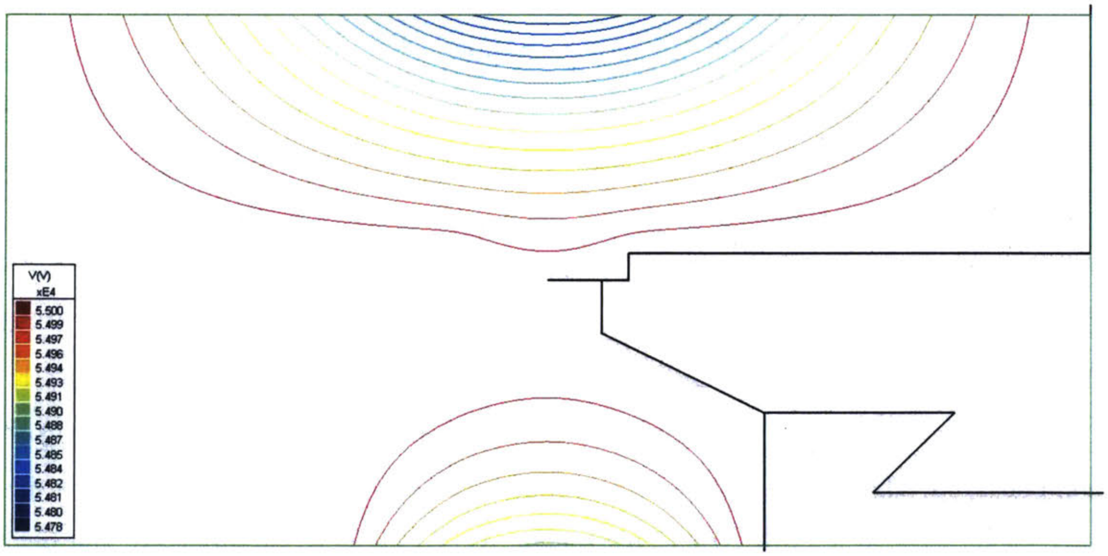

Figure 3-9: Potential distribution at the sample - Simulation of the equipotential surfaces close to the sample plane. The sample is in a position of very uniform potential, hence the field is going to be negligible. Therefore, it is not going to cause any parasitic effect during measurement, such as charging due to difference in potential between different sample regions.

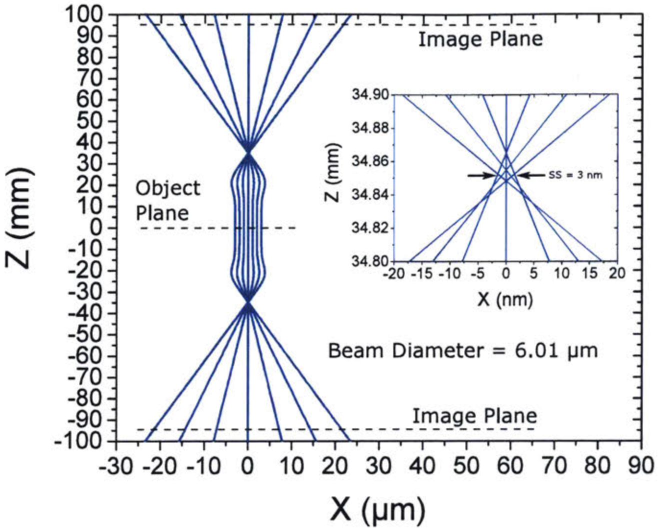

Figure 3-10: Acceleration/deceleration stage particle trajectory simulation - Particle trajectory simulation of a 5 keV electron passing through a 50 keV acceleration/deceleration stage. The inner plot is a close up of the beam at the focal position, showing a spot size due to spherical aberration of 3 nm

the gun and is deflected by the blanker into the cavity, which remains analogous to the one described at the beginning of this chapter. Then the first blanker is switched off and the electron packet is allowed to resonate inside the cavity. After a sufficient number of round trips, when the beam picked up enough phase information from the sample, the second blanker is switched on, the electrons are out-coupled and they can be detected by a screen. It is noteworthy that the blankers do not have to be operated fast, they just need to have a fast rising time. The main drawback with this design is that the deflection angle has to be fairly large to be able to be in-coupled in the cavity and this condition is going to introduce strong aberration, which has to be compensated. One possible way to do it would be to use four blankers instead of just two, as shown in Fig. 3-11 (b). This scheme would allow to pre-aberrate the beam with the first blanker and then, if the second one is positioned at a right distance, and a beam crossover is present in-between the two deflectors, the first blanker aberrations could be compensated. Future work should include a feasibility study for this alternative design.

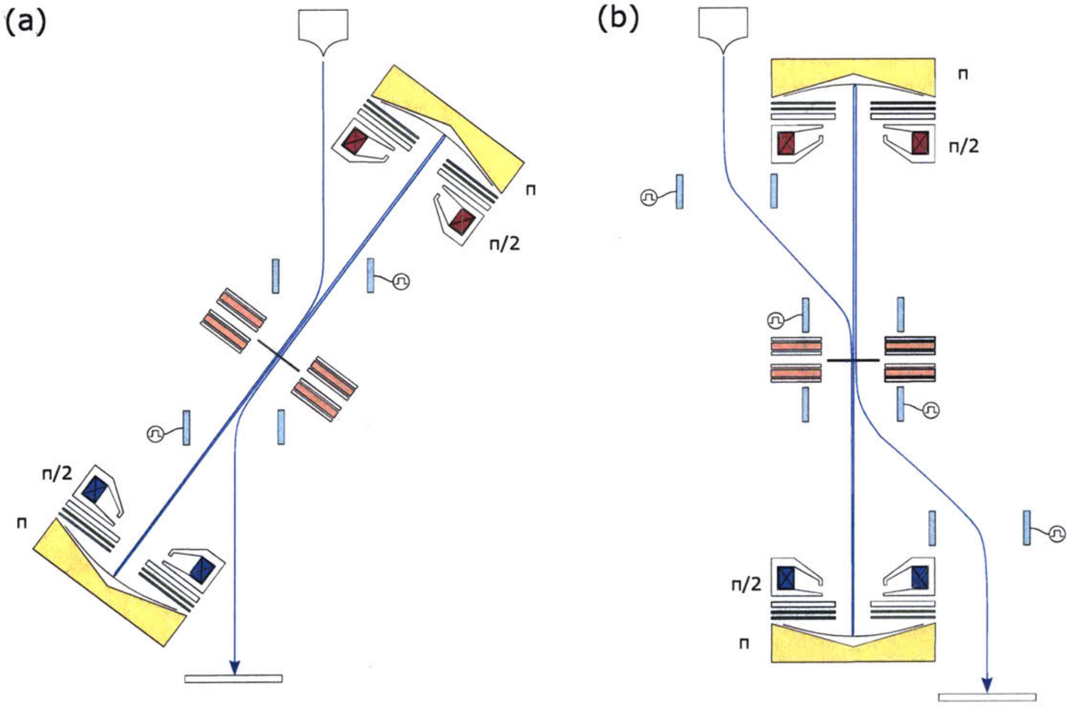

Figure 3-11: Schematics of an alternative design with blanking in- and out-coupling mechanism - This design employs fast blankers for the beam coupling in and out from the cavity. This design relaxes the constraints on the gated mirrors. It is possible to adopt either 2 (a) or 4 blankers (b). The latter options would allow to compensate the astigmatism due to the blankers.

Chapter 4

Development of the Diagnostic Setup

In this chapter, I am going to report on my work toward the development of a diagnostic setup for the measurement of beam current, energy spread, and aberration, to be used for the characterization of electron optical components for multi-pass microscopy.

The development of an experimental apparatus able to demonstrate the validity of the multi-pass measurement approach requires the development and testing of a novel component, e.g. the gated mirrors, both isolated and integrated with the other electron-optical elements comprising the cavity. Therefore, to characterize these components, we need to develop a diagnostic setup and a diagnostic procedure. This testbed system should be comprised of a laser triggered source which allows time-resolved measurements, a holder compatible with different electron optical elements, a nano stage that allows placing a sample at different positions of the electron beam and a heavy-duty stage that allows out-coupling of the signal. As the multi-pass is comprised of components that have to work both in reflection and transmission it would be beneficial to characterize them in both ways. In this chapter, I am going to concentrate on the diagnostics for transmission.

The final goal is to characterize these components with time and spatial resolution, characterizing the energy spread they generate, how much current they let pass through when the gating is activated and the aberrations that they produce. Fig. 4-1 illustrates two possible measurement schemes that we want to implement in such a system. Since we lack of a pulsed electron source these beam characterization techniques were developed for DC, which is what is going to be described in this chapter. In the future, the plan is to substitute our the source with a laser triggered source, and then translate these technique in time domain synchronizing the signal out-coupling with a known delay from the electron beam triggering. The first measurement employs placing a Faraday cup in the beam path. This element is composed of a metallic cup with a high aspect ratio which collects the beam electrons and if connected to an ammeter allows us to measure the beam current. A negatively biased electrode can be placed on top of the cup, so that the secondary electrons generated by the interaction between the beam and the cup are not allowed to leave the cup, allowing for a more precise measurement. In order to characterize the aberrations instead, we need to image the beam itself. For this reason, we need a phosphorus screen in the beam path and an optical out-coupling system.

Fig. 4-2 illustrates the system that was used for the characterization of the beam. The assembly of such a setup was done modifying an existing Zeiss LEO 1525 SEM, which employs a Gemini column. The system is comprised of the column, the vacuum chamber, and a slide-in custom door, that we can remove, modify for our experiment and then re-insert. The door hosts a heavy-duty stage, which allows us to load the electron-optical elements. This stage is also hollow so that it allows us to out-couple the optical signal. For our experiments, we can place the Faraday cup or the phosphorus screen (with or without micro-channel plates) on an interface plate designed to sit on the heavy-duty stage. Then an out-coupling optical system was also designed. Such a system is allocated into the stage and brings the signal outside the chamber. Outside the chamber, the signal is recorded onto a CCD camera (Grasshopper 3 GS3-U3-28S5M, with 8.8x6.6 mm sensor) connected to the door. On the interface plate that hosts the phosphorus screen it is also possible to connect a SMARACT 3-axis nano-stage, that allows us to place and finely manipulate a sample in the electron beam path. Fig. 4-3 shows a picture of the same diagnostic setup.

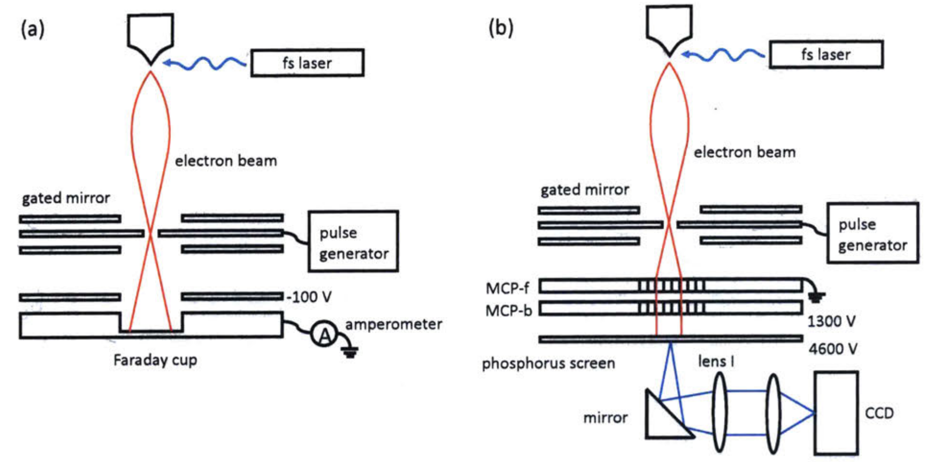

gated mirror current characterization

gated mirror beam aberration analysis

Figure 4-1: Schematics of possible characterization techniques in transmission - Illustration of two possible measurement setups to characterize a gated mirror in terms of its current (a) and aberrations (b). The first measurement can be performed placing a Faraday cup in the beam path, below the device under test (DUT) and readout the current with an ammeter. The aberration measurement instead, requires to place an imaging system in the beam path. This task can be fulfilled placing a phosphorus screen under the DUT and an optical out-coupling system.

4.1 Energy Spectroscopy

The first important parameter that we want to know for our beam characterization is the beam energy spread. In fact, this parameter will greatly affect the performances of the microscope because electron optical component is going to suffer chromatic aberrations, and the spot size due to chromatic aberration can be expressed as $d_C = C_C \alpha \frac{\Delta E}{E}$, which means that a smaller energy spread ΔE is, of course, going to minimize the effect of this aberration.

In order to test the energy spread of the beam in our diagnostic testbed, a setup for retarding potential analysis (RPA) was assembled. This measurement was performed placing a grid between two ground plates in the beam path and sweeping its potential as shown in Fig. 4-4 (a). While sweeping the potential close to the electron beam acceleration potential, in between the grid mesh the potential surfaces are going to gradually reflect all the electron with energy not sufficient to pass through the highest closed potential surface as summarized in Fig. 4-4 (b). Then, the transmitted

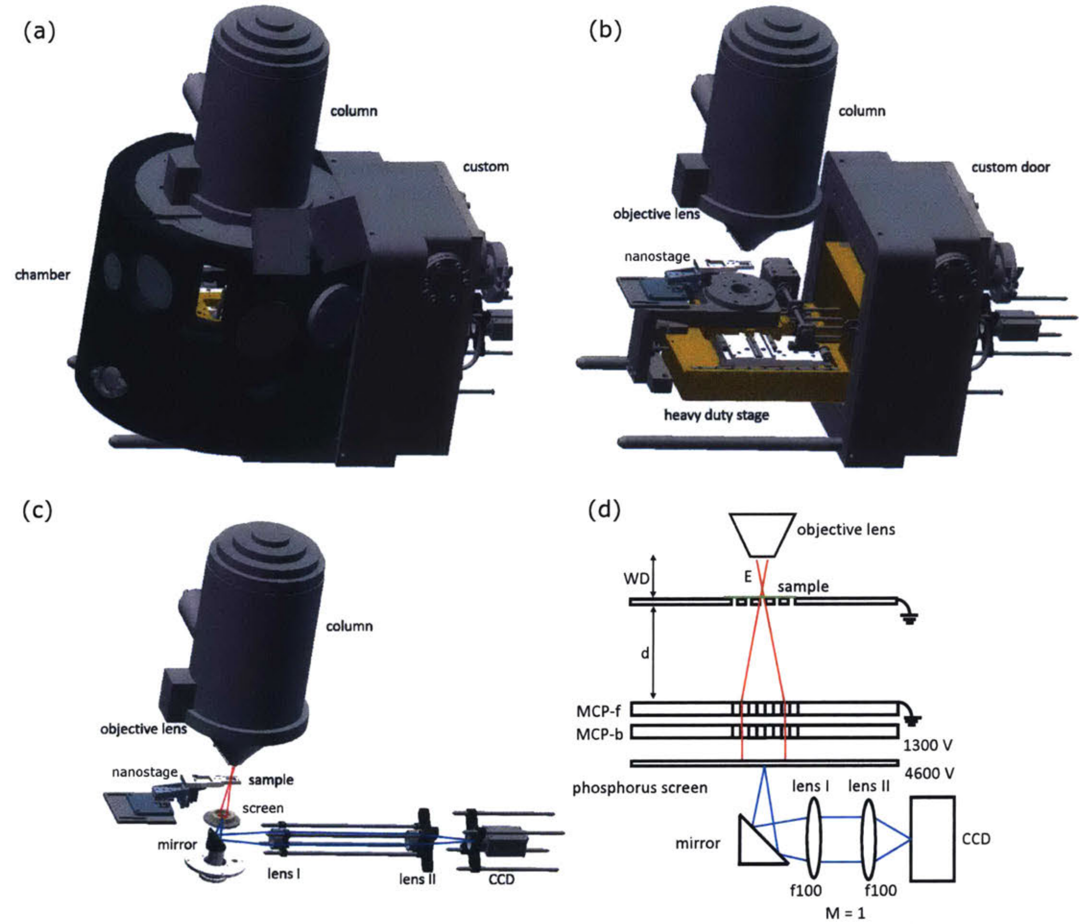

Figure 4-2: CAD of the measurement setup - Different layers of the 3D rendering of the diagnostic setup used to characterize the beam (a-c) and schematics of the same setup (d). The system is built modifying an existing Zeiss SEM equipped with a Gemini column. The original door was substituted with a removable custom door, which allow us to easily modify the experimental setup each time. The door is connected to an heavy duty stage where we can load the electron optical elements and a nanostage to manipulate a sample. An optical system was also installed, connected to the door. This optical system is used to out-couple the signal coming from a phosphorus screen placed in the beam path.

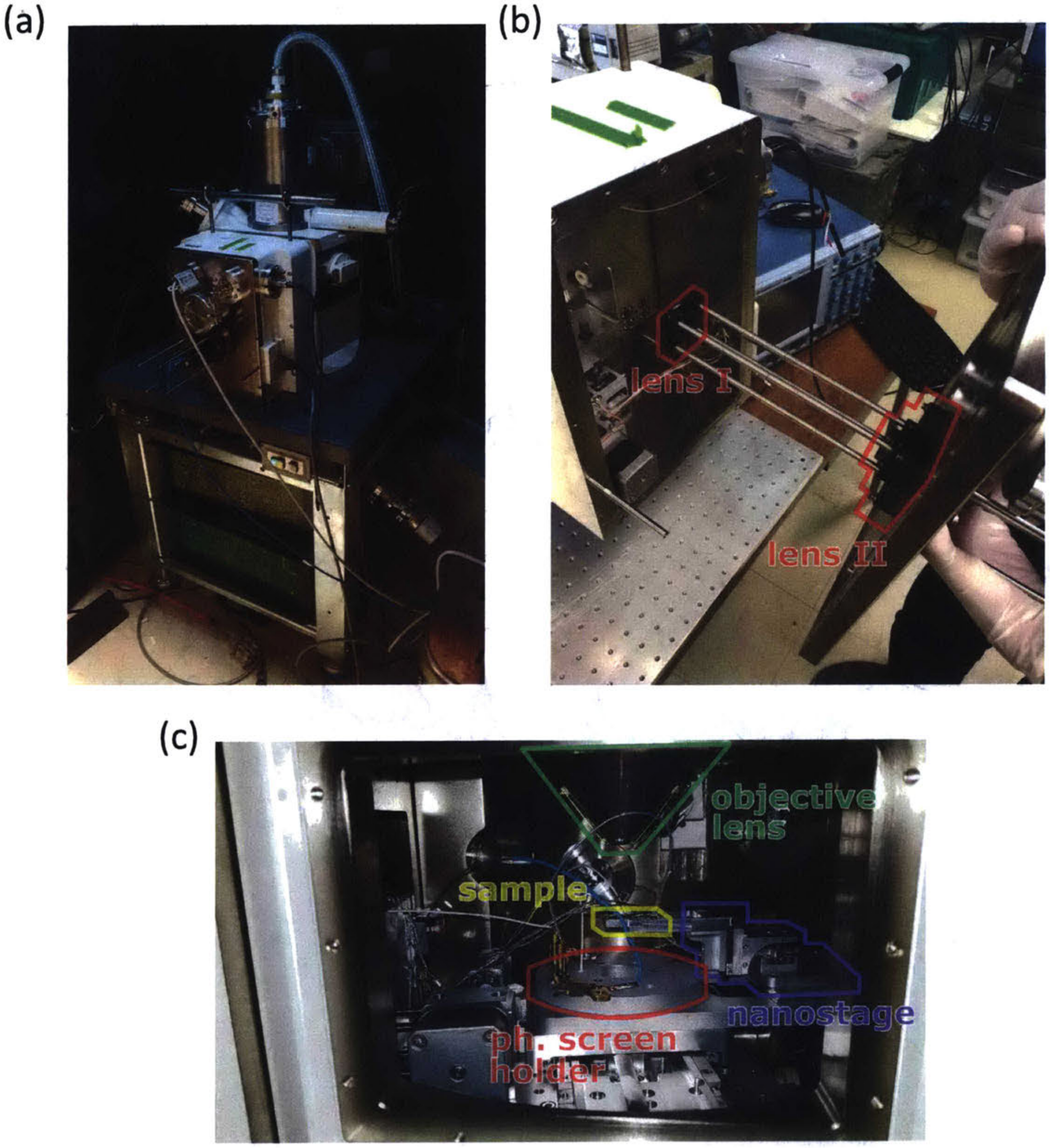

Figure 4-3: Experimental setup - Pictures of tool modified to host the diagnostics setup (a) and close-up on the assembly of the optical apparatus (b) and the characterization setup inside the chamber (c). In the latter it is possible to see the objective lens, the nanostage used to mount the samples and the top plate on which is mounted the phosphorus screen.

current was measured with a Faraday cup connected to an ammeter, in order to get a spectroscopic measurement of the electron energy. Fig. 4-4 (c) shows what the current data looks like for one of these measures. In this case, the measurement was performed for a 5 keV electron beam. It can clearly be seen that at the beginning, when all the electron are allowed to pass through, the measured current was 320 pA. Then, the current gradually goes to zero when the potential is swept. If we assume a Gaussian distribution of the electron beam energy, then this measurement should look like its integral. Therefore, we can fit the data with an ERF function:

$$f(x) = y_0 + A \cdot \mathrm{erf}[k \cdot (x - x_0)] = y_0 + \frac{2A}{\sqrt{\pi}} \int_0^{k\cdot(x-x_0)} e^{u^2} du. \tag{4.1}$$

Once we fit our curve with this equation we can extract the correspondent Gaussian curve, which is plotted in Fig. 4-4 (d). In particular, we can extract the energy spread, which is:

$$\Delta E = 2\sigma_E = \frac{2}{k\sqrt{2}}. \tag{4.2}$$

In this case the energy spread is $\Delta E = 1.72$ eV.

An important point to notice is that this measurement provides an overestimation of the beam spread. In fact, we have to take into account a parasitic effect which is the fact that the electron spot size is finite. Therefore, since some electrons are going to be focused farther or closer, they can be reflected back also from some not fully closed potential surfaces. Therefore, since we know that the spot size is directly proportional to the convergence angle, in order to get a better estimation of energy spread, we can repeat the same test with a smaller aperture (i.e. smaller convergence angle). We noticed that the value of the energy spread stabilizes for an aperture lower than 20 µm. Hence, we decided to use this angle for our characterization. It would be also possible to use an even smaller aperture. However, since a smaller aperture also implies a smaller current, you require a much more precise ammeter to get a clean measurement. For this reason, we decided to stick with the 20 µm. 4-5 shows a comparison between the result obtained for the energy spread using 60 µm

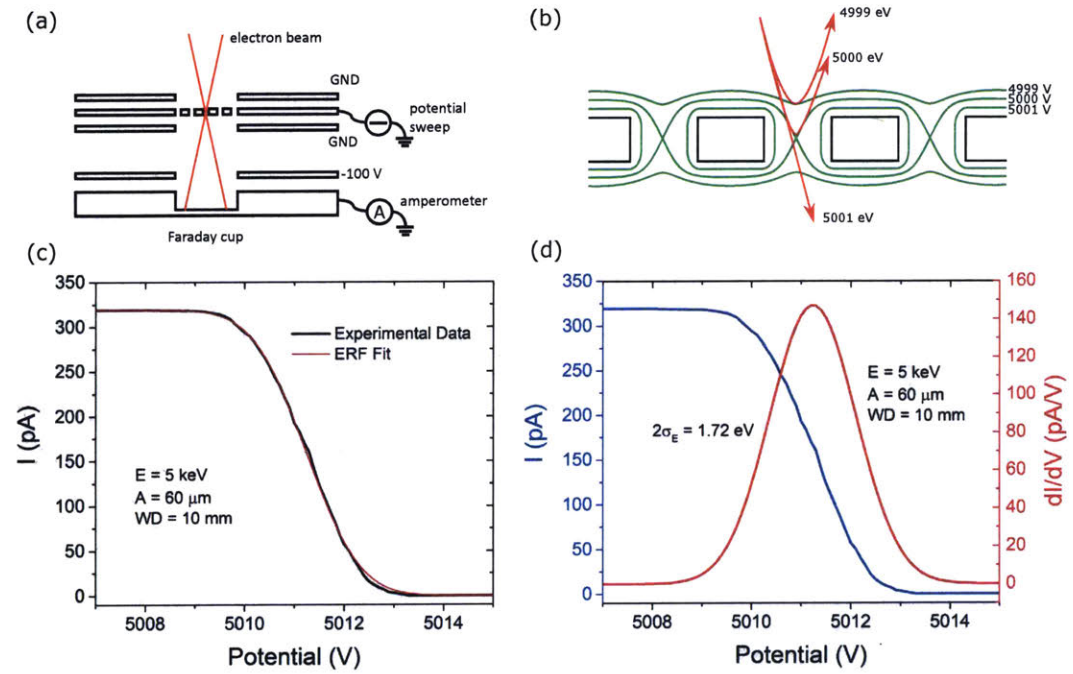

Figure 4-4: Energy spread analysis - (a) Schematic of the system used to characterize the energy spread; (b) retarding potential analysis principle; (c) experimental data and erf fitting of the retarding potential analysis; (d) Gaussian curve evaluated from the derivative of the fit, showing an energy spread of $\Delta E = 2\sigma = 1.72$ eV. Since the spot size is finite this measurement provides an overestimation of the beam spread. To improve the estimation we are going to decrease the aperture size until we see a stabilization of the value of the measured energy spread to its minimum.

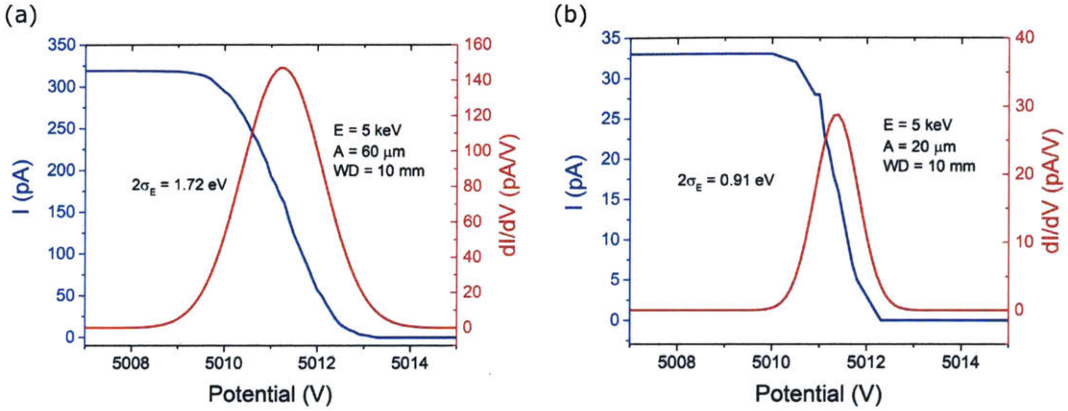

Figure 4-5: Aperture dependence of the RPA - Comparison between the result obtained for the energy spread using 60 µm (a) and 20 µm (b) apertures.

(a) and 20 µm (b) apertures. The energy spread obtained with the 20 µm aperture is $\Delta E = 0.91$ eV.

The measurement was repeated for different values of nominal beam energy, and as we can see in Table 4.1, the resulting energy spread is stable, which is another indication of the fact that this measurement scheme is a reliable tool to asses the beam energy spread.

Table 4.1: Energy spread dependence with energy (A $= 20\mu m$)

E (keV)	ΔE (eV)
2	0.83
3	0.89
5	0.91

This measurement is going to be used in the future not only to asses the quality of the source, but also to characterize the quality of the components. In fact, if when the gate is operated, the electron pulse does not pass through the gated mirror when the potential gating pulse is stable, the electrons are going to interact with a time-varying potential which could affect the beam quality, i.e. its energy spread. This kind of measurement is going to be used to identify the safe time window of operation and the electron generation is going to be timed accordingly.

4.2 Aberration Characterization

In this section, I am going to report on the second important method implemented in order to characterize the beam aberrations. In particular, we are going to concentrate on the development of alternative methods for the evaluation of the spherical aberration coefficient C_S of the beam. These methods require us to image the transmitted beam through a sample. Therefore, we are going to make use of the out-coupling and imaging system described in the introductory section of this chapter and illustrated in Fig. 4-2. In the following two different approaches to retrieve the spherical aberration coefficient are described.

4.2.1 Ronchigrams

The first method that was implemented employs the insertion of a thin sample in the beam path, at the focal position, and the acquisition of a shadow image of the corresponding Ronchigram[22, 23, 24] on a phosphorus screen. This methodology was developed for TEM but with our shadow imaging diagnostic setup, it is possible to use it also in an SEM.

Fig. 4-6 illustrates the working principle of the method. When the electron beam is affected by spherical aberrations the inner rays are focused farther away. As a result, if the beam is focused on the sample, on your image plane you will have regions of different magnification. In particular, there will be a ring where the magnification is infinite. From the size of this ring, knowing your defocus it is possible to infer the spherical aberration coefficient C_S. The evaluation of C_S can be done by noticing that if we defocus the beam respect to the Gaussian focusing condition of a certain amount R_0, the radius of the disc of infinite magnification on the Gaussian focusing plane is going to be $R_0\alpha_\infty$, where $\alpha_\infty = \frac{R_\infty}{D}$ is the semiangle of the circle of infinite magnification R_∞. Since $C_S\alpha^3 = R_0\alpha$ from the definition of C_S [22], then $C_S\alpha_\infty^3 = R_0\alpha_\infty$, and:

$$C_S = \frac{R_0}{\alpha_\infty^2} = \frac{R_0 D^2}{R_\infty^2}. \tag{4.3}$$

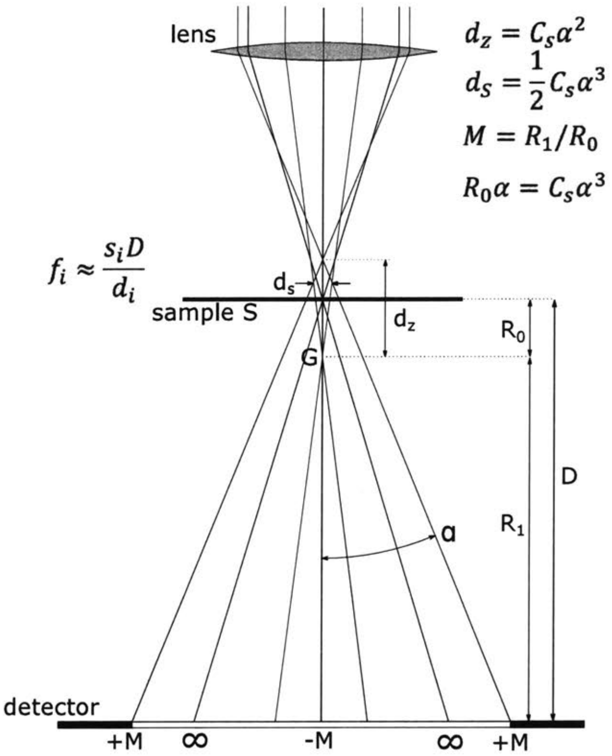

Figure 4-6: Ronchigrams - Schematics of the method used to asses the spherical aberration coefficient C_S collecting Ronchigrams in shadow imaging. Spherical aberrations entails that the paraxial rays are focused farther away respect to the marginal rays. Therefore, if you focus the beam onto the sample, on your image plane regions of different magnification are going to appear. At one specific distance from the optical axis, there will be a ring where the magnification is infinite, because the rays correspondent to this radius are the one exactly focused on the object plane. From the size of this ring, knowing your defocus you can infer the spherical aberration coefficient C_S using the relations reported in the figure.

In order to implement this method, we need to acquire images using the imaging system described in Fig. 4-2. Fig. 4-7 shows the comparison between the same spot imaged by the secondary in-lens detector of the SEM and our shadow imaging system, using optical magnification $M = 1$, that is obtained placing two F100 lenses, one at 100 mm from the phosphorus screen and the other at 100 mm from the camera. The first image is of course acquired by scanning onto the sample, while the second one is recorded in spot mode, which means with a stationary beam onto the sample. We can appreciate that the two measurement schemes give comparable results in

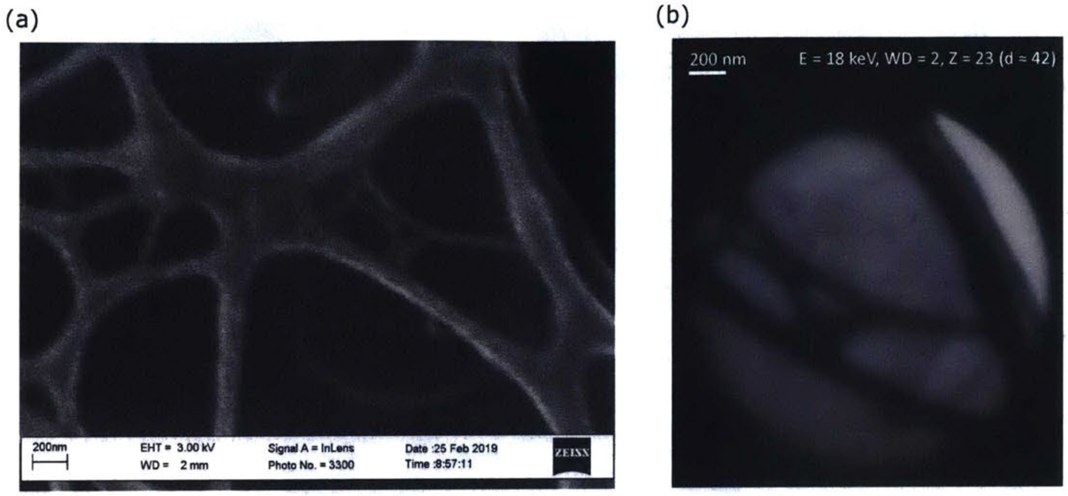

Figure 4-7: Comparison between in-lens SE2 and CCD - Picture of the same region of a single layer graphene on lacey carbon sample, acquiring the data with the in-lens secondary electron detector of the SEM (a) and from the CCD recording the shadow image on the phosphorus (b). The first one is acquired in scanning while the second one is done in spot mode, with the beam few microns above the sample.

terms of resolution. We can clearly distinguish features smaller than 100 nm in both images. The sample imaged in this experiment is single-layer graphene on holey carbon. This sample was selected because a very thin sample is necessary since we are working in transmission, in order to obtain an intense enough signal to excite the phosphorus screen with energy lower than 20 keV, which is the maximum limit of our SEM. TEMs can deal with samples of higher thicknesses, but they are operated at hundreds of keV. One problem that we encountered with this kind of sample is the carbon deposition when we have the beam focused close to the sample plane, which is the condition where we want to be to acquire a Ronchigram. The presence of this deposition is a problem because it means that we get time-dependent images which make the evaluation of the spherical aberration coefficient more complex.

However, this problem can be solved if, instead of focusing on the graphene, we focus the 20 keV beam onto an edge. In this case, as we can see in Fig. 4-8, the paraxial rays, which are focused after the sample, due to the spherical aberration are going to generate a flipped image. Instead, the rays that are above the sample are going to preserve the image orientation. Thanks to this effect we can easily estimate

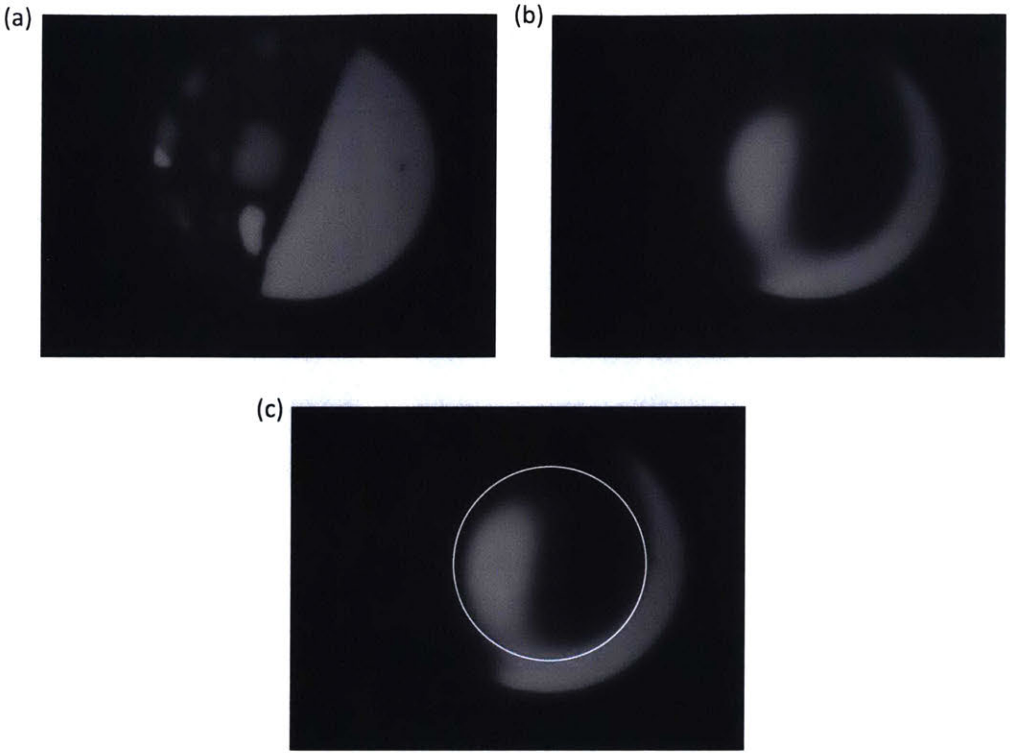

Figure 4-8: Edge Ronchigram - Images obtained placing the beam optical axis onto an edge between lacey carbon and vacuum of the sample. (a) is recorded with the beam focused few tens of microns above the sample, (b) is obtained with the beam focused onto the sample. The central part of this second image is mirrored with respect to the external part since the paraxial rays are focused below the sample plane while the marginal rays are focused above the sample plane. (c) is the same as (b) but with the circle of infinite magnification highlighted. The beam parameters are: energy E = 20 keV, working distance WD = 1 mm, and aperture A = 120 µm.

the size of the circle of infinite magnification, as shown in Fig. 4-8 (c). Also this method has its drawback. Since this method requires the acquisition of a series of images as will be explained later, and the beam is on an edge, a nanometric drift of the sample is going to generate a loss of the image. Therefore, a fast image sequence acquisition is necessary in order to use this method.

In order to both mitigate the carbon deposition problem and avoid issues due to the sample drifting, a different sample can be used. The method was successfully implemented using Si_3N_4 5 nm membranes, which are commonly used as a support

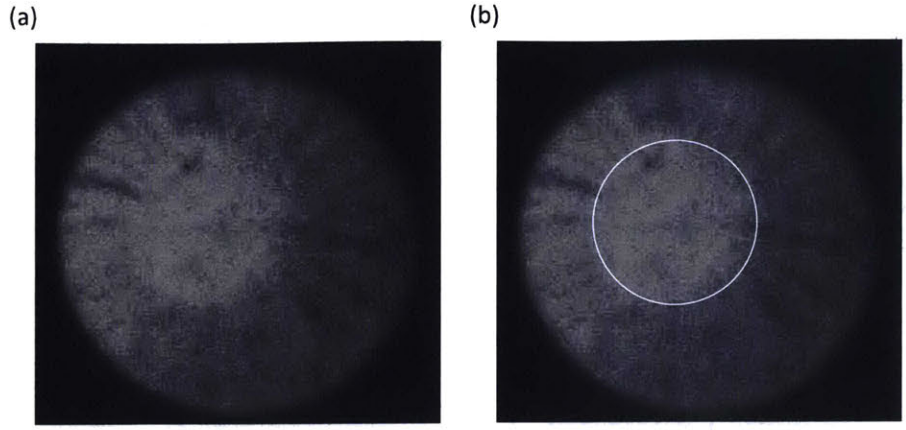

Figure 4-9: Ronchigram of a Si_3N_4 membrane - Images obtained placing the beam optical axis onto a Si_3N_4 5 nm membrane. (a) is obtained with the beam focused onto the sample. In (b) the circle of infinite magnification is highlighted. The beam parameters are: energy E = 20 keV, working distance WD = 1 mm, and aperture A = 120 µm.

for TEM sample. Fig. 4-9 shows the kind of picture that can be obtained when we record the shadow image of this 5 nm membrane with a beam focused on the sample plane. In this case, we can clearly see the appearance of the circle of infinite magnification which encloses the central region of magnification M. This image is obtained with 20 keV energy of the electrons.

Varying the defocus of the beam with respect to the sample plane is going to change the size of the circles of infinite magnification. We can therefore use the relationship expressed in Eq. 4.3 to measure C_S using the following procedure:

1. placing of the detector at a known distance D from the sample;
2. focusing of the beam onto the sample. This procedure will be done with an unknown initial defocus R_0, since we cannot easily distinguish the Gaussian focusing condition from the image;
3. record different images at known defocus ΔR_i from the initial R_0;
4. evaluate for each image the value of R_∞; and
5. plot $\frac{R_\infty^2}{D^2}$ vs ΔR. The slope is going to be C_S and the offset $-R_0$.

Fig. 4-10 shows the result of a measurement done using this method for electrons at 20 keV and a working distance of 1 mm. A series of three images were recorded varying the defocus of 2 µm between each image and the next. The corresponding circles of infinite magnification can be evaluated knowing that the phosphorus screen is placed at 103 mm from the sample, the optical system has unitary magnification, and the CCD sensor size is 8.8 mm by 6.6 mm. The results are summarized in Table 4.2:

Table 4.2: Dependence of the size of the disc of infinite magnification with the defocus

Defocus	R_∞ (mm)
R_0	1
$R_0 + 2\,\mu\text{m}$	1.3
$R_0 + 4\,\mu\text{m}$	1.6

This data can be fitted by the equation $y[\text{mm}] = 27x - 0.0025$. Which means that the initial defocus was $R_0 = 2.5\,\mu\text{m}$ and that the corresponding spherical aberration coefficient is $C_S = 27$ mm.

4.2.2 Barrel distortion characterization

As described in the previous section, the Ronchigram method works well but it is not free of issues. In fact, we discussed the carbon deposition sample drift issues that force us to take quick measurements. Therefore, we would like to have a more robust method to evaluate aberrations. One possible way to do so is to use a sample with known topography, focusing close to the sample (but not on the sample as was done for producing Ronchigrams), and retrieve the aberration coefficient from the distortion in the shadow image.

Fig. 4-11 illustrates how this method works. When the beam is focused above the sample plane, due to spherical aberration we know that the paraxial rays are going to be focused closer to the sample while the marginal rays are going to be focused farther from it. For this reason, the former is going to produce on the detector a

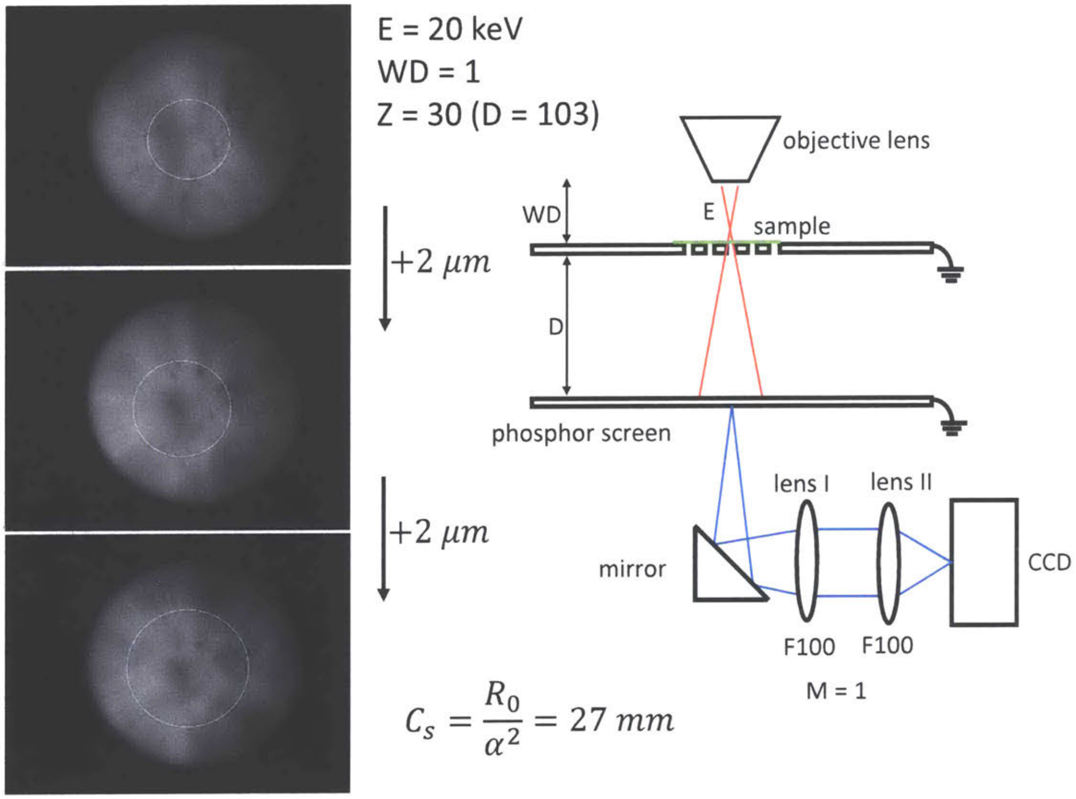

Figure 4-10: Ronchigram characterization result - The images captured with the beam focused onto the sample while varying the defocus of 2 µm, and the corresponding variation in the size of the disc of infinite magnification are portrayed, together with the experimental setup used for the characterization. For this analysis, an energy of 20 keV, a working distance of 1 mm and an aperture of 120 µm was used. The resulting spherical aberration coefficient of the beam is 27 mm.

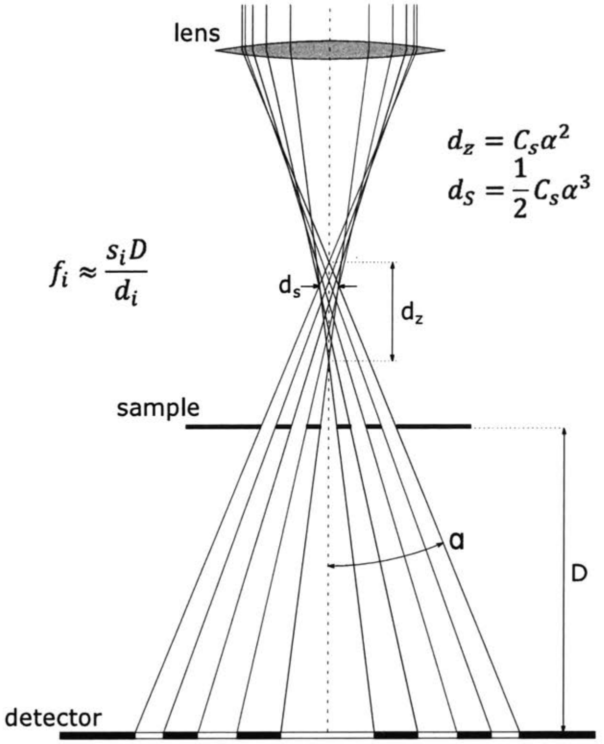

Figure 4-11: C_S evaluation through shadow imaging of a grid - Schematics of the method used to asses the spherical aberration coefficient C_S collecting shadow images of a known grid sample.

higher geometrical magnification. Therefore, if we use a sample with known feature sizes we can infer the geometrical distortion due to this effect from the shadow image characteristics. In particular, Fig. 4-12 shows the two possible image distortion that can be experienced when a beam affected by spherical aberration is focused onto a grid. If the beam is focused above the sample we are going to see barrel distortion in the image. Instead, if the beam focusing is below the sample we are going to see a pincushion distortion.

In our experiment, we decided to use a 200 nm thick Si_3N_4 membrane with a closed packed hexagonal pattern of 200 nm circular holes and a 400 nm pitch, from PELCO. The sample has also been covered by a 50 nm layer of gold using gold evaporation. This step is necessary because without the gold layer the Si_3N_4 film would be insulating. Therefore when hit by an electron beam the presence of an insulating layer would cause charging, which in turn would generate a lensing effect

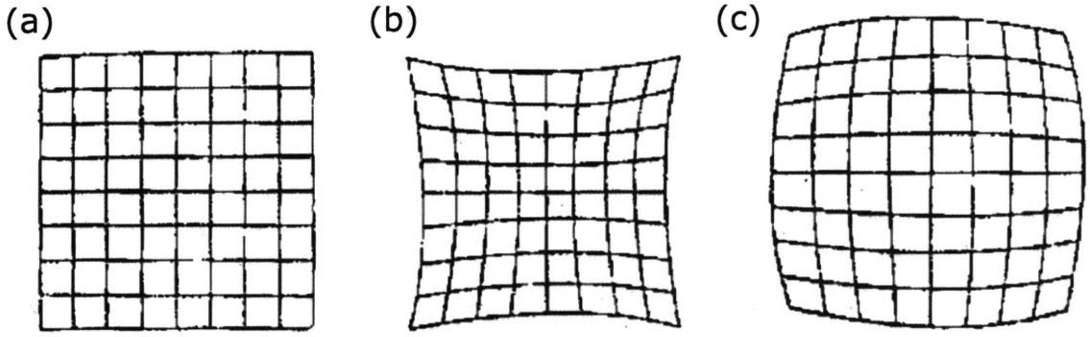

Figure 4-12: Pincushion and barrel distortion - Illustration of the pincushion (b) and barrel (c) distortion, caused by spherical aberration when the beam is focused above or below the sample respectively. The original grid is shown in (a). This image is taken from [52]

that distorts the image. Fig. 4-13 illustrates this effect. From the image, we can recognize that this effect is due to charging and not to other geometric aberration because the distortion causes the size of the holes to blow up and the size of the Si_3N_4 grid to shrink. Therefore the effect cannot be geometrical but it has to do with the sample material.

After coating the sample with the gold evaporated film this effect disappears. At this point, only the geometrical distortion remains. Fig. 4-14(a) shows an SEM image of the sample topography. Instead, in Fig. 4-14(b-d) a series of shadow images obtained varying the beam defocus are shown, from far to close. As can be clearly seen, the closer we get to the sample, the more evident the effect of the spherical aberration became. The difference between the size of the features close to the optical axis and those farther away become more prominent. In other terms, the paraxial geometrical magnification becomes much higher than the marginal one.

Once you acquire a shadow image of the aberrated beam through the sample you can retrieve the value of the spherical aberration noticing that the spherical aberration coefficient is tied both to the beam size and to the focusing spread on the axis as:

$$\begin{aligned} d_S &= \tfrac{1}{2} C_S \alpha^3, \\ d_Z &= C_S \alpha^2. \end{aligned} \tag{4.4}$$

Using this relationship you can evaluate C_S with this setup as follows:

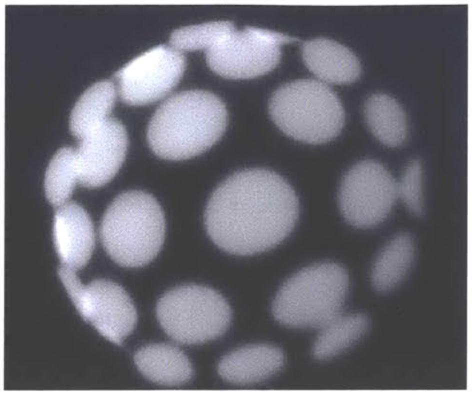

Figure 4-13: Charging effect - Shadow image of a 200 nm thick Si_3N_4 membrane patterned with 200 nm holes and a 400 nm pitch, showing the distortion due to the lensing effect caused by the charging resulting from the interaction between the electron beam and the insulating sample. The beam parameters are: energy E = 15 keV, working distance WD = 1 mm, and aperture A = 120 µm.

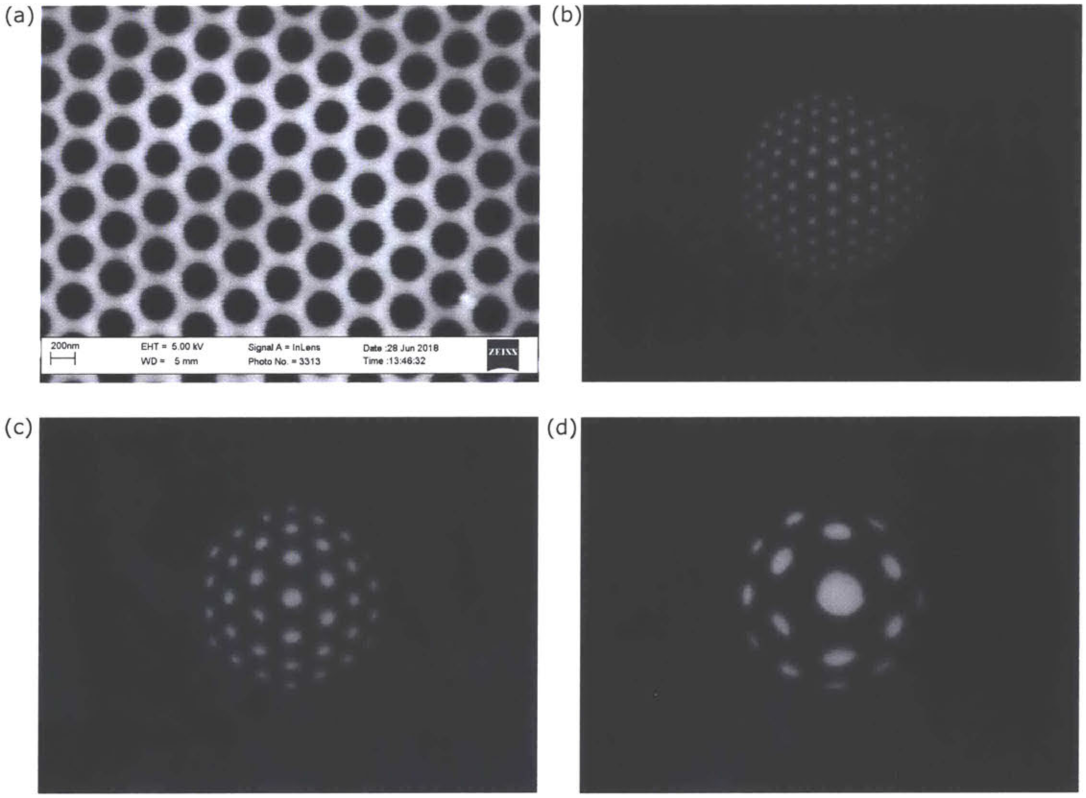

Figure 4-14: Barrel distortion at different defocus - (a) SEM picture of the 200 nm thick Si_3N_4 membrane patterned with 200 nm holes and a 400 nm pitch, coated with a 50 nm layer of evaporated gold. (b-d) Shadow images of the same sample at different values of defocus showing an increasing effect of the beam spherical aberration.

1. placing of the detector at a known distance D from the sample;
2. focusing of the beam above the sample. I decided for my measurement to focus at a distance that allows to shadow image three sets of equidistant patterned holes, including one hole in the middle;
3. do a line scan passing through the center;
4. assess the distance from the center of a series of features d_i and evaluate the corresponding focal position $f_i \sim \frac{s_i D}{d_i}$, where s_i is the known size of the feature on the sample; and
5. infer the value of C_S using the relationship $C_S = \frac{\Delta f}{\alpha^2} = \frac{(f_i - f_0)\cdot D^2}{d_i^2}$, where f_0 is the focal position of the most paraxial feature. Average the value obtained for multiple features to get a more accurate estimation.

Fig. 4-15 illustrates the image acquired for a 15 keV electron beam and a working distance of 5 mm, and the resulting data obtained from a line scan across the center. Using the method just described, from this data, we can infer the values summarized in Table 4.3:

Table 4.3: C_S analysis

d_i (mm)	s_i (μm)	f_i (μm)	C_S (mm)
0.4945	0.1	19.8	-
1.1675	0.3	25.2	37.8
1.6315	0.5	30.0	36.9
1.9525	0.7	35.1	38.6
2.2300	0.9	39.6	38.1

If we do an average among the values obtained we get a coefficient of spherical aberration $C_S = 37.8 \pm 0.9$ mm for this configuration of the beam.

The same measurement was repeated in order to characterize the beam coming from the objective lens of the SEM for multiple working distances. This study, which is shown in Fig. 4-16(a), resulted in a f^3 dependence of the spherical aberration

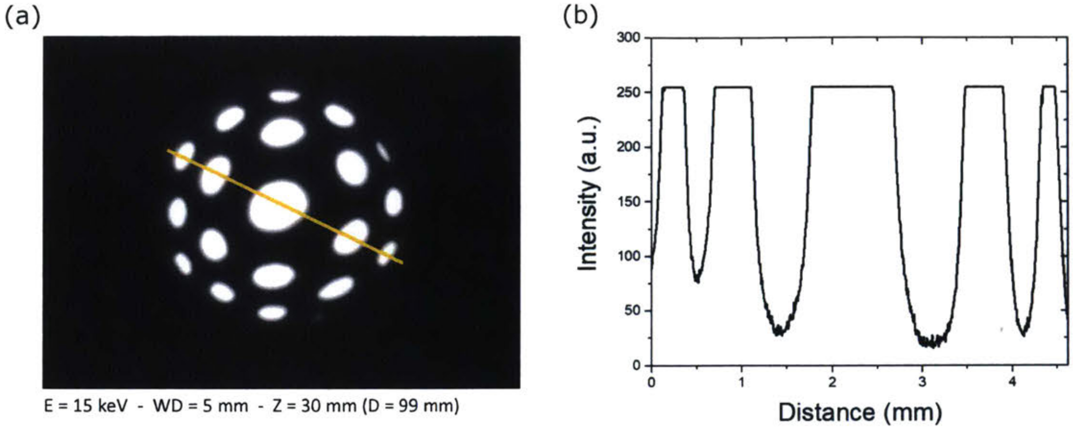

Figure 4-15: Data used for a C_S evaluation through shadow imaging - Data acquired from the shadow image of a conductive grid (a) and signal amplitude from a line scan across the center of the beam(b). This measurement resulted in the determination of a spherical aberration coefficient of $C_S = 37.8$ mm. This measurement was performed for a 15 keV beam and a working distance of 5 mm.

coefficient C_S which is consistent with the expected C_S behavior for a weak magnetic lens.[35] For a strong lens, hence very short working distances there is instead an f behavior. A similar set of data points was also measured for different energies, in order to get a more comprehensive characterization of the SEM illumination beam. The resulting values are summarized in Fig. 4-16(b). As we can see from this figure higher energies correspond to higher spherical aberration coefficient, which is consistent with what found in [43].

It is worth noticing that the C_S coefficient obtained from this method is comparable with that evaluated with the Ronchigram method. However, this method is more systematic and stable with time, because carbon deposition is not an issue and a small drift of the sample does not affect the measurement. Moreover, it can be applied for any energy. Instead, the Ronchigram, since it relies on transmission through a sample, cannot be applied for low energies, at least not in the thin film version. In fact, at low energy the interaction probability with the sample is going to be higher, therefore the transmitted beam is going to be low to null, which prevents the image formation on the phosphorus screen.

In conclusion, for these reasons, to do a complete assessment of the beam spherical

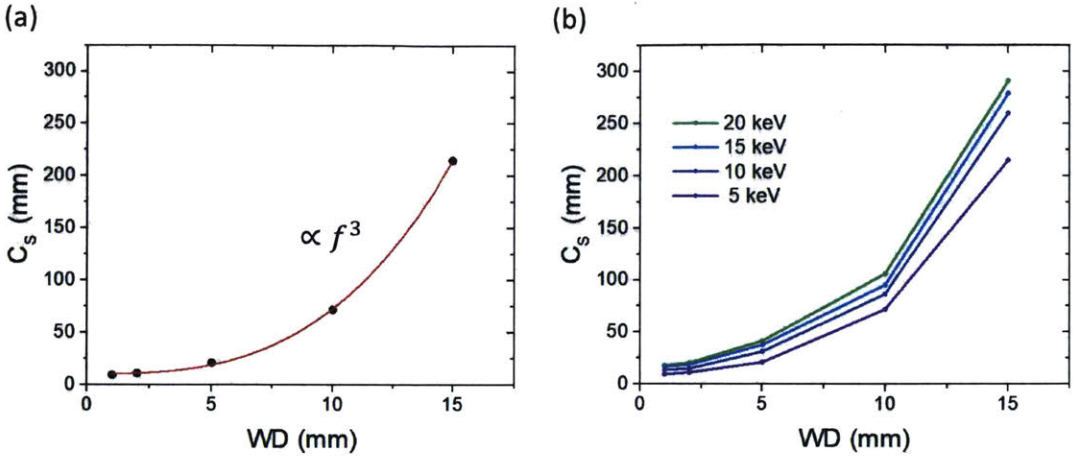

Figure 4-16: Experimental evaluation of the C_S dependence with working distance and beam energy - (a) show the measurement of C_S for different working distances at 5 keV, and f^3 fit; (b) shows the same measurement performed for different beam energies.Namely, 5 keV, 10 keV, 15 keV and 20 keV.

aberration, it is preferable to use a sample with known patterned features, possibly grid-like, and characterize the barrel distortion due to the aberration acquiring a shadow image of the sample.

Chapter 5

Conclusion

In conclusion, in this work, the main components necessary to design a linear resonant cavity for multi-pass microscopy were simulated and characterized in terms of their optical properties. In particular, a preliminary gated mirror device was simulated and experimentally tested to asses its frequency response and its DC optical properties. The possibility of compensating for spherical aberration adopting a hyperbolic mirror approach was also analyzed.

A resonant cavity based on aberration-corrected gated mirrors and magnetic lenses was also proposed and verified through simulation. The realization of such a resonant cavity would allow the proof-of-concept demonstration of a system able to significantly reduce the radiation damage adopting a multi-pass measurement scheme into an SEM.

Finally, a characterization and diagnostic setup for electron optical component were developed, assembled and experimentally tested in order to extract and study an electron beam optical and electrical properties. This apparatus allows for the assessment of the beam current, its energy spread and astigmatism and spherical aberrations. Different techniques for characterizing spherical aberrations in an SEM were tested and compared.

This work is part of the ongoing effort for achieving direct imaging of macromolecules with sub-nm resolution. Future work will include the experimental demonstration of the elements composing the cavity and of their integration to build the complete system, as well as additional effort in improving the performance of the cavity in terms of imaging resolution. Moreover, further work to include the analysis of the other beam aberrations using ptychography techniques in the same diagnostic apparatus is going to be valuable to better characterize the electron optical components composing the system and developing a working prototype of a multi-pass microscope. Such a device could be an invaluable ally for biologists in the study of proteins and macromolecules that could have a precious impact in the advancement of modern medicine and society in general.

Bibliography

[1] L. Jin, J. Barthel, J. Chun-Lin, Atomic resolution imaging of YAlO3: Ce in the chromatic and sphericalaberration corrected PICO electron microscope, Ultramicroscopy 176, 99-104 (2017) https://doi.org/10.1017/S1431927617002793

[2] D. T. Grubb and A. Keller, Proceedings of the Fifth European Regional Conferences on Electron Microscopy, Manchester, 554–560 (1972).

[3] D. T. Grubb, Radiation damage and electron microscopy of organic polymers, Journal of Material Science 9, 1715-1736 (1974) https://doi.org/10.1007/BF00540772

[4] R. Henderson, The potential and limitations of neutrons, electrons and X-rays for atomic resolution microscopy of unstained biological molecules, Q. Rev. Biophys. 28, 171 (1995). https://doi.org/10.1017/S003358350000305X

[5] D.B. Williams,C.B.Carter,Transmission Electron Microscopy: A Textbook for Materials Science, Springer, 64-65, (2009). https://doi.org/10.1007/978-0-387-76501-3

[6] D. B. Carlson, J. E. Evans, Low-Dose Imaging Techniques for Transmission Electron Microscopy, The Transmission Electron Microscope, InTech 85-96 (2012). https://doi.org/10.5772/36614

[7] J. Vonck, D. J. Mills, Advances in high-resolution cryo-EM of oligomeric enzymes, Current Opinion in Structural Biology 46, 48-54 (2017). https://doi.org/10.1016/j.sbi.2017.05.016

[8] W. Chiu, K. H. Downing, Editorial overview: Cryo Electron Microscopy: Exciting advances in CryoEM Herald a new era in structural biology, Current Opinion in Structural Biology 46, iv-viii (2017). https://doi.org/10.1016/j.sbi.2017.07.006

[9] C. A. Diebolder, A. J. Koster, R. I. Koning, Pushing the resolution limits in cryo electron tomographyof biological structures, Journal of Microscopy 248, 1–5 (2012). https://doi.org/10.1111/j.1365-2818.2012.03627.x

[10] W. Kühlbrandt, Microscopy: Cryo-EM enters a new era, eLife 3:e03665 (2014). https://doi.org/10.7554/eLife.03678

[11] R. M. Glaeser, How good can cryo-EM become?, Nature Methods 13, 28-32 (2016). https://doi.org/10.1038/nmeth.3695

[12] H. Okamoto, T. Latychevskaia, H.-W. Fink, A quantum mechanical scheme to reduce radiation damage in electron microscopy, Appl. Phys. Lett. 88 (2006). https://doi.org/10.1063/1.2191096

[13] H. Okamoto, Y. Nagatani, Entanglement-assisted electron microscopy based on a flux qubit, Appl. Phys. Lett. 104 (2014). https://doi.org/10.1063/1.4865244

[14] H.W. Fink, W. Stocker, H. Schmid, Holography with low-energy electrons, Phys. Rev. Lett. 65 (1990) 1204–1206. https://doi:10.1103/PhysRevLett.65.1204.

[15] M.J. Humphry, B. Kraus, A.C. Hurst, A.M. Maiden, J.M. Rodenburg, Ptychographic electron microscopy using high-angle dark-field scattering for sub-nanometre resolution imaging, Nat. Commun. 3 (2012). https://doi:10.1038/ncomms1733.

[16] P. Kruit, R.G. Hobbs, C-S. Kim, Y. Yang, V.R. Manfrinato, J. Hammer, S. Thomas, P. Weber, B. Klopfer, C. Kohstall, T. Juffmann, M.A. Kasevich, P. Hommelhoff, K.K. Berggren, Designs for a quantum electron microscope, Ultramicroscopy 164, 31–45 (2016). https://doi.org/10.1016/j.ultramic.2016.03.004

[17] T. Juffmann, B. B. Klopfer, T. L.I. Frankort, P. Haslinger and M. A. Kasevich, Multi-pass microscopy, Nature Communications 7, 12858 (2016). https://doi.org/10.1038/ncomms12858

[18] T. Juffmann, S. A. Koppel, B. B. Klopferl, C. Ophus, R. M. Glaeser and M. A. Kasevich, Multi-pass transmission electron microscopy, Scientific Reports 7, 1699 (2017). https://doi.org/10.1038/s41598-017-01841-x

[19] V. Giovannetti, S. Lloyd and L. Maccone, Quantum metrology, Physical Review Letters 96, 010401 (2006). https://doi.org/10.1103/PhysRevLett.96.010401

[20] V. Giovannetti, S. Lloyd and L. Maccone, Advances in quantum metrology, Nature Photonics 5, 222–229 (2011). https://doi.org/10.1038/nphoton.2011.35

[21] M. Turchetti, Master's Thesis: Quantum electron microscope for interaction-free measurements, Politecnico di Torino, Grenoble INP, EPFL (2016)

[22] J. M. Cowley, Adjustment of a STEM instrument by use of shadow imaging, Ultramicroscopy 4, 413-418 (1979). https://doi.org/10.1016/S0304-3991(79)80018-2

[23] J. M. Cowley, Coherent interference in convergent-beam electron diffraction and shadow imaging, Ultramicroscopy 4, 435-450 (1979). https://doi.org/10.1016/S0304-3991(79)80021-2

[24] J. A. Lin, J. M. Cowley, Calibration of the operating parameters for an HB5 STEM instrument, Ultramicroscopy 19, 31-42 (1986). https://doi.org/10.1016/0304-3991(86)90005-7

[25] P. W. Hawkes, E. Kasper, Principles of Electron Optics: Basic Geometrical Optics, Academic Press (1996). https://doi.org/10.1016/B978-0-12-333352-0.50003-7

[26] R. Brydson, Aberration-Corrected Analytical Transmission Electron Microscopy, John Wiley and Sons Ltd., (2011). https://doi.org/10.1002/9781119978848

[27] O. Scherzer, Uber einige Fehler von Elektronenlinsen, Zeitschrift Für Phys. 101 (1936) 593-603. https://doi.org/10.1007/BF01349606

[28] H. M. L. Faulkner, L. J. Allen, M. P. Oxley, D. Paganin, Computational aberration determination and correction, Optics Communications 216 (2016) 89-98. https://doi.org/10.1016/S0030-4018(02)02298-8

[29] J. C. Wyant, K. Creath, Basic wavefront aberration theory for optical metrology, Applied optics and optical engineering XI, chap. 1 (1992).

[30] G.R. Rempfer, A theoretical study of the hyperbolic electron mirror as a correcting element for spherical and chromatic aberration in electron optics, J. Appl. Phys. 67 (1990). https://doi.org/10.1063/1.345212

[31] G.R. Rempfer, D. M. Desloge, W. P. Skoczylas, O. H. Griffith, Simultaneous correction of spherical and chromatic aberrations with an electron mirror: an electron optical Achromat, Microscopy and Microanalysis 3 (1997). https://doi.org/10.1017/S143192769797001X

[32] J.P.S. Fitzgerald, R.C. Word, R. Konenkamp, Adaptive aberration correction using a triode hyperbolic electron mirror, Ultramicroscopy. 111 (2011) 1495-1503. https://doi.org/10.1016/j.ultramic.2011.06.004

[33] J.P.S. Fitzgerald, R.C. Word, R. Konenkamp, Simultaneous and independent adaptive correction of spherical and chromatic aberration using an electron mirror and lens combination, Ultramicroscopy. 115 (2012) 35-40. https://doi.org/10.1016/j.ultramic.2012.02.001

[34] H. Koike, S. Okada, Charged particle beam reflector device and electron microscope, US Patent: US7902504B2 (2007).

[35] P. Kruit, Introduction to Charged Particle Optics - Notes (2014).

[36] N. Abedzadeh, Master's Thesis: Diffractive electron mirror for use in quantum electron microscopy, MIT (2018). http://hdl.handle.net/1721.1/115627

[37] P.E. Batson, N. Dellby, O.L. Krivanek, Sub-Angstrom resolution using aberration corrected electron optics., Nature. 418 (2002) 617-620. https://doi.org/10.1038/nature00972

[38] O.L. Krivanek, N. Dellby, A.R. Lupini, Towards sub-A electron beams, Ultramicroscopy. 78 (1999) 1-11. https://doi.org/10.1016/S0304-3991(99)00013-3

[39] P. Hartel, D. Preikszas, R. Spehr, H. Müller, H. Rose, Mirror corrector for low-voltage electron microscopes, Adv. Imaging Electron Phys. 120 (2003) 41-133. https://doi.org/10.1016/S1076-5670(02)80034-9

[40] G. Schonhense, H. Spiecker, Correction of chromatic and spherical aberration in electron microscopy utilizing the time structure of pulsed excitation sources, J. Vac. Sci. Technol. B. 20 (2002) 2526-2534. https://doi.org/10.1116/1.1523373

[41] R.H. Van Aken, C.W. Hagen, J.E. Barth, P. Kruit, Low-energy foil aberration corrector, Ultramicroscopy. 93 (2002) 321-330. https://doi.org/10.1016/S0304-3991(02)00287-5

[42] US Patent 7902504B2, Charged particle beam reflector device and electron microscope, Topcon KK (2007)

[43] P. Gnauck, P. Hoffrogge, J. Greiser, A New CrossBeam Inspection Tool Combining an Ultrahigh Resolution Field emission SEM and a High Resolution FIB, Proceeding of SPIE - The International Society of Optical Engineering 4689 (2002) . https://doi.org/10.1117/12.473530

[44] D. Ehberger, J. Hammer, M. Eisele, M. Krüger, J. Noe, A. Högele, P. Hommelhoff, Highly Coherent Electron Beam from a Laser-Triggered Tungsten Needle Tip, Physical Review Letters 114, 227601 (2015). https://doi.org/10.1103/PhysRevLett.114.227601

[45] S. Meuret, M. Solà Garcia, T. Coenena, E. Kieft, H. Zeijlemaker, M. Lätzel, S. Christiansen, S.Y. Woo, Y.H. Ra, Z. Mi, A. Polman, Complementary cathodoluminescence lifetime imaging configurations in a scanning electron microscope, Ultramicroscopy 197, 28-38 (2019). https://doi.org/10.1016/j.ultramic.2018.11.006

[46] F. Houdellier, G.M. Caruso, S. Weber, M. Kociak, A. Arbouet, Development of a high brightness ultrafast Transmission Electron Microscope based on a

laser-driven cold field emission source, Ultramicroscopy 186, 128-138 (2018). https://doi.org/10.1016/j.ultramic.2017.12.015

[47] R. Bormann, S. Strauch, S. Schäfer, and C. Ropers, An ultrafast electron microscope gun driven by two-photon photoemission from a nanotip cathode, Journal of Applied Physics 118, 17305 (2015). https://doi.org/10.1063/1.4934681

[48] A. Feist, N. Bach, N. R. da Silva, T. Danz, M. Möller, K. E. Priebe, T. Domröse, J. G. Gatzmann, S. Rost, J. Schauss, S. Strauch, R. Bormann, M. Sivis, S. Schäfer, C. Ropers, Ultrafast transmission electron microscopy using a laser-driven field emitter: Femtosecond resolution with a high coherence electron beam, Ultramicroscopy 176, 63-73 (2017). https://doi.org/10.1016/j.ultramic.2016.12.005

[49] R. Moerland, I. G. C. Weppelman, M. W. H. Garming, P. Kruit, J. P. Hoogenboom, Time-resolved cathodoluminescence microscopy with sub-nanosecond beam blanking for direct evaluation of the local density of states, Optics Express 24, 21 (2016). https://doi.org/10.1364/OE.24.024760

[50] I. G. C. Weppelman, R. J. Moerland, J. P. Hoogenboom, P. Kruit, Concept and design of a beam blanker with integrated photoconductive switch for ultrafast electron microscopy, Ultramicroscopy 184 B, 8-17 (2018). https://doi.org/10.1016/j.ultramic.2017.10.002

[51] H. Dohi, P. Kruit, Design for an aberration corrected scanning electron microscope using miniature electron mirrors, Ultramicroscopy 189, 1-23 (2018). https://doi.org/10.1016/j.ultramic.2018.03.009

[52] K. C. Fan, M.-Z Lee, J.-I. Mou, On-Line Non-Contact System for Grinding Wheel Wear Measurement. International Journal of Advanced Manufacturing Technology. 19 (2002) 14-22. https://doi.org/10.1007/PL00003964.